

A Comparative Laboratory Study of Metallic Reinforcing Steels for Corrosion Protection of Reinforced Concrete Bridge Structures

PUBLICATION NO. FHWA-HRT-15-078

JUNE 2018



U.S. Department of Transportation
Federal Highway Administration

Research, Development, and Technology
Turner-Fairbank Highway Research Center
6300 Georgetown Pike
McLean, VA 22101-2296

FOREWORD

This final report presents research findings of a comparative laboratory study evaluating the corrosion resistance of 12 alternative metallic reinforcing materials embedded for about 18 mo in 8 large-scale concrete slabs that simulated typical reinforced concrete bridge decks. Based on electrochemical test data and autopsy results, the materials were divided into three groups: four products in the best performance group, six products in the intermediate performance group, and two products in the poorest performance group.

This study was conducted as part of the Federal Highway Administration's Long-Term Bridge Performance Program. The products from this program will be a collection of data-driven tools, including predictive and forecasting models, that will enhance the abilities of bridge owners to optimize their management of bridges. This report should be of interest to bridge program personnel from Federal, State, and local transportation departments. Also, bridge design engineers, specification writers, manufacturers/suppliers of reinforcing steel, and reinforcing detailers would benefit from reading this report.

Cheryl Allen Richter, P.E., Ph.D.
Director, Office of Infrastructure
Research and Development

Notice

This document is disseminated under the sponsorship of the U.S. Department of Transportation (USDOT) in the interest of information exchange. The U.S. Government assumes no liability for the use of the information contained in this document.

The U.S. Government does not endorse products or manufacturers. Trademarks or manufacturers' names appear in this report only because they are considered essential to the objective of the document.

Quality Assurance Statement

The Federal Highway Administration (FHWA) provides high-quality information to serve Government, industry, and the public in a manner that promotes public understanding. Standards and policies are used to ensure and maximize the quality, objectivity, utility, and integrity of its information. FHWA periodically reviews quality issues and adjusts its programs and processes to ensure continuous quality improvement.

TECHNICAL REPORT DOCUMENTATION PAGE

1. Report No. FHWA-HRT-15-078	2. Government Accession No.	3. Recipient's Catalog No.	
4. Title and Subtitle A Comparative Laboratory Study of Metallic Reinforcing Steels for Corrosion Protection of Reinforced Concrete Bridge Structures		5. Report Date June 2018	
		6. Performing Organization Code	
7. Author(s) Seung-Kyoung Lee		8. Performing Organization Report No.	
9. Performing Organization Name and Address SK Lee & Associates, Inc. 10813 Fieldwood Drive Fairfax, VA 22030 Rutgers, The State University Center for Advanced Infrastructure and Transportation 100 Brett Road Piscataway, NJ 08854		10. Work Unit No.	
		11. Contract or Grant No. DTFH61-08-C-00005	
12. Sponsoring Agency Name and Address Office of Infrastructure Research and Development Federal Highway Administration 6300 Georgetown Pike McLean, VA 22101-2296		13. Type of Report and Period Covered Final Report; January 2009–August 2015	
		14. Sponsoring Agency Code HRDI-10	
15. Supplementary Notes The Technical Contact was Donald Becker (HRDI-10), and the Contracting Officer's Representative was Robert Zobel (HRDI-30).			
16. Abstract This report presents study findings related to corrosion resistance of 12 types of metallic reinforcing steel bars. The accelerated laboratory corrosion testing was performed using eight large-scale concrete slabs that simulated typical reinforced concrete bridge decks for about 18 mo by an accelerated corrosion testing protocol followed by a detailed autopsy of extracted bar samples and acid-soluble chloride concentrations determined at the bar imprints. The weekly corrosion testing protocol consisted of a 3-d wetting cycle in 15 weight percent chloride solution at 77 °F and a 4-d drying cycle at 100 °F. The best corrosion performance group of reinforcing bars includes epoxy-coated reinforcing steel, dual-coated reinforcing steel, stainless steel–clad reinforcing steel, and duplex solid stainless reinforcing steel with 23 percent chromium. The intermediate corrosion performance group includes duplex solid stainless reinforcing steel with 21 percent chromium, austenitic solid stainless reinforcing steel, another type of stainless steel–clad reinforcing steel, ferritic solid stainless reinforcing steel with 12 percent chromium, high-strength micro-composite reinforcing steel, and hot-dip galvanized reinforcing steel. The poorest corrosion performance group includes black steel and lean duplex solid stainless reinforcing steel with 12 percent chromium.			
17. Key Words Corrosion, Corrosion-resistant reinforcing steel, Chloride threshold, Corrosion initiation, Corrosion propagation, Autopsy, Accelerated corrosion testing		18. Distribution Statement No restrictions. This document is available to the public through the National Technical Information Service, Springfield, VA 22161. http://www.ntis.gov	
19. Security Classif. (of this report) Unclassified	20. Security Classif. (of this page) Unclassified	21. No of Pages 170	22. Price

SI* (MODERN METRIC) CONVERSION FACTORS

APPROXIMATE CONVERSIONS TO SI UNITS

Symbol	When You Know	Multiply By	To Find	Symbol
LENGTH				
in	inches	25.4	millimeters	mm
ft	feet	0.305	meters	m
yd	yards	0.914	meters	m
mi	miles	1.61	kilometers	km
AREA				
in ²	square inches	645.2	square millimeters	mm ²
ft ²	square feet	0.093	square meters	m ²
yd ²	square yard	0.836	square meters	m ²
ac	acres	0.405	hectares	ha
mi ²	square miles	2.59	square kilometers	km ²
VOLUME				
fl oz	fluid ounces	29.57	milliliters	mL
gal	gallons	3.785	liters	L
ft ³	cubic feet	0.028	cubic meters	m ³
yd ³	cubic yards	0.765	cubic meters	m ³
NOTE: volumes greater than 1000 L shall be shown in m ³				
MASS				
oz	ounces	28.35	grams	g
lb	pounds	0.454	kilograms	kg
T	short tons (2000 lb)	0.907	megagrams (or "metric ton")	Mg (or "t")
TEMPERATURE (exact degrees)				
°F	Fahrenheit	5 (F-32)/9 or (F-32)/1.8	Celsius	°C
ILLUMINATION				
fc	foot-candles	10.76	lux	lx
fl	foot-Lamberts	3.426	candela/m ²	cd/m ²
FORCE and PRESSURE or STRESS				
lbf	poundforce	4.45	newtons	N
lbf/in ²	poundforce per square inch	6.89	kilopascals	kPa

APPROXIMATE CONVERSIONS FROM SI UNITS

Symbol	When You Know	Multiply By	To Find	Symbol
LENGTH				
mm	millimeters	0.039	inches	in
m	meters	3.28	feet	ft
m	meters	1.09	yards	yd
km	kilometers	0.621	miles	mi
AREA				
mm ²	square millimeters	0.0016	square inches	in ²
m ²	square meters	10.764	square feet	ft ²
m ²	square meters	1.195	square yards	yd ²
ha	hectares	2.47	acres	ac
km ²	square kilometers	0.386	square miles	mi ²
VOLUME				
mL	milliliters	0.034	fluid ounces	fl oz
L	liters	0.264	gallons	gal
m ³	cubic meters	35.314	cubic feet	ft ³
m ³	cubic meters	1.307	cubic yards	yd ³
MASS				
g	grams	0.035	ounces	oz
kg	kilograms	2.202	pounds	lb
Mg (or "t")	megagrams (or "metric ton")	1.103	short tons (2000 lb)	T
TEMPERATURE (exact degrees)				
°C	Celsius	1.8C+32	Fahrenheit	°F
ILLUMINATION				
lx	lux	0.0929	foot-candles	fc
cd/m ²	candela/m ²	0.2919	foot-Lamberts	fl
FORCE and PRESSURE or STRESS				
N	newtons	0.225	poundforce	lbf
kPa	kilopascals	0.145	poundforce per square inch	lbf/in ²

*SI is the symbol for the International System of Units. Appropriate rounding should be made to comply with Section 4 of ASTM E380.
(Revised March 2003)

TABLE OF CONTENTS

CHAPTER 1. INTRODUCTION.....	1
CHAPTER 2. MATERIALS AND EXPERIMENTAL PROCEDURES.....	3
BAR MATERIALS.....	3
Black Reinforcing Steel	5
ECR	5
DCR.....	5
HDG	6
SCR1.....	6
SCR2.....	6
SSR1	6
SSR2	7
SSR3	7
HSR	7
LSS1	7
LSS2	7
INTRODUCTION OF ARTIFICIAL DEFECTS.....	8
FABRICATION OF CONCRETE TEST SLABS.....	10
ACCELERATED CORROSION TESTING	23
Corrosion Tests	26
Data Collection Procedure	30
Acid-Soluble (Total) Chloride Analysis	30
Unscheduled Interruptions	31
AUTOPSY OF TEST SLABS.....	32
Core Extraction.....	32
Photographic Documentation of Cores.....	34
Condition Evaluation of Extracted Bar Samples.....	35
Final Chloride Analysis	36
CHAPTER 3. TEST RESULTS AND DISCUSSION	39
PHYSICAL CONDITION OF TEST SLABS.....	39
POTENTIAL AND I_{MACRO}-CELL DATA.....	40
Black Reinforcing Steel (Slabs 1 and 8)	40
SCR1 (Slab 2L).....	45
ECR Top Mat/Black Steel Bottom Mat (Slab 2R)	46
ECR in Both Mats (Slab 3L).....	48
SCR2 (Slab 3R)	49
LSS2 (Slab 4L).....	50
HDG (Slab 4R)	52
HSR (Slab 5L)	53
SSR1 (Slab 5R)	55

LSS1 (Slab 6L).....	56
DCR (Slab 6R).....	58
SSR2 (Slab 7L)	59
SSR3 (Slab 7R).....	60
AC RESISTANCE	62
INSTANTANEOUS RATE OF CORROSION.....	64
CHLORIDE ANALYSIS	67
CONDITION EVALUATION OF EXTRACTED BAR SAMPLES.....	93
Black Reinforcing Steel (Slabs 1 and 8).....	93
SCR1 (Slab 2L).....	97
ECR Top Mat/Black Bar Bottom Mat (Slab 2R).....	99
ECR in Both Mats (Slab 3L).....	104
SCR2 (Slab 3R)	106
LSS2 (Slab 4L).....	109
HDG (Slab 4R)	111
HSR (Slab 5L)	115
SSR1 (Slab 5R).....	118
LSS1 (Slab 6L).....	120
DCR (Slab 6R).....	122
SSR2 (Slab 7L)	125
SSR3 (Slab 7R).....	126
DISCUSSION	129
CHAPTER 4. A FOLLOW-UP LABORATORY STUDY	135
PREPARATION OF EXPERIMENT.....	135
Reinforcing Bars	135
Cylindrical Specimens	135
Slab Specimens.....	142
Concrete Casting and Curing.....	143
Exposure Testing and Data Collection.....	146
TEST RESULTS AND DISCUSSION.....	148
OCP Data.....	148
Rp Data	151
I _{macro-cell} Data.....	152
CHAPTER 5. CONCLUSIONS.....	153
REFERENCES.....	155

LIST OF FIGURES

Figure 1. Photo. Bar samples acquired from 11 sources.....	5
Figure 2. Photo. Example of as-received ECR defects.....	8
Figure 3. Photo. Creation of artificial coating damage.....	9
Figure 4. Photo. Close-up view of an artificial coating damage on an ECR.....	9
Figure 5. Photo. ECR samples with various types of coating damage.....	10
Figure 6. Photo. Close-up view of an artificial coating damage on an HDG.....	10
Figure 7. Illustrations. Bar arrangement in concrete slabs.....	13
Figure 8. Photos. Complete set of SCR2 prior to placement in a mold.....	14
Figure 9. Photo. Fabrication of two bottom mats.....	14
Figure 10. Photo. Close-up view of two crossing bars in the bottom mat.....	15
Figure 11. Photo. Completed four bottom mats in two molds.....	15
Figure 12. Photo. Close-up view of transverse and longitudinal bars in the top mat.....	16
Figure 13. Photo. Encapsulating cut ends of top mat longitudinal bars.....	17
Figure 14. Photo. Fabrication of a top mat.....	17
Figure 15. Photo. Electrical wires attached to longitudinal bars.....	18
Figure 16. Illustration. Identification of top mat bars.....	18
Figure 17. Photo. Top mat with 2-inch clear cover.....	19
Figure 18. Photo. Top mat with 1-inch clear cover.....	19
Figure 19. Photo. Completed slab sections.....	20
Figure 20. Photo. Second view of completed slab sections.....	20
Figure 21. Photo. Concrete molds ready for casting.....	21
Figure 22. Photo. Concrete casting.....	21
Figure 23. Photo. Demolded concrete slabs.....	22
Figure 24. Photo. Curing of concrete slabs.....	22
Figure 25. Photo. Placement of cured concrete slabs in the laboratory.....	23
Figure 26. Photo. Ponding wells and marking of data measurement spots.....	23
Figure 27. Photo. Closed heat tents during a drying cycle.....	24
Figure 28. Photo. Opened heat tents during a wetting cycle.....	25
Figure 29. Photo. Data collection switch box.....	25
Figure 30. Illustration. OCP measurement.....	26
Figure 31. Illustration. $I_{\text{macro-cell}}$ measurement.....	27
Figure 32. Illustration. AC resistance measurement.....	28
Figure 33. Illustration. LPR measurement.....	28
Figure 34. Photo. Corrosion rate measurement in progress.....	29
Figure 35. Photo. Chloride sampling at the top mat bar depth.....	31
Figure 36. Photo. Concrete slabs with leaking ponding wells.....	32
Figure 37. Photo. Concrete slab section ready for coring.....	33
Figure 38. Photo. Coring work in progress.....	33
Figure 39. Photo. Storage of extracted cores in the laboratory.....	34
Figure 40. Photo. Documentation of a core.....	34
Figure 41. Photo. Documentation of a core's bottom showing a severely corroded black bar.....	35
Figure 42. Photo. Splitting a core at the transverse bar depth.....	35
Figure 43. Photo. Documentation of a bar/concrete interface after splitting.....	36

Figure 44. Photo. Concrete powder sampling from upper bar imprint of a core.	37
Figure 45. Photo. Concrete powder sampling by drilling.	37
Figure 46. Photo. Close-up view of a sampling hole.	38
Figure 47. Photos. Corrosion damage on slab 1R.	39
Figure 48. Photo. Rust oozing out of a top mat transverse bar.	40
Figure 49. Graph. Potential versus time plot for 1-inch black bars in slab 1R.	41
Figure 50. Graph. $i_{\text{macro-cell}}$ versus time plot for 1-inch black bars in slab 1R.	42
Figure 51. Graph. Potential versus time plot for 1-inch black bars in slab 8R.	42
Figure 52. Graph. $i_{\text{macro-cell}}$ versus time plot for 1-inch black bars in slab 8R.	43
Figure 53. Graph. Potential versus time plot for 2-inch black bars in slab 1L.	43
Figure 54. Graph. $i_{\text{macro-cell}}$ versus time plot for 2-inch black bars in slab 1L.	44
Figure 55. Graph. Potential versus time plot for 2-inch black bars in slab 8L.	44
Figure 56. Graph. $i_{\text{macro-cell}}$ versus time plot for 2-inch black bars in slab 8L.	45
Figure 57. Graph. Potential versus time plot for SCR1 in slab 2L.	46
Figure 58. Graph. $i_{\text{macro-cell}}$ versus time plot for SCR1 in slab 2L.	46
Figure 59. Graph. Potential versus time plot for ECR + black in slab 2R.	47
Figure 60. Graph. $i_{\text{macro-cell}}$ versus time plot for ECR + black in slab 2R.	47
Figure 61. Graph. Potential versus time plot for ECR in slab 3L.	48
Figure 62. Graph. $i_{\text{macro-cell}}$ versus time plot for ECR in slab 3L.	49
Figure 63. Graph. Potential versus time plot for SCR2 in slab 3R.	50
Figure 64. Graph. $i_{\text{macro-cell}}$ versus time plot for SCR2 in slab 3R.	50
Figure 65. Graph. Potential versus time plot for LSS2 in slab 4L.	51
Figure 66. Graph. $i_{\text{macro-cell}}$ versus time plot for LSS2 in slab 4L.	52
Figure 67. Graph. Potential versus time plot for HDG in slab 4R.	53
Figure 68. Graph. $i_{\text{macro-cell}}$ versus time plot for HDG in slab 4R.	53
Figure 69. Graph. Potential versus time plot for HSR in slab 5L.	54
Figure 70. Graph. $i_{\text{macro-cell}}$ versus time plot for HSR in slab 5L.	55
Figure 71. Graph. Potential versus time plot for SSR1 in slab 5R.	56
Figure 72. Graph. $i_{\text{macro-cell}}$ versus time plot for SSR1 in slab 5R.	56
Figure 73. Graph. Potential versus time plot for LSS1 in slab 6L.	57
Figure 74. Graph. $i_{\text{macro-cell}}$ versus time plot for LSS1 in slab 6L.	57
Figure 75. Graph. Potential versus time plot for DCR in slab 6R.	58
Figure 76. Graph. $i_{\text{macro-cell}}$ versus time plot for DCR in slab 6R.	59
Figure 77. Graph. Potential versus time plot for SSR2 in slab 7L.	60
Figure 78. Graph. $i_{\text{macro-cell}}$ versus time plot for SSR2 in slab 7L.	60
Figure 79. Graph. Potential versus time plot for SSR3 in slab 7R.	61
Figure 80. Graph. $i_{\text{macro-cell}}$ versus time plot for SSR3 in slab 7R.	62
Figure 81. Graph. AC resistance versus time plot for bare bars.	63
Figure 82. Graph. AC resistance versus time plot for coated bars.	63
Figure 83. Graph. Example of low R_p data.	64
Figure 84. Graph. Example of intermediate R_p data.	64
Figure 85. Graph. Example of high R_p data.	65
Figure 86. Graph. Mean normalized R_p measured at different times.	66
Figure 87. Graph. Overall mean normalized R_p	66
Figure 88. Photo. Corrosion-damaged slab 1R with a 5-2 core ID (black bar at 1-inch cover).	94

Figure 89. Photo. Corrosion-damaged slab 1R with a 3-2 core ID (black bar at 1-inch cover).....	94
Figure 90. Photo. Extracted black bar from slab 1L with a 2-1 core ID ($[Cl^-]_{interface@2-inch} = 1,298$ ppm).....	94
Figure 91. Photo. Close-up view of the bar shown in figure 90.....	95
Figure 92. Photo. Extracted black bar from slab 1L with a 6-3 core ID ($[Cl^-]_{interface@2-inch} = 3,416$ ppm).....	95
Figure 93. Photo. Close-up view of the bar shown in figure 92.....	95
Figure 94. Photo. Extracted black bar from slab 8L with a 1-2 core ID ($[Cl^-]_{interface@2-inch} = 525$ ppm).....	96
Figure 95. Photo. Close-up view of the bar shown in figure 94.....	96
Figure 96. Photo. Extracted black bar from slab 8L with a 5-3 core ID ($[Cl^-]_{interface@2-inch} = 2,499$ ppm).....	96
Figure 97. Photo. Close-up view of the bar shown in figure 96.....	97
Figure 98. Photo. Extracted SCR1 from slab 2L with a 5-1 core ID ($[Cl^-]_{interface@2-inch} = 1,114$ ppm).....	97
Figure 99. Photo. Close-up view of the bar shown in figure 98.....	97
Figure 100. Photo. Extracted SCR1 from slab 2L with a 2-3 core ID ($[Cl^-]_{interface@2-inch} = 4,265$ ppm).....	98
Figure 101. Photo. Close-up view of the bar shown in figure 100.....	98
Figure 102. Photo. Rust spot and two pits observed on an SCR1 sample from slab 2L with a 6-1 core ID ($[Cl^-]_{interface@2-inch} = 1,578$ ppm).....	99
Figure 103. Photo. Small pits on another SCR1 sample from slab 2L with a 1-3 core ID ($[Cl^-]_{interface@2-inch} = 1,628$ ppm).....	99
Figure 104. Photo. Extracted ECR from slab 2R with a 1-1 core ID ($[Cl^-]_{interface@2-inch} = 353$ ppm).....	100
Figure 105. Photos. Close-up view of the bar shown in figure 104.....	100
Figure 106. Photos. Knife adhesion test results on the bar shown in figure 104.....	100
Figure 107. Photo. Extracted ECR from slab 2R with a 5-1 core ID ($[Cl^-]_{interface@2-inch} = 1,745$ ppm).....	101
Figure 108. Photos. Close-up views of the bar shown in figure 107.....	101
Figure 109. Photos. Knife adhesion test results on the bar shown in figure 107.....	101
Figure 110. Photo. Extracted ECR from slab 2R with a 2-3 core ID ($[Cl^-]_{interface@2-inch} = 1,332$ ppm).....	102
Figure 111. Photos. Close-up views of the bar shown in figure 110 before and after an artificial coating defect was peeled off.....	102
Figure 112. Photo. Second close-up view of the bar shown in figure 110.....	102
Figure 113. Photos. The most significant disbondment on an ECR from slab 2R with a 5-3 core ID ($[Cl^-]_{interface@2-inch} = 1,434$ ppm).....	103
Figure 114. Photos. Coating backside contamination of an ECR from slab 2R with a 2-3 core ID ($[Cl^-]_{interface@2-inch} = 1,332$ ppm).....	103
Figure 115. Photo. Extracted ECR from slab 3L with a 2-1 core ID ($[Cl^-]_{interface@2-inch} = 1,026$ ppm).....	104
Figure 116. Photos. Close-up views of the bar shown in figure 115.....	104
Figure 117. Photo. Extracted ECR from slab 3L with a 6-3 core ID ($[Cl^-]_{interface@2-inch} = 3,602$ ppm).....	104

Figure 118. Photos. Close-up views of the bar shown in figure 117.	105
Figure 119. Photo. Condition beneath a defect from slab 3L with a 5-1 core ID ($[Cl]_{interface@2-inch} = 1,374$ ppm).	105
Figure 120. Photo. Coating backside of an ECR from slab 3L with a 5-2 core ID ($[Cl]_{interface@2-inch} = 2,153$ ppm).	106
Figure 121. Photo. Extracted SCR2 from slab 3R with a 1-1 core ID ($[Cl]_{interface@2-inch} =$ 1,341 ppm).	106
Figure 122. Photo. Close-up view of the bar shown in figure 121.	107
Figure 123. Photo. Extracted SCR2 from slab 3R with a 2-1 core ID ($[Cl]_{interface@2-inch} =$ 4,523 ppm).	107
Figure 124. Photo. Close-up view of the bar shown in figure 123.	108
Figure 125. Photo. Extracted SCR2 from slab 3R with a 2-2 core ID ($[Cl]_{interface@2-inch} =$ 3,080 ppm).	108
Figure 126. Photo. Close-up view of manufacturing defects and rust spots shown in figure 125.	109
Figure 127. Photo. Visible gap along the rib of an SCR2 from slab 3R with a 5-2 core ID ($[Cl]_{interface@2-inch} = 4,299$ ppm).	109
Figure 128. Photo. Extracted LSS2 from slab 4L with a 1-3 core ID ($[Cl]_{interface@2-inch} =$ 641 ppm).	110
Figure 129. Photo. Close-up view of the bar shown in figure 128.	110
Figure 130. Photo. Extracted LSS2 from slab 4L with a 5-2 core ID ($[Cl]_{interface@2-inch} =$ 2,713 ppm).	110
Figure 131. Photo. Close-up view of the bar shown in figure 130.	111
Figure 132. Photo. Extracted HDG from slab 4R with a 1-1 core ID ($[Cl]_{interface@2-inch} =$ 785 ppm).	111
Figure 133. Photo. Close-up view of the bar shown in figure 132.	111
Figure 134. Photo. Extracted HDG from slab 4R with a 6-2 core ID ($[Cl]_{interface@2-inch} =$ 2,982 ppm).	112
Figure 135. Photo. Close-up view of the bar shown in figure 134.	112
Figure 136. Photos. Remaining zinc coating on the bar shown in figure 132.	113
Figure 137. Photos. Close-up view of an extracted HDG from slab 4R with a 5-2 core ID ($[Cl]_{interface@2-inch} = 2,410$ ppm).	113
Figure 138. Photo. Bar imprint in slab 4R with a 2-1 core ID ($[Cl]_{interface@2-inch} = 854$ ppm)....	114
Figure 139. Photo. Matching HDG for the imprint shown in figure 138.	114
Figure 140. Photo. Rebar imprint in slab 4R with a 2-2 core ID ($[Cl]_{interface@2-inch} = 2,233$ ppm).	114
Figure 141. Photo. Matching HDG for the imprint shown in figure 140.	115
Figure 142. Photo. Extracted HSR from slab 5L with a 5-3 core ID ($[Cl]_{interface@2-inch} = 961$ ppm).	115
Figure 143. Photo. Close-up view of the bar shown in figure 142.	116
Figure 144. Photo. Extracted HSR from slab 5L with a 5-2 core ID ($[Cl]_{interface@2-inch} =$ 2,398 ppm).	116
Figure 145. Photo. Close-up view of the bar shown in figure 144.	117
Figure 146. Photo. Cracked slab 5L with a 2-1 core ID ($[Cl]_{interface@2-inch} = 6,630$ ppm).	117

Figure 147. Photo. Corroded HSR extracted from the core shown in figure 146.....	118
Figure 148. Photo. Extracted SSR1 from slab 5R with a 1-1 core ID ($[Cl^-]_{interface@2-inch} = 774$ ppm).	118
Figure 149. Photo. Close-up view of the bar shown in figure 148.	118
Figure 150. Photo. Extracted SSR1 from slab 5R with a 2-3 core ID ($[Cl^-]_{interface@2-inch} = 4,153$ ppm).	119
Figure 151. Photo. Close-up view of the bar shown in figure 150.	119
Figure 152. Photo. Second close-up view of the bar shown in figure 150.	119
Figure 153. Photo. Corrosion of an SSR1 from slab 5R with a 1-2 core ID ($[Cl^-]_{interface@2-inch} = 1,841$ ppm).	120
Figure 154. Photo. Corrosion of a second SSR1 from slab 5R with a 6-2 core ID ($[Cl^-]_{interface@2-inch} = 2,446$ ppm).	120
Figure 155. Photo. Extracted LSS1 from slab 6L with a 6-1 core ID ($[Cl^-]_{interface@2-inch} = 621$ ppm).	120
Figure 156. Photo. Close-up view of the bar shown in figure 155.	121
Figure 157. Photo. Extracted LSS1 from slab 6L with a 6-3 core ID ($[Cl^-]_{interface@2-inch} = 2,936$ ppm).	121
Figure 158. Photo. Close-up view of the bar shown in figure 157.	121
Figure 159. Photo. Extracted DCR from slab 6R with a 1-1 core ID ($[Cl^-]_{interface@2-inch} = 305$ ppm).	122
Figure 160. Photos. Close-up views of the bar shown in figure 159.	122
Figure 161. Photo. A second autopsied area of the bar shown in figure 159.	123
Figure 162. Photos. Removed coating from the bar shown in figure 159.	123
Figure 163. Photo. Extracted DCR from slab 6R with a 1-3 core ID ($[Cl^-]_{interface@2-inch} = 2,138$ ppm).	124
Figure 164. Photo. Close-up view of the bar shown in figure 163.	124
Figure 165. Photos. Autopsy of the area shown in figure 164.	124
Figure 166. Photo. Coating fragments removed from the area shown in figure 165.	125
Figure 167. Photo. Extracted SSR2 from slab 7L with a 1-3 core ID ($[Cl^-]_{interface@2-inch} = 330$ ppm).	125
Figure 168. Photo. Extracted SSR2 from slab 7L with a 2-2 core ID ($[Cl^-]_{interface@2-inch} = 2,452$ ppm).	125
Figure 169. Photo. Close-up view of an SSR2 from slab 7L with a 6-2 core ID ($[Cl^-]_{interface@2-inch} = 932$ ppm).	126
Figure 170. Photo. Sliver on the bar shown in figure 169.	126
Figure 171. Photo. Extracted SSR3 from slab 7R with a 5-1 core ID ($[Cl^-]_{interface@2-inch} = 765$ ppm).	127
Figure 172. Photo. Close-up view of the bar shown in figure 171.	127
Figure 173. Photo. Extracted SSR3 from slab 7R with a 1-3 core ID ($[Cl^-]_{interface@2-inch} = 4,288$ ppm).	127
Figure 174. Photo. Close-up view of the bar shown in figure 173.	128
Figure 175. Photo. Rust on the bar shown in figure 173.	128
Figure 176. Photo. Powderous corrosion product on an SSR3 bar sample from slab 7R with a 2-3 core ID ($[Cl^-]_{interface@2-inch} = 4,012$ ppm).	129
Figure 177. Graph. $i_{macro-cell}$ versus time plot for high absolute current group.	130

Figure 178. Graph. $i_{\text{macro-cell}}$ versus time plot for low absolute current group.	130
Figure 179. Graph. Mean $i_{\text{macro-cell}}$	131
Figure 180. Graph. Normalized mean R_p versus mean $i_{\text{macro-cell}}$	132
Figure 181. Photo. Black bars.	135
Figure 182. Photo. ECR bars.	136
Figure 183. Photo. DCR bars.	136
Figure 184. Photo. HDG bars.	137
Figure 185. Photo. SCR1 bars.	137
Figure 186. Photo. SCR2 bars.	138
Figure 187. Photo. SSR1 bars.	138
Figure 188. Photo. Pickled SSR1 bars.	139
Figure 189. Photo. SSR2 bars.	139
Figure 190. Photo. SSR3 bars.	140
Figure 191. Photo. HSR bars.	140
Figure 192. Photo. LSS1 bars.	141
Figure 193. Photo. LSS2 bars.	141
Figure 194. Photo. View from above of a suspended bar in an empty mold.	142
Figure 195. Photo. Slab #1 bars.	143
Figure 196. Photo. Slab #2 bars.	143
Figure 197. Photo. 4- by 8-inch cylindrical molds ready for casting.	144
Figure 198. Photo. Slab #1 mold.	144
Figure 199. Photo. Slab #2 mold.	145
Figure 200. Photo. Specimen curing.	145
Figure 201. Photo. Demolded concrete specimens.	146
Figure 202. Photo. OCP and LPR measurements of a cylindrical specimen.	146
Figure 203. Photo. OCP and $I_{\text{macro-cell}}$ measurements of slab #2 specimen.	147
Figure 204. Photo. Cylindrical specimens in a plastic container.	147
Figure 205. Photo. Arrangement of specimens in a temporary heat tent with lid removed.	148
Figure 206. Graph. Mean OCP versus time plot for the best and poorest performance bars in the cylindrical specimens.	149
Figure 207. Graph. OCP versus time plot for the best and poorest performance bars in the slab specimens.	149
Figure 208. Graph. Mean OCP versus time plot for intermediate performance bars in the cylindrical specimens.	150
Figure 209. Graph. OCP versus time plot for intermediate performance bars in the slab specimens.	150
Figure 210. Graph. Mean OCP versus time plot for as-received SSR1 and pickled SSR1 in the cylindrical specimens.	151
Figure 211. Graph. Baseline R_p data.	152

LIST OF TABLES

Table 1. Types and characteristics of metallic reinforcing bars employed.	4
Table 2. Four levels of coating damage.	8
Table 3. Detailed damage conditions on individual coated bars.	11
Table 4. Chloride concentrations of selective bars at 102 d exhibiting OCP more negative than $-0.300 V_{CSE}$ and two bottom mats exposed to salt water.	67
Table 5. Chloride concentrations at 193 d based on the most positive and negative OCPs per slab section.	68
Table 6. Black bar autopsy results (slab 1L).	70
Table 7. Black bar autopsy results (slab 8L).	71
Table 8. Black bar (1-inch cover) autopsy results (slab 1R).	72
Table 9. Black bar (1-inch cover) autopsy results (slab 8R).	74
Table 10. SCR1 autopsy results (slab 2L).	76
Table 11. ECR with black bar bottom mat autopsy results (slab 2R).	77
Table 12. ECR autopsy results (slab 3L).	80
Table 13. SCR2 autopsy results (slab 3R).	82
Table 14. LSS2 autopsy results (slab 4L).	83
Table 15. HDG autopsy results (slab 4R).	84
Table 16. HSR autopsy results (slab 5L).	85
Table 17. SSR1 autopsy results (slab 5R).	86
Table 18. LSS1 autopsy results (slab 6L).	87
Table 19. DCR autopsy results (slab 6R).	88
Table 20. SSR2 autopsy results (slab 7L).	90
Table 21. SSR3 autopsy results (slab 7R).	91
Table 22. Key statistical parameters of final chloride data.	92
Table 23. Mean chloride diffusion coefficients of test slabs.	93

LIST OF ABBREVIATIONS AND SYMBOLS

Abbreviations

AASHTO	American Association of State Highway and Transportation Officials
AC	alternating current
Ag/AgCl	silver–silver chloride
Cl ⁻	chloride ion
CV	coefficient of variance
CSE	copper–copper sulfate reference electrode
DCR	dual-coated reinforcing steel
ECR	epoxy-coated reinforcing steel
FDOT	Florida Department of Transportation
FHWA	Federal Highway Administration
HDG	hot-dip galvanized reinforcing steel
HSR	high-strength micro-composite reinforcing steel
ID	identification
LPR	linear polarization resistance
LSS1	lean duplex solid stainless reinforcing steel with 12 percent chromium
LSS2	ferritic solid stainless reinforcing steel with 12 percent chromium
NaCl	sodium chloride
NDE	nondestructive evaluation
OCP	open circuit potential
PT	post-tensioned
PVC	polyvinyl chloride
R ²	coefficient of determination
RCPT	rapid chloride permeability test

RE	reference electrode
R_p	polarization resistance
SCR1	type 1 stainless steel–clad reinforcing steel
SCR2	type 2 stainless steel–clad reinforcing steel
SSR1	duplex solid stainless reinforcing steel with 21 percent chromium
SSR2	duplex solid stainless reinforcing steel with 23 percent chromium
SSR3	austenitic solid stainless reinforcing steel
UNS	unified numbering system
V_{CSE}	potential in volt versus copper–copper sulfate reference electrode

Symbols

$[Cl^-]_{\text{interface@2-inch}}$	chloride concentration at a bar depth of 2 inches
i_{corr}	corrosion current density
I_{corr}	corrosion current
$i_{\text{macro-cell}}$	macro-cell corrosion current density
$I_{\text{macro-cell}}$	macro-cell corrosion current

CHAPTER 1. INTRODUCTION

Steel, in concrete, corrodes when the concentration of chloride ions (Cl^-) exceeds the threshold level at the reinforcing steel surface. This usually occurs after the concrete is exposed to anti-icing agents and deicers for snow removal or when the structure is located in or near a marine environment. The minimum chloride concentration to initiate corrosion is called the “chloride threshold.” Corrosion is also caused by the carbonation of concrete surrounding the steel. These two corrosion mechanisms are responsible for initiating the corrosion of ordinary reinforcing steel (black bar) by compromising a protective, invisible oxide film that is formed on the steel surface due to the high alkalinity (pH greater than 12.5) of uncontaminated concrete.

Until several decades ago, black bar was the most frequently used reinforcement material for reinforced concrete structures, including bridges and other types of transportation infrastructure. While black bar is the least expensive and the most available reinforcement, it has a weak corrosion resistance. Black bar generally initiates corrosion when the chloride concentration exceeds a threshold as low as 250 ppm and/or a pH below 10 in most service environments. The resultant corrosion product is known to produce three to six times more volume, depending on the oxide state, than the bar itself.⁽¹⁾ Since concrete has low tensile strength (about 10 percent of its compressive strength), active corrosion results in concrete cracking in the presence of excessive hoop stress around the corroding bar. Ultimately, serious concrete deterioration occurs in the form of large cracks, delamination, and spalling, which allow more water, chloride, and oxygen to reach the reinforcement and thus accelerate the ongoing corrosion. The typical life expectancy of northern bridge decks in the United States containing black bars is only 15–20 yr.

In the late 1970s, epoxy-coated reinforcing steel (ECR) was found to be superior to black steel. There are more than 100,000 structures containing ECR in the United States. Various laboratory and field studies indicate that ECR decks provide longer service life with minimal maintenance than black bar bridge decks, especially when ECR is used in both mats. The extended service life offered by ECR is projected to be more than 75 yr if high-quality ECR is used. Care must be taken to ensure that minimal coating damage is sustained from production in the coating plant to concrete placement in the field. Conversely, poor performance of ECR has been reported in some other studies in which ECR behaved similarly to black bar. A significant contributing factor for the poor performance is coating disbondment (or loss of adhesion, which may occur either in production or during installation). Corrosion of ECR is always associated with coating disbondment, but not all disbonded coating areas lead to corrosion.

Amid controversies surrounding ECR, the steel industry responded by developing various types of corrosion-resistant alloy reinforcing steel. At one point, end users, including bridge design engineers, maintenance engineers, and consultants, had more than 15 products to choose from. Such an influx of different bar materials into the market created confusion and a knowledge gap among the end users as they were not prepared to choose the right materials for their applications due to a lack of unbiased corrosion performance data, especially for the new products.

Therefore, the Federal Highway Administration’s (FHWA) Coatings and Corrosion Laboratory launched an in-house research study in 2009. The objective of the study was to evaluate the

corrosion resistance of 12 alternative reinforcing materials, including ECR, galvanized bars with and without epoxy coating, corrosion-resistant alloy bars, stainless steel-clad bars, and solid stainless steel bars in the same accelerated corrosion testing environment. This report presents experimental details including materials employed in this study and test methods and procedures, test results and discussion, and conclusions.

CHAPTER 2. MATERIALS AND EXPERIMENTAL PROCEDURES

BAR MATERIALS

During the experimental design stage of this study in 2008, there were more than 15 different products available in the steel reinforcement market. Among them, some solid stainless steel products, such as types 316L, 304L, and 2205, had already demonstrated excellent corrosion resistance with plenty of supporting data. Therefore, the present study excluded those well-performing products. Individual products are identified by their specification/designation numbers given by ASTM International, the American Association of State Highway and Transportation Officials (AASHTO), and the unified numbering system (UNS). If a product has more than one designation, it is referred to by the first designation listed in table 1. Also, dual-coated reinforcing steel (DCR) is included in two groups, as it is coated with a thin zinc layer followed by a fusion-bonded epoxy coating. Throughout this report, products are identified by their abbreviations rather than their commercial names and specification/designation numbers. Unfortunately, most of the bar materials were provided by individual suppliers without useful information such as grade, heat treatment, and pickling.

Table 1 summarizes each product with governing specification, bar abbreviation, material characteristics, and acquired bar size. Products are categorized into the following six groups (that also provide bar designation abbreviations) based on the type of material:

1. **Control:** Black reinforcing steel (i.e., black bar) (ASTM A615).⁽²⁾
2. **Fusion-bonded epoxy coating:** ECR (ASTM A775) and DCR (ASTM A1055).^(3,4)
3. **Metallic coating:** Hot-dip galvanized reinforcing steel (HDG) (ASTM A767) and DCR (ASTM A1055).^(5,4)
4. **Stainless steel–clad:** Types 1 and 2 stainless-clad reinforcing steel (SCR1 and SCR2) (AASHTO M 329M).⁽⁶⁾
5. **Solid stainless steel:** Duplex solid stainless reinforcing steel with 21 percent chromium (SSR1) (UNS S32101), duplex solid stainless reinforcing steel with 23 percent chromium (SSR2) (UNS S32304), and austenitic solid stainless reinforcing steel (SSR3) (UNS S24100).^(7,8)
6. **Other corrosion-resistant alloys:** High-strength micro-composite reinforcing steel (HSR) (ASTM A1035), lean duplex solid stainless reinforcing steel with 12 percent chromium (LSS1) (ASTM A1010), and ferritic solid stainless reinforcing steel with 12 percent chromium (LSS2) (ASTM A240).^(9,10,7)

Table 1. Types and characteristics of metallic reinforcing bars employed.

Group ID	Abbreviation of Bar Type Used in This Report	Relevant Specification/ Designation	Material Characteristics	Acquired Bar Size
1	Black	ASTM A615 ⁽²⁾	Conventional uncoated carbon steel	#6
2	ECR	ASTM A775 ⁽³⁾	Conventional fusion-bonded epoxy coated steel	#5
2, 3	DCR	ASTM A1055 ⁽⁴⁾	2-mil zinc coating plus 8-mil fusion-bonded epoxy coating	#5
3	HDG	ASTM A767 ⁽⁵⁾	Hot-dip galvanized	#5
4	SCR1	AASHTO M 329M/M 329-11 ⁽⁶⁾	316 stainless cladding by a spraying process over carbon steel core, clad thickness less than 10 mil	#5
4	SCR2	AASHTO M 329M/M 329-11 ⁽⁶⁾	316L stainless cladding, minimum cladding thickness of 7 mil (typically 14–35 mil)	#6
5	SSR1	UNS S32101 ⁽⁷⁾	21 percent chromium duplex solid stainless steel	#5
5	SSR2	UNS S32304 ⁽⁷⁾	23 percent chromium duplex solid stainless steel	#5
5	SSR3	UNS S24100 ⁽⁷⁾	16.5–19.0 percent chromium, high-manganese, low-nickel, nitrogen-strengthened austenitic solid stainless steel	#5
6	HSR	ASTM A1035/ AASHTO MP 18M/MP 18-09 ^(9,11)	High-strength, low-carbon, chromium alloy, micro-composite	#5
6	LSS1	ASTM A1010/ UNS S41003 ⁽¹⁰⁾	12 percent chromium lean duplex solid stainless steel	#5
6	LSS2	ASTM A240/ UNS S41003 ⁽⁷⁾	12 percent chromium ferritic solid stainless steel	#5

Figure 1 shows some of the bar products as they were delivered for testing. It was assumed that the acquired products were representative of those sold to actual construction projects and that they conformed to their respective specifications, including pickling treatment, if required. As such, they were tested with as-received surface condition. The only exception was that artificial coating defects were introduced to some of the coated bars to simulate field conditions (which is discussed further in the next section related to table 2 and figure 3). The other products (i.e., LSS2 and SSR1) were donated by the Florida Department of Transportation (FDOT). These bars were left over from earlier unpublished FDOT studies.



Source: FHWA.

Figure 1. Photo. Bar samples acquired from 11 sources.

The following subsections describe individual products briefly based on major material characteristics, chemical composition, and additional information gathered from the supplier brochures and an online search.

Black Reinforcing Steel

Conventional black (uncoated) bar conforming to ASTM A615 was chosen as a control material that defines the least corrosion resistance.⁽²⁾

ECR

ECR, which is a fusion-bonded epoxy coated bar, is produced per ASTM A775.⁽³⁾ The coating appearance of ECR used in this study was satisfactory, but a large number of as-received coating defects (holidays and mechanical damage) were found with a low-voltage holiday detector (for detecting invisible pinholes) and by visual examination. The measured average coating thickness was 9.6 mil with a standard deviation of 1.4 mil. This range of coating thickness satisfied the standard requirement (7–12 mil for a #5 bar (with 0.625-inch diameter) and 7–16 mil for bar size #6 (with 0.75-inch diameter) or greater). The bent bars did not contain hairline coating cracks near the bent sections. The detached coating fragments did not exhibit excessive backside contamination.

DCR

DCR is produced per ASTM A1055.⁽⁴⁾ It consists of two coats: a minimum 1.4-mil-thick, arc-sprayed zinc layer covered by a layer of fusion-bonded epoxy coating similar to the ECR coating. The combined coating thickness is required to be 7–12 mil for bar sizes up to #5 and 7–16 mil for bar sizes #6 or greater. For this study, the coating appearance was excellent without any blemishes. A small number of as-received coating defects were found on each bar sample with a low-voltage holiday detector and by visual examination. The measured average total coating thickness was 7.6 mil with a standard deviation of 1.2 mil. Therefore, some of the

measured dual-coating thickness data were lower than the ASTM specification. The bent bars did not contain hairline coating cracks. As expected, the backside of the peeled epoxy coating had a layer of zinc-coating residue. Additional detail is provided in the Autopsy of Test Slabs section later in this chapter.

HDG

This bar material, which requires a chromate treatment after galvanizing, conforms to ASTM A767.⁽⁵⁾ For this study, the zinc coating had a rough surface with scattered, small zinc lumps. The measured average total coating thickness was 2.0 mil with a standard deviation of 0.5 mil. The zinc thickness was thinner than that (i.e., 3.4 mil) of typical HDG. The bent bars did not contain hairline coating cracks.

SCR1

This bar material conforms to AASHTO M 329M/M 329-11.⁽⁶⁾ It is a 316 grade SCR and is produced by plasma-spraying stainless steel to a carbon steel billet and then rolling.⁽¹¹⁾ The specified cladding thickness and chemical composition are not known as of the date that this report was published.

SCR2

This bar material also conforms to AASHTO M 329M/M 329-11.⁽⁶⁾ It is a 316L (i.e., low-carbon steel) SCR that is metallurgically bonded to a carbon steel core. The minimum cladding thickness is specified to be 7 mil, but it usually varies from 14 to 35 mil.⁽¹²⁾ Its typical chemical composition consists of carbon (0.030 percent maximum), chromium (16 to 18 percent), manganese (2 percent maximum), silicon (0.750 percent maximum), sulfur (0.030 percent maximum), phosphorus (0.045 percent maximum), nickel (10 to 14 percent), and molybdenum (2 to 3 percent).⁽¹²⁾

SSR1

This bar material is designated as UNS S32101 and conforms to the physical specifications of ASTM A955/A955M.^(7,8) It is a duplex (austenite plus ferrite) solid stainless steel. When the samples were acquired from FDOT for this study, they were labeled as “2201.” However, the principal investigator of this study believed that these bars were marked as 2201 in error and that the correct designation should be UNS S32101. In addition, the bar samples in question might not meet the pickling requirement specified by ASTM A955.⁽⁸⁾ Therefore, this report designates the bar material as UNS S32101 and assumes that it did not receive proper pickling treatment. Additional bars were tested in a follow-up laboratory study after they were pickled by a stainless steel producer. Test results included in chapter 4 confirmed that the original bar samples were not properly pickled. Its chemical composition includes carbon (0.040 percent), chromium (22.470 percent), manganese (4.700 percent), silicon (0.800 percent), sulfur (0.001 percent), phosphorus (0.019 percent), copper (0.380 percent), nickel (1.680 percent), and molybdenum (0.240 percent).⁽¹³⁾

SSR2

This bar material is designated as UNS S32304 and conforms to the physical specifications of ASTM A955/A955M.^(7,8) It is another duplex solid stainless steel. In this study, this product was included as potentially the most corrosion-resistant alloyed material. Its chemical composition includes carbon (0.030 percent), chromium (22.330 percent), manganese (1.160 percent), silicon (0.450 percent), sulfur (0.002 percent), phosphorus (0.026 percent), copper (0.300 percent), nickel (4.160 percent), and molybdenum (0.250 percent).⁽¹³⁾

SSR3

This bar material is designated as UNS S24100 and conforms to the physical specifications of ASTM A955/A955M.^(7,8) It is an austenitic solid stainless steel with high manganese and low nickel and is strengthened by extra nitrogen via solid solution strengthening mechanism.⁽¹⁴⁾ Its chemical composition includes carbon (0.060 percent max), chromium (16.500 to 19.000 percent), manganese (11 to 14 percent), silicon (1 percent maximum), sulfur (0.030 percent maximum), phosphorus (0.060 percent maximum), nickel (0.500 to 2.500 percent), and nitrogen (0.200 to 0.450 percent).⁽¹⁴⁾

HSR

This bar material conforms to ASTM A1035/AASHTO MP 18M/MP 18-09.^(9,11) It is a high-strength, low-carbon, chromium alloy steel. HSR possesses a different microstructure from ordinary carbon steel (a laminated lath microstructure), which minimizes the formation of micro-galvanic cells. The material properties are superior to those of ordinary carbon steel, which contains a matrix of ferrites and carbides, in terms of strength, ductility, toughness, and corrosion resistance. HSR's chemical composition includes carbon (0.050 percent), chromium (9.300 percent), manganese (0.450 percent), silicon (0.230 percent), sulfur (0.015 percent), phosphorus (0.012 percent), copper (0.120 percent), nickel (0.100 percent), and molybdenum (0.030 percent).⁽¹³⁾

LSS1

This bar material conforms to ASTM A1010 and UNS S41003.⁽¹⁰⁾ It also conforms to the physical specifications of ASTM A955/A955M.⁽⁸⁾ It is a duplex solid stainless steel containing 12 percent chromium. It is claimed to be more corrosion resistant than weathering steel, painted steel, and galvanized steel. Its chemical composition includes carbon (0.025 percent), chromium (11.000 to 12.500 percent), manganese (1.500 percent), silicon (0.700 percent), sulfur (0.010 percent), phosphorus (0.040 percent), nickel (1.000 percent), and molybdenum (0.200 to 0.350 percent).⁽¹⁵⁾

LSS2

This bar material is certified to ASTM A240 and UNS S41003.⁽⁷⁾ It also conforms to the physical specifications of ASTM A955/A955M.⁽⁸⁾ It is a ferritic utility solid stainless steel containing 12 percent chromium.⁽¹⁶⁾ Its chemical composition includes carbon (0.040 percent), chromium (11.690 percent), manganese (0.380 percent), silicon (0.710 percent), sulfur (0.024 percent),

phosphorus (0.018 percent), copper (0.020 percent), nickel (0.500 percent), and molybdenum (0.090 percent).⁽¹³⁾

INTRODUCTION OF ARTIFICIAL DEFECTS

Mechanical coating damages were made intentionally on some of the coated bars that had soft protective layers to simulate realistic damage conditions. Table 2 lists four levels of total coating damage on the selected ECR, DCR, and HDG bars. Initially, the researchers attempted to make artificial defects for stainless steel-clad bars. However, it became clear that making such defects was not realistic, as it required significant effort to drill through the cladding. It was determined that the specified and measured thickness of the cladding makes mechanical damage in the field unlikely to occur. Consequently, the attempt to introduce mechanical defects on the clad bars was abandoned, and all clad bars were tested without artificial damage.

Table 2. Four levels of coating damage.

Damage Level per Mat (Percent of Total Surface Area)	Number of Defects Based on 0.125-Inch Artificial Defect Size (ECR, DCR, and HDG)		
	Straight Bar		Bent Bar
	Transverse	Longitudinal	Transverse
0–0.05	0	3	—
0.15	4	10	7
0.5	14	30	—
1.0	29	—	—

—No defect was introduced.

As the first step of introducing target coating damage, as-received (natural) coating defects on ECR and DCR were located using a low-voltage holiday detector. Figure 2 shows five as-received coating defects identified on an ECR, which are circled in black.



Source: FHWA.

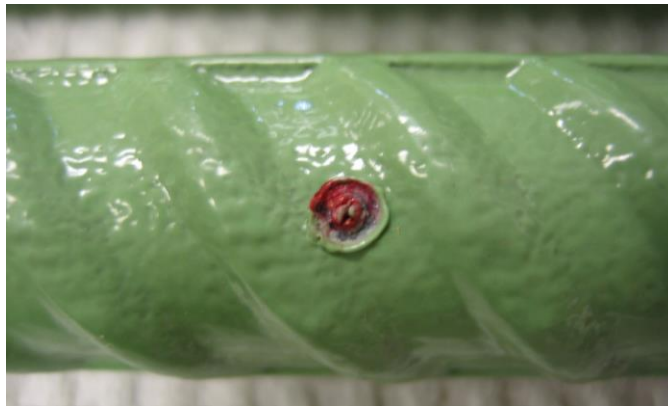
Figure 2. Photo. Example of as-received ECR defects.

If a target damage level (as identified in table 2) could not be met by the number of as-received defects, more coating defects were artificially introduced using a 0.125-inch puncher with an assumption that each as-received defect is equivalent to an artificial defect made with the puncher. Figure 3 and figure 4 show the creation of an artificial coating defect and a close-up view of such a defect on an ECR, respectively. The red dot in figure 4 was used to indicate where an artificial defect would be made. The red permanent marker did not influence the outcome of the study.



Source: FHWA.

Figure 3. Photo. Creation of artificial coating damage.



Source: FHWA.

Figure 4. Photo. Close-up view of an artificial coating damage on an ECR.

Figure 5 shows a photograph of five ECR bars that contained as-received defects (indicated by black circles) and artificial defects (indicated by red dots). Figure 6 shows typical intentional damage created on an HDG bar (indicated by a red dot).



Source: FHWA.

Figure 5. Photo. ECR samples with various types of coating damage.



Source: FHWA.

Figure 6. Photo. Close-up view of an artificial coating damage on an HDG.

FABRICATION OF CONCRETE TEST SLABS

Table 3 summarizes the final coating damage conditions of every ECR, DCR, and HDG used in this study. A unique slab identification system was used: slabs 1 through 8 refer to the large slabs and use the letters “L” and “R” to indicate the left and right slab sections, respectively. For example, slab 3L stands for the left slab section of large slab 3. The left and right sections were two independent test slabs contained in a large slab.

Table 3. Detailed damage conditions on individual coated bars.

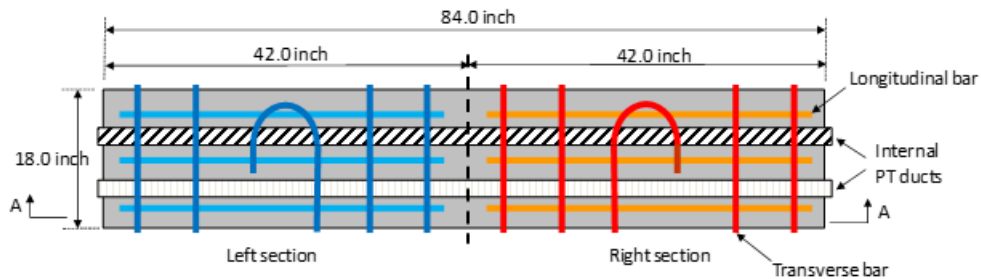
Bar Type (Slab ID)	Bar ID	Mat and Orientation	Bar Shape	Length (Inches)	Damage Level (Percent)	Number of As- Received Defects	Number of 0.125-Inch Artificial Defects	Total Number of Defects
ECR + black (slab 2R)	R1	Top transverse	Straight	18	0.00	0	0	0
ECR + black (slab 2R)	R2	Top transverse	Straight	18	0.15	4	0	4
ECR + black (slab 2R)	R3	Top transverse	Bent	30	0.15	1	6	7
ECR + black (slab 2R)	R4	Top transverse	Straight	18	0.50	3	11	14
ECR + black (slab 2R)	R5	Top transverse	Straight	18	1.00	5	24	29
ECR + black (slab 2R)	R6	Top longitudinal	Straight	38	0.15	10	0	10
ECR + black (slab 2R)	R7	Top longitudinal	Straight	38	0.50	4	26	30
ECR + black (slab 2R)	R8	Top longitudinal	Straight	38	0.04	3	0	3
ECR (slab 3L)	L1	Top transverse	Straight	18	0.00	1	0	1
ECR (slab 3L)	L2	Top transverse	Straight	18	0.15	2	2	4
ECR (slab 3L)	L3	Top transverse	Bent	30	0.15	7	0	7
ECR (slab 3L)	L4	Top transverse	Straight	18	0.50	2	12	14
ECR (slab 3L)	L5	Top transverse	Straight	18	1.00	6	23	29
ECR (slab 3L)	L6	Top longitudinal	Straight	38	0.04	2	1	3
ECR (slab 3L)	L7	Top longitudinal	Straight	38	0.50	11	19	30
ECR (slab 3L)	L8	Top longitudinal	Straight	38	0.15	10	0	10
ECR (slab 3L)	L1	Bottom transverse	Straight	18	0.00	1	0	1
ECR (slab 3L)	L2	Bottom transverse	Straight	18	0.15	4	0	4
ECR (slab 3L)	L3	Bottom transverse	Bent	30	0.15	3	4	7
ECR (slab 3L)	L4	Bottom transverse	Straight	18	0.50	3	11	14
ECR (slab 3L)	L5	Bottom transverse	Straight	18	1.00	10	19	29
ECR (slab 3L)	L6	Bottom longitudinal	Straight	38	0.50	15	15	30
ECR (slab 3L)	L7	Bottom longitudinal	Straight	38	0.04	3	0	3
ECR (slab 3L)	L8	Bottom longitudinal	Straight	38	0.50	9	1	10
HDG (slab 4R)	R1	Top transverse	Straight	18	0.00	0	0	0
HDG (slab 4R)	R2	Top transverse	Straight	18	0.15	0	4	4
HDG (slab 4R)	R3	Top transverse	Bent	30	0.15	0	7	7
HDG (slab 4R)	R4	Top transverse	Straight	18	0.50	0	14	14
HDG (slab 4R)	R5	Top transverse	Straight	18	1.00	0	29	29
HDG (slab 4R)	R6	Top longitudinal	Straight	38	0.04	0	3	3

Bar Type (Slab ID)	Bar ID	Mat and Orientation	Bar Shape	Length (Inches)	Damage Level (Percent)	Number of As-Received Defects	Number of 0.125-Inch Artificial Defects	Total Number of Defects
HDG (slab 4R)	R7	Top longitudinal	Straight	38	0.50	0	10	10
HDG (slab 4R)	R8	Top longitudinal	Straight	38	0.15	0	30	30
HDG (slab 4R)	R1	Bottom transverse	Straight	18	0.00	0	0	0
HDG (slab 4R)	R2	Bottom transverse	Straight	18	0.15	0	4	4
HDG (slab 4R)	R3	Bottom transverse	Bent	30	0.15	0	7	7
HDG (slab 4R)	R4	Bottom transverse	Straight	18	0.50	0	14	14
HDG (slab 4R)	R5	Bottom transverse	Straight	18	1.00	0	29	29
HDG (slab 4R)	R6	Bottom longitudinal	Straight	38	0.50	0	3	3
HDG (slab 4R)	R7	Bottom longitudinal	Straight	38	0.04	0	10	10
HDG (slab 4R)	R8	Bottom longitudinal	Straight	38	0.50	0	30	30
DCR (slab 6R)	R1	Top transverse	Straight	18	0.00	0	0	0
DCR (slab 6R)	R2	Top transverse	Straight	18	0.15	4	0	4
DCR (slab 6R)	R3	Top transverse	Bent	30	0.15	1	6	7
DCR (slab 6R)	R4	Top transverse	Straight	18	0.50	2	12	14
DCR (slab 6R)	R5	Top transverse	Straight	18	1.00	3	26	29
DCR (slab 6R)	R6	Top longitudinal	Straight	38	0.04	1	2	3
DCR (slab 6R)	R7	Top longitudinal	Straight	38	0.15	2	8	10
DCR (slab 6R)	R8	Top longitudinal	Straight	38	0.50	4	26	30
DCR (slab 6R)	R1	Bottom transverse	Straight	18	0.00	1	0	1
DCR (slab 6R)	R2	Bottom transverse	Straight	18	0.15	4	0	4
DCR (slab 6R)	R3	Bottom transverse	Bent	30	0.15	1	6	7
DCR (slab 6R)	R4	Bottom transverse	Straight	18	0.50	3	11	14
DCR (slab 6R)	R5	Bottom transverse	Straight	18	1.00	2	27	29
DCR (slab 6R)	R6	Bottom longitudinal	Straight	38	0.15	1	9	10
DCR (slab 6R)	R7	Bottom longitudinal	Straight	38	0.04	0	3	3
DCR (slab 6R)	R8	Bottom longitudinal	Straight	38	0.50	4	26	30

Note: ECR + black represents ECR in the top mat and black bar in the bottom mat.

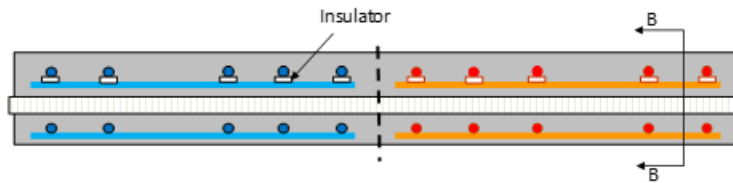
A total of eight large concrete slabs were made for this study. The overall dimensions of the slabs were 7 ft long, 18 inches wide, and 8 inches thick. Figure 7 shows the schematic of a slab that was divided into half-sections. Its elongated shape allowed for the accommodation of two internal post-tensioned (PT) ducts parallel to the slab length at the mid-depth because it was designed to carry out two concurrent studies: the present rebar study and a possible nondestructive evaluation (NDE) study designed for internal PT tendons. As illustrated in figure 7, the internal ducts were not in contact with the reinforcements. This dual configuration was intended to maximize research productivity by performing two studies with a single type of specimen.

Each slab section simulated typical reinforced concrete bridge decks by placing the bars in two depths: a top mat and a bottom mat. With this configuration, a realistic situation of macro-cell corrosion could be established between the top mat as a macro-anode and the bottom mat as a macro-cathode. Upon the arrival of Cl^- in the salt water at the top mat, the macro-anode corroded, and the macro-cathode provided surface area for a cathodic reaction.



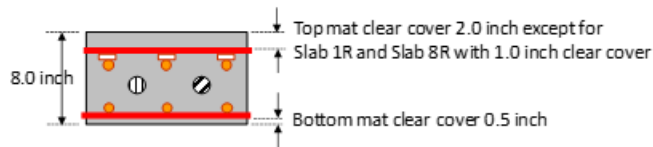
Source: FHWA.

A. Plan view at top mat and bottom mat levels.



Source: FHWA.

B. Cross section A-A.

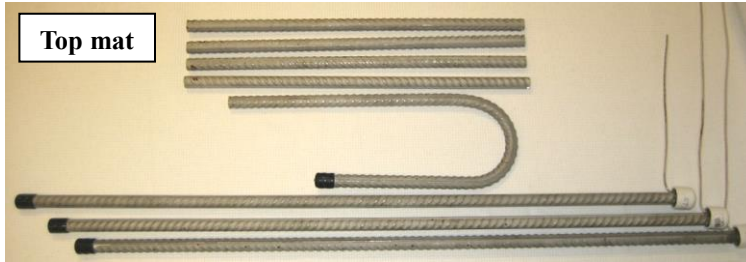


Source: FHWA.

C. Cross section B-B.

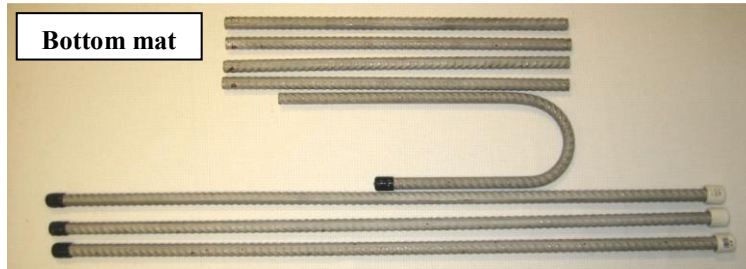
Figure 7. Illustrations. Bar arrangement in concrete slabs.

Like the top mat, the bottom mat consisted of five transverse bars (four straight and one bent) and three straight longitudinal bars, as shown in figure 7-A. A complete set of SCR2 transverse and longitudinal bars is shown in subfigures A and B in figure 8.



Source: FHWA.

A. Top mat SCR2 transverse and longitudinal bars.



Source: FHWA.

B. Bottom mat SCR2 transverse and longitudinal bars.

Figure 8. Photos. Complete set of SCR2 prior to placement in a mold.

All of the bottom transverse and longitudinal bars were made electrically continuous using steel tie wire so that they could act as a single macro-cathode. Even though coated tie wire has been used for ECR in the field for over 20 yr, this study purposely used the uncoated steel tie wire for the sake of electrical continuity of the ECR bottom mat. Such a deviation from the standard field practice was expected to create more severe conditions for ECR compared to electrically isolated cases. Only one electrical connection was made to the bottom mat. Figure 9 shows a bottom mat being fabricated, and figure 10 shows a close-up view of two crossing bars and a tie wire.



Source: FHWA.

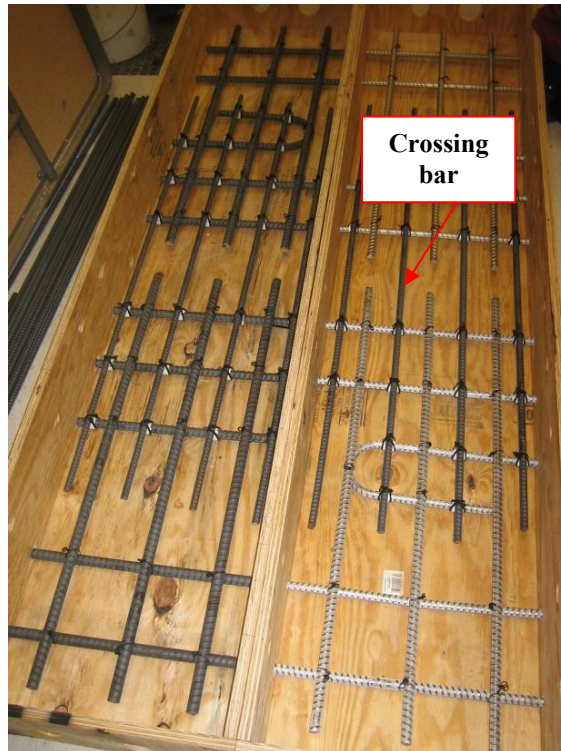
Figure 9. Photo. Fabrication of two bottom mats.



Source: FHWA.

Figure 10. Photo. Close-up view of two crossing bars in the bottom mat.

Figure 11 shows four completed bottom mats placed in two molds. The figure also shows four electrically isolated #4 crossing bars interconnecting two bottom mats. These crossing bars were added to prevent concrete fracture at the boundary between two slab sections during slab handling.



Source: FHWA.

Figure 11. Photo. Completed four bottom mats in two molds.

The top mat utilized a matching set of reinforcement made with the same material. One exception was slab 2R, which was made with ECR in the top mat and black bars in the bottom mat to simulate old ECR concrete bridge decks. Bar arrangement of the top mat was identical to that of the bottom mat as shown in figure 7 and figure 8. However, all of the transverse and longitudinal bars were electrically isolated by placing an insulator between them at every crossing point. This arrangement is illustrated in parts A and B of figure 7, and an actual contact point is shown in figure 12.



Source: FHWA.

Figure 12. Photo. Close-up view of transverse and longitudinal bars in the top mat.

Since individual top mat bars had to be electrically isolated, a separate electrical connection had to be made at one cut end of each bar for corrosion tests. An electrical connection was made by attaching a solid copper wire to one exposed end of each transverse bar. Since longitudinal bars were to be completely embedded in concrete, one cut end of each longitudinal bar was connected to a solid copper wire and then encapsulated with a polyvinyl chloride (PVC) cap and epoxy resin. Figure 13 shows the PVC encapsulation work in progress. Three encapsulated SCR2 longitudinal bars are also shown in figure 8.



Source: FHWA.

Figure 13. Photo. Encapsulating cut ends of top mat longitudinal bars.

Figure 14 shows a top mat being fabricated, and figure 15 shows two completely fabricated top mats, including six longitudinal bars/wires penetrating through a mold. The latter also shows two internal PT ducts installed between top and bottom mats.



Source: FHWA.

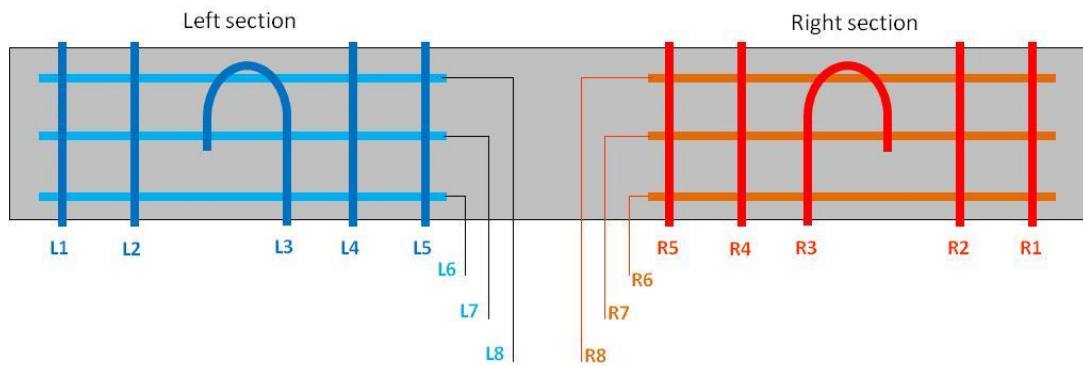
Figure 14. Photo. Fabrication of a top mat.



Source: FHWA.

Figure 15. Photo. Electrical wires attached to longitudinal bars.

Figure 16 shows an identification system for top mat bars. A clear concrete cover for the top mat was set at 2 inches, as shown in figure 17.



Source: FHWA.

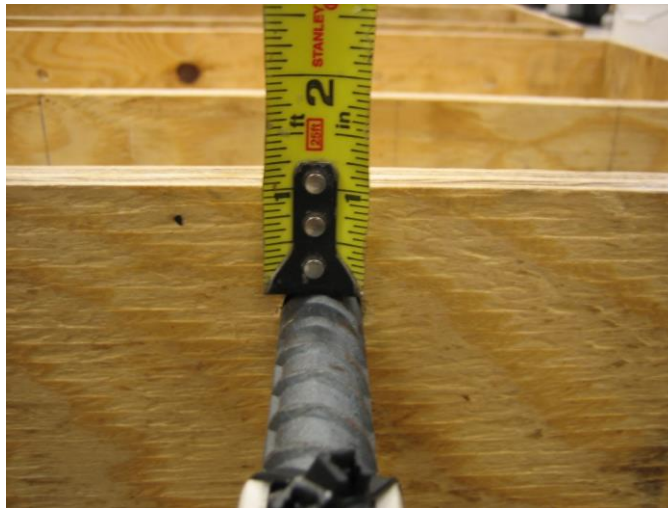
Figure 16. Illustration. Identification of top mat bars.



Source: FHWA.

Figure 17. Photo. Top mat with 2-inch clear cover.

To expedite the corrosion process for some black bars, two slab sections (slab 1R and slab 8R) had a shallow clear cover of 1 inch, as shown in figure 18. This allowed the chloride solution to reach the bars sooner during testing.



Source: FHWA.

Figure 18. Photo. Top mat with 1-inch clear cover.

Figure 19 and figure 20 show several molds containing fully fabricated reinforcements. Figure 21 shows a bird's-eye view of all eight molds ready for concrete casting, and figure 22 shows concrete casting in progress. After 48 h, the slabs were demolded (see figure 23) and placed outdoors under plastic sheets for 26 d of curing with occasional water spray (see figure 24). After completing 28-d curing, the slabs were brought into the FHWA Coatings and Corrosion Laboratory (see figure 25). A ponding well was installed on the top surface of each slab using 2-inch-wide clear PVC strips and a silicon caulking material (see figure 26).

Corrosion potential measurement spots were systematically marked on the top surface using a permanent marker. Three spots were each marked with a plus sign over a transverse bar, and six spots were each marked with an open circle over a longitudinal bar. Therefore, wherever a transverse bar and a longitudinal bar intersected, an open circle filled with a plus sign was included.



Source: FHWA.

Figure 19. Photo. Completed slab sections.



Source: FHWA.

Figure 20. Photo. Second view of completed slab sections.



Source: FHWA.

Figure 21. Photo. Concrete molds ready for casting.



Source: FHWA.

Figure 22. Photo. Concrete casting.



Source: FHWA.

Figure 23. Photo. Demolded concrete slabs.



Source: FHWA.

Figure 24. Photo. Curing of concrete slabs.



Source: FHWA.

Figure 25. Photo. Placement of cured concrete slabs in the laboratory.



Source: FHWA.

Figure 26. Photo. Ponding wells and marking of data measurement spots.

The concrete mix contained 32 percent blast furnace slag, and its water-to-cementitious material ratio was 0.49. A total of 12 (arranged 4 by 8) small cylindrical specimens for compressive strength were also cast along with the large concrete slabs. The cylindrical specimens were moist-cured for 7 d followed by air drying. The mean 28-d compressive strength of three specimens was 3,185 psi. After 90 d, it increased to 3,318 psi based on the same number of specimens. Four cylindrical specimens were employed for a 90-d rapid chloride permeability test (RCPT), which resulted in a mean value of 5,848 C. Such a high RCPT result confirmed that concrete mix yielded fairly porous concrete to accelerate corrosion of reinforcing bars.

ACCELERATED CORROSION TESTING

When the accelerated corrosion testing started, seven slabs were employed, and an eighth slab (slab 8) containing black bars was reserved for the NDE study. Unexpectedly, the first black bar

slab (slab 1) initiated corrosion at its bottom mat first due to leaking salt water traveling down the exterior surfaces to the bottom mat. Consequently slab 8 was added after 283 d to study the corrosion behavior of black bar without the bottom mat being corroded first.

An accelerated corrosion testing protocol was employed for this study. It consisted of a 3-d wetting cycle in 15 weight percent chloride solution at 77 °F and a 4-d drying cycle at 100 °F. The 15 weight percent sodium chloride (NaCl) solution was made with an automated salt water mixer, which agitated a mixture of NaCl and tap water with compressed air overnight. Each wetting cycle used a fresh salt solution. For the drying cycles, the slabs were placed inside four heat tents that were constructed with rigid insulation board and permanently installed in the laboratory. Each heat tent was equipped with three flood lamps and a digital thermostat, which maintained the target temperature with an accuracy of ± 1 °F. During the wetting cycles, the top panel of each heat tent was opened, and a large clear PVC lid was placed over each ponding well to minimize evaporation of the NaCl solution. Figure 27 and figure 28 show the heat tents during a drying cycle and a wetting cycle, respectively.



Source: FHWA.

Figure 27. Photo. Closed heat tents during a drying cycle.

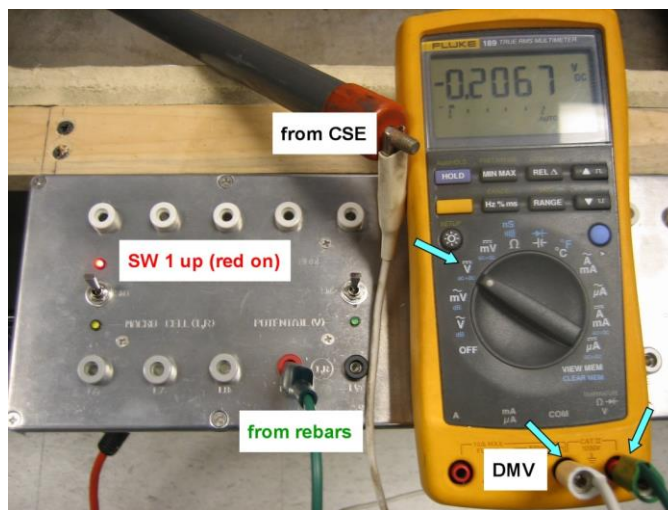


Source: FHWA.

Figure 28. Photo. Opened heat tents during a wetting cycle.

Before starting the corrosion testing, a ponding well leakage test was done for 7 d by filling the ponding wells with tap water. Several leaking ponding wells were repaired, followed by drying for another week. The first wetting cycle started 81 d after the slabs were made.

The corrosion data were collected on a weekly basis for 521 d. A total of 16 custom-made switch boxes were used to collect experimental data from a slab section, as shown in figure 29. The switch box contained circuitry allowing various electrical connections among eight individual bars in the top mat and a single macro-cathode in the bottom mat. Baseline data were collected after 53 d of the accelerated corrosion testing followed by weekly corrosion tests to monitor the state of corrosion for each bar material. In addition, instantaneous rates of corrosion were measured twice toward the end of the accelerated corrosion testing. The following subsection describes corrosion tests employed in this study.



Source: FHWA.

Figure 29. Photo. Data collection switch box.

Corrosion Tests

This study employed the following corrosion testing methods to investigate corrosion characteristics of reinforcing steel in concrete.

Open Circuit Potential (OCP)

OCP (also called “corrosion potential” or “half-cell potential”) indicates a thermodynamic tendency for corrosion of reinforcing steel in concrete to occur or not according to ASTM C876.⁽¹⁷⁾ According to the criteria given in the ASTM standard, an OCP value more positive than -0.200 volts versus copper–copper sulfate reference electrode (CSE) (V_{CSE}) means that there is a 10 percent probability of corrosion, and most bars are in a passive state. An OCP value more negative than $-0.350 V_{CSE}$ indicates a 90 percent probability of corrosion. An OCP range from -0.200 to $-0.350 V_{CSE}$ indicates an uncertain probability of corrosion. Even though those criteria are for uncoated reinforcing bars, OCP data were collected for every bar type employed in this study, as a measured potential indicating the possibility of corrosion can also be used to suggest a failure of the coating or protective covering of the steel.

After an electrical connection was made to an electrically isolated top mat bar through the data collection box, three OCP measurements along a transverse bar and five measurements along a longitudinal bar were taken, as illustrated in figure 30. The mean value of multiple potential readings was used as a nominal OCP of a particular bar at the time of measurement.

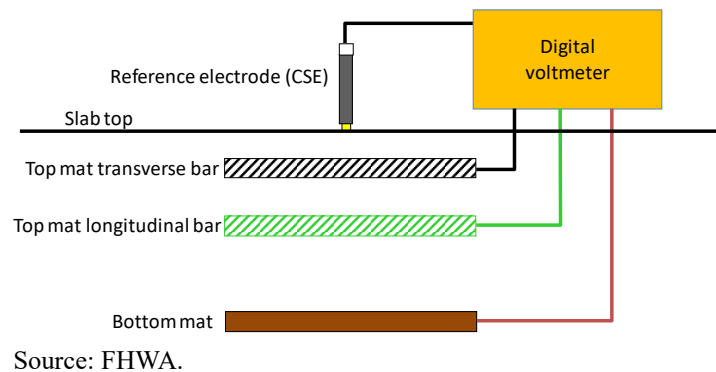


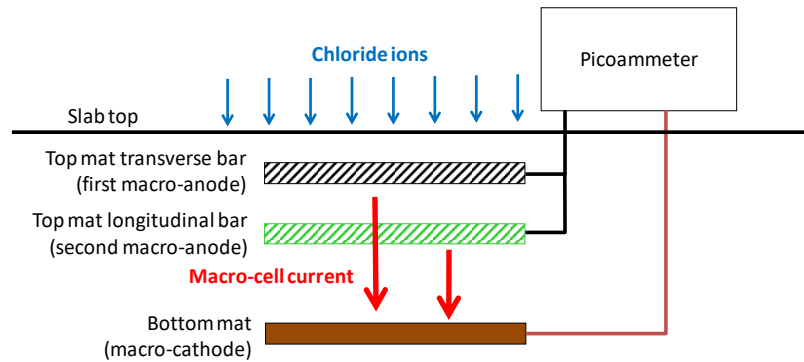
Figure 30. Illustration. OCP measurement.

Macro-cell Corrosion Current ($I_{macro-cell}$) and Polarized Potential

The magnitude of $I_{macro-cell}$ indicates the intensity of a galvanic corrosion, while the direction of the current indicates which mat is more active than the other. The OCP difference between two mats is the driving force for this type of corrosion. Concrete resistance between the mats also influences $I_{macro-cell}$ —the higher the concrete resistance, the lower the $I_{macro-cell}$.

In this study, $I_{macro-cell}$ was measured by inserting a picoammeter between the top and bottom mats, as shown in the data collection switch box connected all eight top mat bars together as a macro-anode. The present study employed either #5 or #6 bars and resulted in different mat surface areas. Since the magnitude of $I_{macro-cell}$ can change based on the surface area of the mat involved, macro-cell corrosion current density ($i_{macro-cell}$) for a particular slab section was

calculated by dividing the current by its top mat surface area. The $i_{macro-cell}$ values are used in this report for comparing corrosion performance among slabs having different surface areas. Figure 31 illustrates $I_{macro-cell}$ measurement.



Source: FHWA.

Figure 31. Illustration. $I_{macro-cell}$ measurement.

Polarization is a phenomenon of potential shift from an electrode's equilibrium potential when net current flows in or out of the electrode. In this study, polarization occurred at the top and bottom mats simultaneously from their OCPs as soon as $I_{macro-cell}$ started to flow between them. Magnitude and direction (positive or negative) of polarization can be influenced by many factors, including magnitude/direction of $I_{macro-cell}$ and concrete resistance (electrolyte). After a steady flow of $I_{macro-cell}$ is reached, polarization stops. In this state, top and bottom mats share the same potential, which is called polarized potential, mixed potential, or galvanic potential. The polarized potential of a slab section was measured by placing a portable CSE in the middle of the top surface when the macro-cell current reached a steady state.

Alternating Current (AC) Resistance (Impedance at 97 Hz)

Resistance influences corrosion activities by restricting the flow of corrosion current (I_{corr}) at the micro level (i.e., bar surface/concrete interface) as well as the macro level (i.e., between macro-anode and macro-cathode). Determination of resistance between the top and bottom mats has been a part of typical macro-cell corrosion experiments. In this study, a soil resistance meter, which supplied an AC at 97 Hz, was employed to measure concrete resistance between the top and bottom mats. For the coated bars, the AC resistance included additional impedance components coming from the coating layers. Figure 32 shows a diagram of an AC resistance measurement.

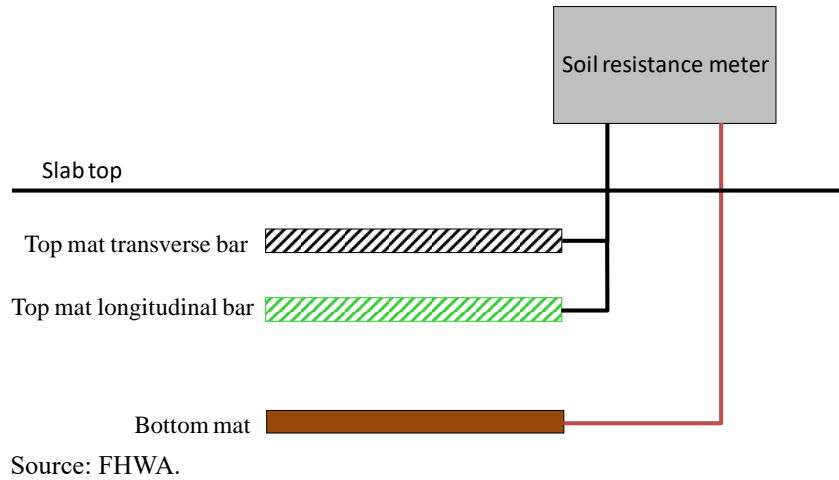


Figure 32. Illustration. AC resistance measurement.

Instantaneous Rate of Corrosion

A potentiostat was used to determine instantaneous rate of corrosion using the linear polarization resistance (LPR) method. The LPR tests were performed only at 410 and 526 d. Figure 33 and figure 34 show the LPR test setup and measurement.

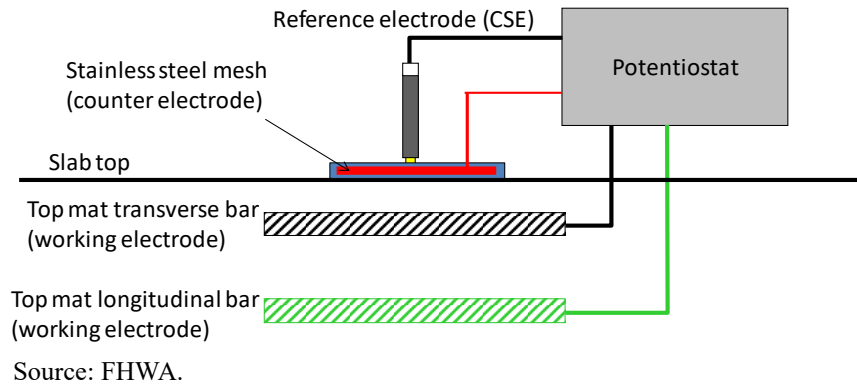
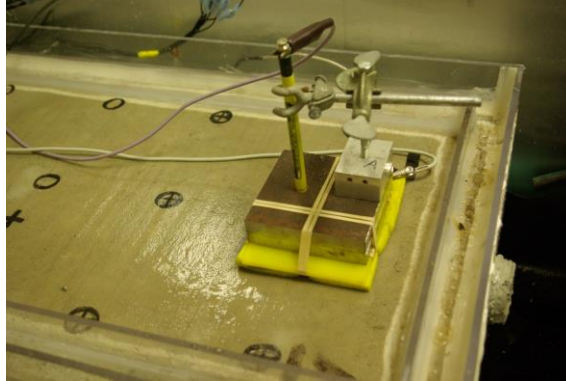


Figure 33. Illustration. LPR measurement.



Source: FHWA.

Figure 34. Photo. Corrosion rate measurement in progress.

This electrochemical technique applied a small direct current voltage from -0.015 V with respect to the specimen's OCP to $+0.015$ V at a scan rate of 0.0005 V/s and a sampling period of 2 s. The corresponding current data in response to each polarization step were recorded by the instrument, and the slope of the linear region between the potential data versus the corresponding current datasets was determined. By Ohm's law, this slope is called the polarization resistance (R_p). The experimentally determined R_p is used in the Stern-Geary equation to calculate I_{corr} or corrosion current density (i_{corr}) by dividing I_{corr} by electrode surface area. Faraday's law calculates mass loss at the time of measurement in terms of uniform penetration rate. This rate indicates the kinetic aspect of corrosion regarding how fast corrosion takes place at the moment of measurement. The most common corrosion rate units include mil per year and millimeters per year.

Some of the bar materials used in this study were alloys containing unknown elements; accurate equivalent weights of these alloys required for Faraday's law could not be determined. For this reason, this study uses a normalized R_p times surface area as another form of corrosion rate. A reciprocal of the normalized R_p is proportional to the commonly used uniform penetration rates.

Data Collection Procedure

The following procedure was adopted to collect experimental data in conjunction with weekly alternating exposure cycles:

1. Start a wetting cycle using a 15 weight percent NaCl solution on Monday morning.
2. Remove the NaCl solution in the ponding wells using a wet/dry vacuum on Thursday morning (beginning of the fourth day).
3. Measure polarized potential of the first slab section.
4. Insert a picoammeter between the top and bottom mats.
5. Break the electrical circuit between the mats.
6. Measure macro-cell current using the picoammeter.
7. Replace the picoammeter with a soil resistance meter and measure AC resistance between the mats.
8. Wait for approximately 2 h to let all electrically isolated top mat bars go back to their natural corrosion potentials via the depolarization process.
9. Measure OCPs of the top mat bars.
10. Restore the electrical connections.
11. Repeat steps 3 through 10 for the remaining slab sections.

Acid-Soluble (Total) Chloride Analysis

Three rounds of chloride analysis were performed: one after 102 d, one after 193 d, and the final one as part of the autopsy process. Acid-soluble chloride analysis was done per ASTM C1152.⁽¹⁸⁾ The first two chloride analyses investigated levels of chloride concentration associated with active OCPs, which were caused by a natural chloride diffusion process to some of the top mat bars or by NaCl solution leaking to the bottom mats over the slab's exterior surface. .

Figure 35 shows concrete powder sampling work near a top mat transverse bar. Final chloride analysis is discussed in the Autopsy of Test Slabs section.



Source: FHWA.

Figure 35. Photo. Chloride sampling at the top mat bar depth.

Unscheduled Interruptions

In the early stages of corrosion testing, NaCl solution leaked through some of the ponding wells and reached some bottom mats. Because every bottom mat had only a 0.5-inch clear cover, Cl⁻ reached the bottom mat bars much faster than the top mat bars, which had a 2-inch clear cover. Consequently, corrosion initiated prematurely on those affected bottom mats. After several attempts to repair the leaky ponding wells, it was concluded that all slabs needed a systematic and thorough repair to eliminate the possibility of reoccurrence. Figure 36 shows two slabs with dried NaCl deposits on the exterior surfaces and floor. When the exposure testing was suspended after 172 d, the slabs were cleaned with tap water followed by complete drying for several weeks. Next, slightly smaller ponding wells were installed inside the existing wells. Figure 26 shows the old and new ponding wells. Following repeated water tightness tests with tap water and some minor repairs, the exposure testing resumed after 284 d. The leaking problem caused nearly 4 mo of interruption and unintended corrosion of some bottom mats.



Source: FHWA.

Figure 36. Photo. Concrete slabs with leaking ponding wells.

In addition, corrosion-induced concrete cracks and liquid-type rust stains were observed on some slab sections. Thus, continuous drying was maintained from 417 to 473 d to investigate the effects of prolonged drying on already developed concrete cracks and other hidden damage being developed. The intention of the extended drying was to promote more corrosion damage by voluminous corrosion products.

AUTOPSY OF TEST SLABS

After the final dataset was collected, the slabs were taken out of heat tents, and the following autopsy work was performed in sequence.

Core Extraction

As the first step of the autopsy, a 4-inch-diameter core was taken at the transverse/longitudinal bar intersections such that 18 cores were extracted from a slab section: three cores from each of four straight transverse bars (core identification (ID) starts with 1, 2, 5, or 6) and six cores from a bent transverse bar (core ID starts with 3 or 4). Figure 37 shows a slab section showing traces of transverse and longitudinal bars prior to coring, and figure 38 shows coring work being performed. Most of the extracted cores contained a piece of a transverse bar and a piece of a longitudinal bar. After a total of 279 cores were taken out of 16 slab sections in 2011, they were stored in the FHWA Coatings and Corrosion Laboratory (see figure 39). In May 2014, they were transported to an independent laboratory for the remaining autopsy work.



Source: FHWA.

Figure 37. Photo. Concrete slab section ready for coring.



Source: FHWA.

Figure 38. Photo. Coring work in progress.



Source: FHWA.

Figure 39. Photo. Storage of extracted cores in the laboratory.

Photographic Documentation of Cores

Each core was documented using a digital camera. Any unique features observed were recorded in a core catalog sheet. Figure 40 shows a representative photograph of a core containing a transverse bar and a longitudinal bar. When a bottom of a core revealed a bar piece or other interesting feature, its condition was photographed, as shown in figure 41. A ruler was included in each figure to record overall length of the cores.



Source: FHWA.

Figure 40. Photo. Documentation of a core.



Source: FHWA.

Figure 41. Photo. Documentation of a core's bottom showing a severely corroded black bar.

Condition Evaluation of Extracted Bar Samples

When core documentation was completed, 192 cores containing straight transverse/longitudinal bars were chosen for bar extraction and final chloride analysis. The remaining cores containing bent bars were reserved in case more work needs to be done in the future. Only transverse bars were extracted for autopsy, as the longitudinal bars embedded in the deeper depth were not likely to reveal valuable information due to lower chloride concentration compared to the transverse bar depth. To separate the cores cleanly at the transverse bar level, two saw cuts were made into either side of the bar, and a chisel was used to exert the splitting force (see figure 42).



Source: FHWA.

Figure 42. Photo. Splitting a core at the transverse bar depth.

Once a core was opened up at the transverse bar depth, the upper and lower sections of the core were placed together in two depth-adjustable jigs, as shown in figure 43. This custom-made

setup allowed two fracture surfaces to be on the same level regardless of any height differences between two core sections. Any interesting features of bar imprints were photographed.



Source: FHWA.

Figure 43. Photo. Documentation of a bar/concrete interface after splitting.

After a transverse bar was extracted, the top side (i.e., facing the top surface) and underside (i.e., facing the concrete interior) of the bar were photographed. The observed corrosion morphology was captured with close-up photographs. A low-power magnifying glass and a digital microscope were used to examine corrosion morphologies and take digital macro-photographs. The examined bars were placed in a sealed plastic bag and stored for future reference.

For ECR and DCR samples, coating was peeled off, starting from as-received and artificial coating defects, until no more coating could be removed to determine the extent of coating disbondment. A knife adhesion test was also performed to determine the qualitative adhesion strength of intact coating at two spots on the top side and two more on the bottom side of a sample bar.

Final Chloride Analysis

In order to quantify corrosivity around the bar samples, concrete powder samples were taken at the bar depth to analyze acid-soluble chloride concentrations. Chloride diffusion coefficients of the selected cores were also determined using acid-soluble chloride concentrations of the powder samples taken at several depths from each of the selected cores.

Concrete Powder Sampling

After a transverse bar was removed, a concrete powder sample was taken from the upper bar imprint by gently shaving the bar trace with an oscillating saw (see figure 44). These samples were used to determine chloride concentration at a bar depth of 2 inches ($[Cl^-]_{interface@2-inch}$).



Source: FHWA.

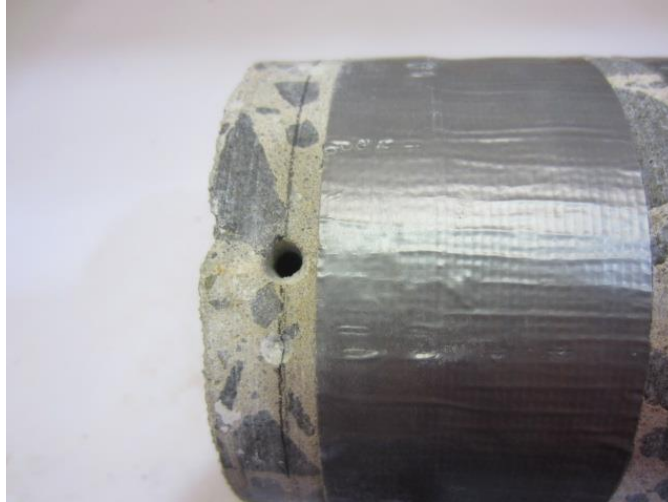
Figure 44. Photo. Concrete powder sampling from upper bar imprint of a core.

The cores taken from the 1-inch cover slab sections containing black bars were disintegrated during coring due to severe corrosion damage. Therefore, three cores from each slab section with a 2-inch clear cover were chosen for 5-depth chloride profiling and subsequent determination of chloride diffusion coefficients. Full-depth concrete powder samples were taken at 0.125, 0.5, 1, 2, and 4 inches. After the top 0.03125 inch was shaved off using a diamond blade masonry saw, the first chloride sample at 0.125 inch was prepared from a slice between depths of 0.03125 and 0.25 inch. Other samples at deeper depths were collected by drilling the core with a 0.1875-inch masonry drill bit. Figure 45 and figure 46 show core drilling and a sampled hole, respectively. The latter figure also shows a band of duct tape, which prevented cross-contamination with powder residues falling from already sampled holes. Drilling was performed from the deepest depth toward shallower depths to minimize the risk of cross-contamination.



Source: FHWA.

Figure 45. Photo. Concrete powder sampling by drilling.



Source: FHWA.

Figure 46. Photo. Close-up view of a sampling hole.

Acid-Soluble Chloride Analysis and Determination of Chloride Diffusion Coefficients

Like interim chloride analysis, the final acid-soluble chloride analysis was made according to ASTM C1152.⁽¹⁸⁾ A service life prediction model developed by the independent laboratory was used to determine the chloride diffusion coefficients of the cores with full-depth chloride data.

CHAPTER 3. TEST RESULTS AND DISCUSSION

PHYSICAL CONDITION OF TEST SLABS

When the accelerated corrosion testing was terminated, the slabs were generally in good condition. One exception was slab 1R, which had developed several concrete cracks and rust stains due to the 1-inch clear cover.

Figure 47-A shows a representative condition of the slab section exhibiting a corrosion-induced crack highlighted in a blue square after 165 d of testing (or 137 d of NaCl solution exposure).

Figure 47-B shows a close-up view of the cracked concrete. The condition of the slab worsened with more cracks and rust stains over time. The other black bar slab section with a 1-inch cover (slab 8R), which was added at a later time, also developed small rust stains after 70 d of salt water exposure.



Source: FHWA.

A. Cracked concrete.



Source: FHWA.

B. Close-up view of the crack.

Figure 47. Photos. Corrosion damage on slab 1R.

Slab 5, which contained HSR (left section) and SSR1 (right section), exhibited rust oozing out through the lateral face of the slab where top mat transverse bars entered. An example of this condition is shown in figure 48.



Source: FHWA.

Figure 48. Photo. Rust oozing out of a top mat transverse bar.

POTENTIAL AND $i_{macro-cell}$ DATA

Figure 49 through figure 80 show potentials and $i_{macro-cell}$ data plots of all slab sections. Each particular bar material is represented by a pair of figures, which show a potential versus time plot and an $i_{macro-cell}$ versus time plot. For example, figure 49 shows a potential versus time plot for black bars in a 1-inch cover slab section (slab 1R), and figure 50 shows an $i_{macro-cell}$ versus time plot for the same slab section. While all of the potential versus time plots can be made with the same potential range of 0 to $-0.7 V_{CSE}$, individual $i_{macro-cell}$ versus time plots were made with different current density scales due to a large variation in the data.

In each plot, the experiment suspended period (173 to 283 d) is indicated by a column, and the continuous drying period (417 to 473 d) is indicated by another column. With these columns, each plot is divided into the following five phases for the entire testing period:

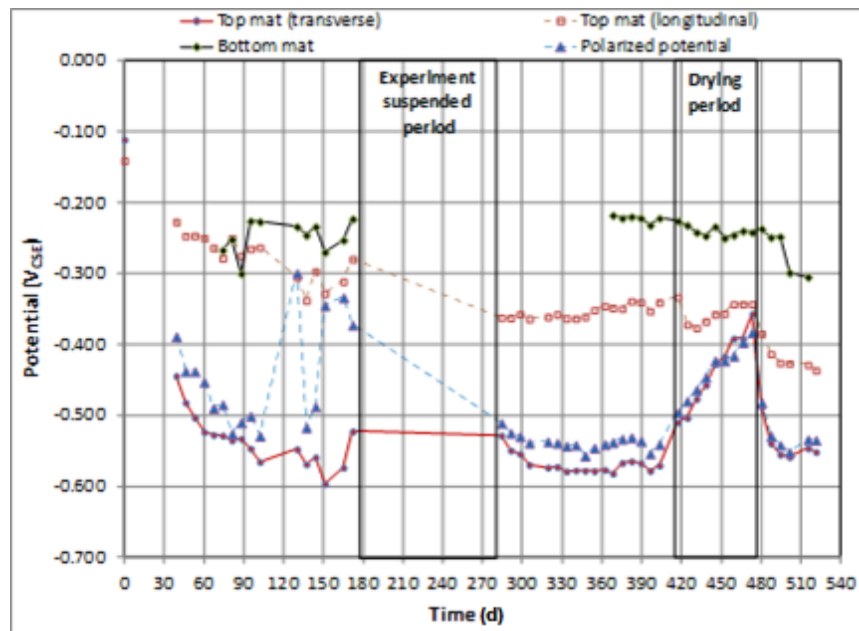
- **Baseline (0 d):** Baseline OCP data were collected using tap water as a wetting agent. (The slabs were 53 d old.)
- **Phase I (39 to 172 d):** There was an initial exposure to salt water. Sporadic leaking problems occurred, and some slabs exhibited reversed (negative) macro-cell current.
- **Phase II (284 to 403 d):** NaCl solution exposure testing was resumed. No more leaking occurred, and the second black bar slab (slab 8) was added.
- **Phase III (417 to 473 d):** Drying condition was maintained continuously at 100 °F.
- **Phase IV (480 to 521 d):** NaCl solution exposure testing continued.

Black Reinforcing Steel (Slabs 1 and 8)

The potential plots for two 1-inch-cover black bar slab sections (see figure 49 for slab 1R and figure 51 for slab 8R) behaved very similarly, even though slab 1R started much earlier than

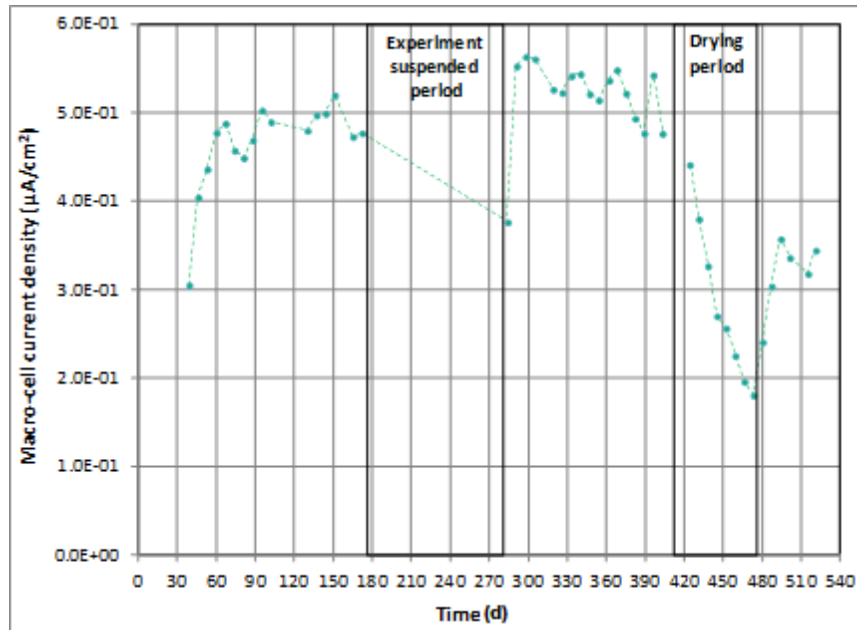
slab 8R. It took about 30 d for both slabs to change from a positive OCP to $-0.500 V_{CSE}$ and another 90 d to reach a very negative potential around $-0.600 V_{CSE}$. The $i_{macro-cell}$ behaviors of these slabs (see figure 50 for slab 1R and figure 52 for slab 8R) were also similar in that initially $i_{macro-cell}$ increased to a plateau of $0.5 \mu A/cm^2$ ($3.23 \mu A/inch^2$) within 100 d of testing and then decreased to about $0.2 \mu A/cm^2$ ($1.29 \mu A/inch^2$) during the extended drying in phase III. The shallow concrete cover was responsible for inducing active corrosion in terms of OCP and $i_{macro-cell}$ in a relatively short period. Two datasets showed similar corrosion initiation behaviors that were able to confirm the reproducibility and effectiveness of the accelerated corrosion testing method.

For black bars in the regular 2-inch slab section (slab 1L), salt water-initiated corrosion of the bottom mat at the very early stages of phase I occurred during the initial testing due to unexpected water leakage. This problem can be confirmed in figure 53, where OCP of the bottom mat became more negative (i.e., more active) than the top mat bars. Consequently, negative $i_{macro-cell}$ can be seen in figure 54. Also, a reduction of negative $i_{macro-cell}$ with time in phase I may suggest that top mat bars also initiated corrosion at some point, and thus the driving force gradually reduced between top and bottom mats. Subsequently, the top mat transverse bars exhibited quite active OCPs in phases II and III, which became similar to that of the bottom mat. The magnitude of $i_{macro-cell}$ also became less than that of phase I even though the negative current remained unchanged. The black bars embedded in the 2-inch cover (slab 8L) maintained passive OCP (see figure 55) and negligible $i_{macro-cell}$ (see figure 56) due to insufficient chloride concentration until the corrosion testing was terminated.



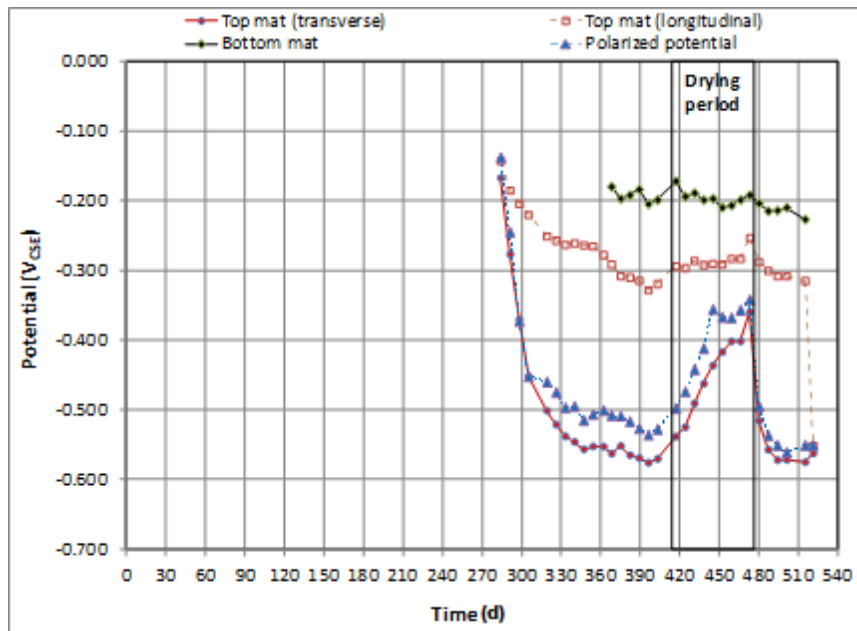
Source: FHWA.

Figure 49. Graph. Potential versus time plot for 1-inch black bars in slab 1R.



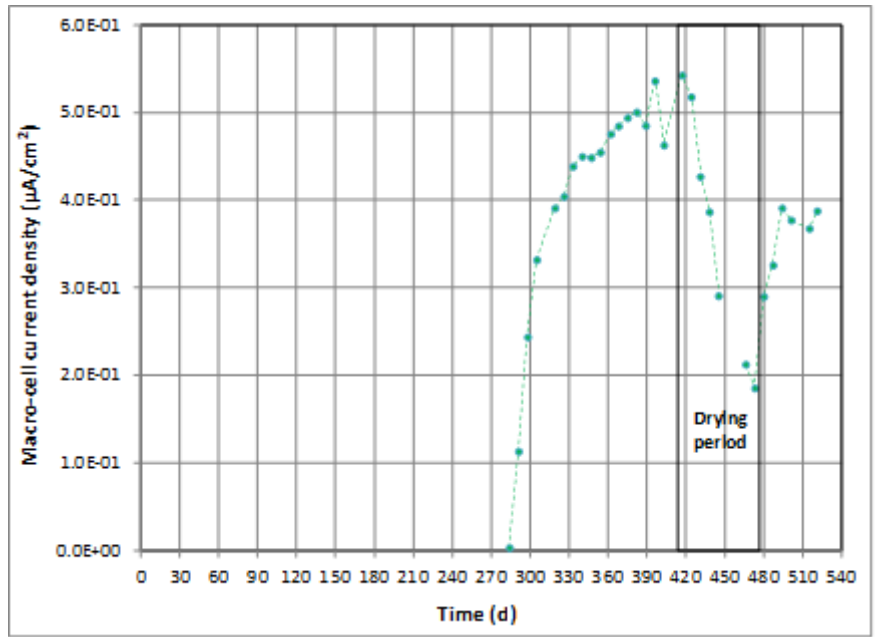
Source: FHWA.
 $1 \mu\text{A}/\text{cm}^2 = 6.45 \mu\text{A}/\text{inch}^2$.

Figure 50. Graph. $i_{macro-cell}$ versus time plot for 1-inch black bars in slab 1R.



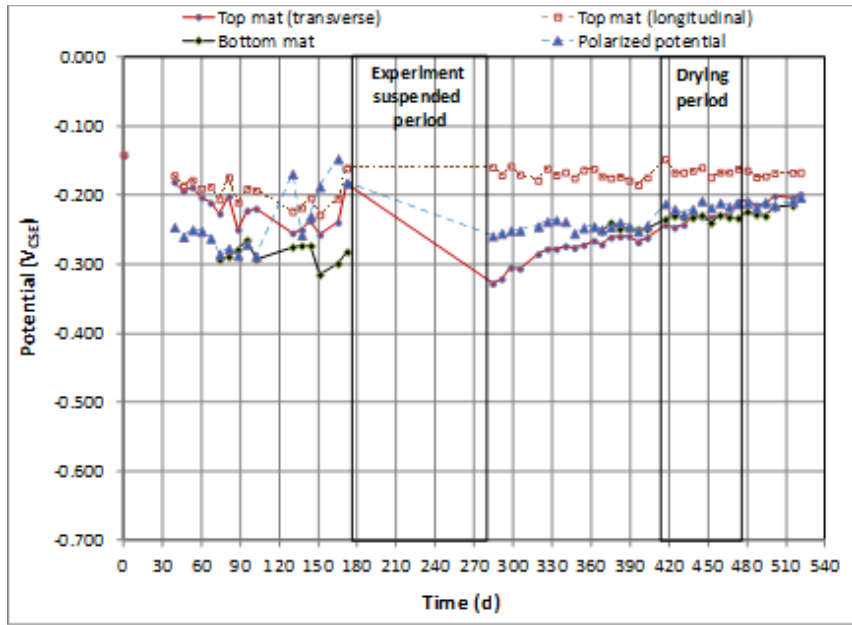
Source: FHWA.

Figure 51. Graph. Potential versus time plot for 1-inch black bars in slab 8R.



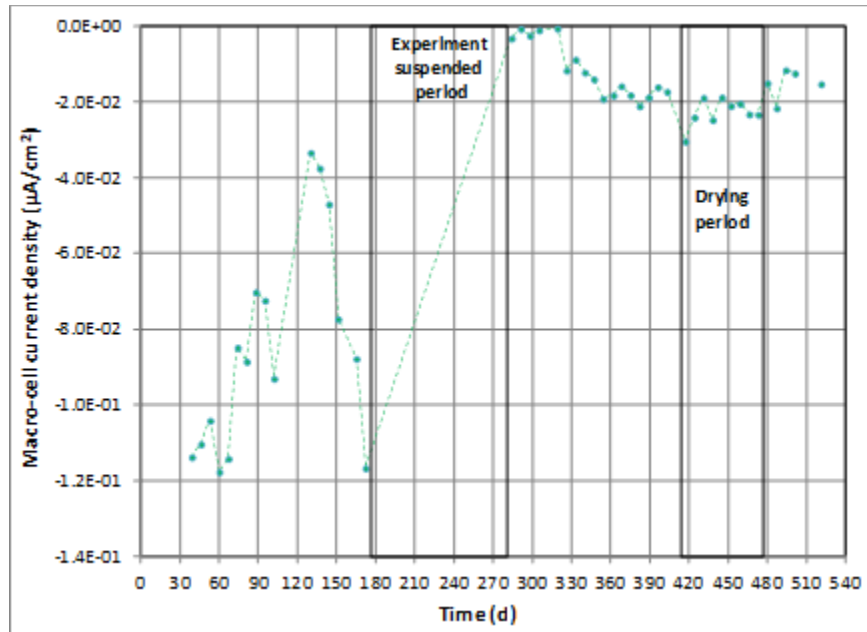
Source: FHWA.
 $1 \mu\text{A}/\text{cm}^2 = 6.45 \mu\text{A}/\text{inch}^2$.

Figure 52. Graph. $i_{macro-cell}$ versus time plot for 1-inch black bars in slab 8R.



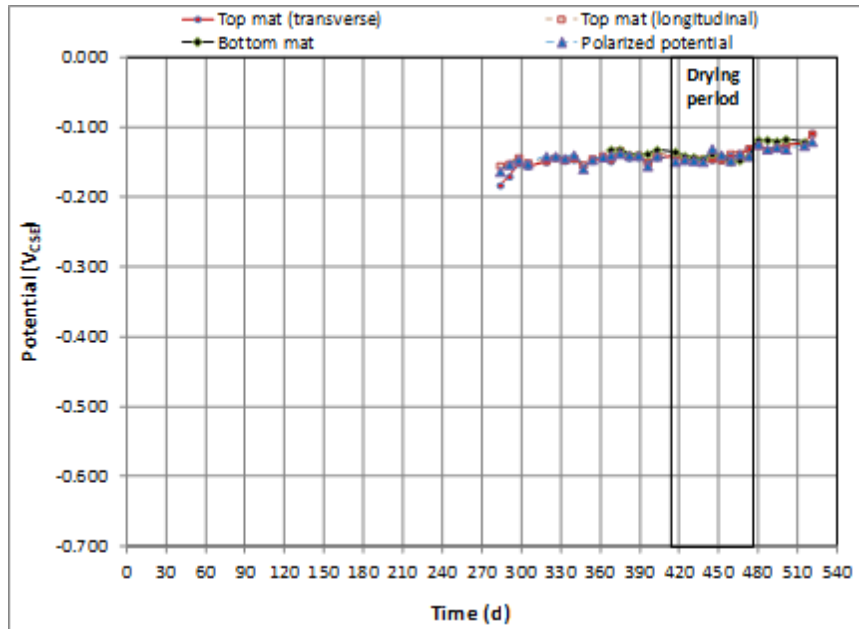
Source: FHWA.

Figure 53. Graph. Potential versus time plot for 2-inch black bars in slab 1L.



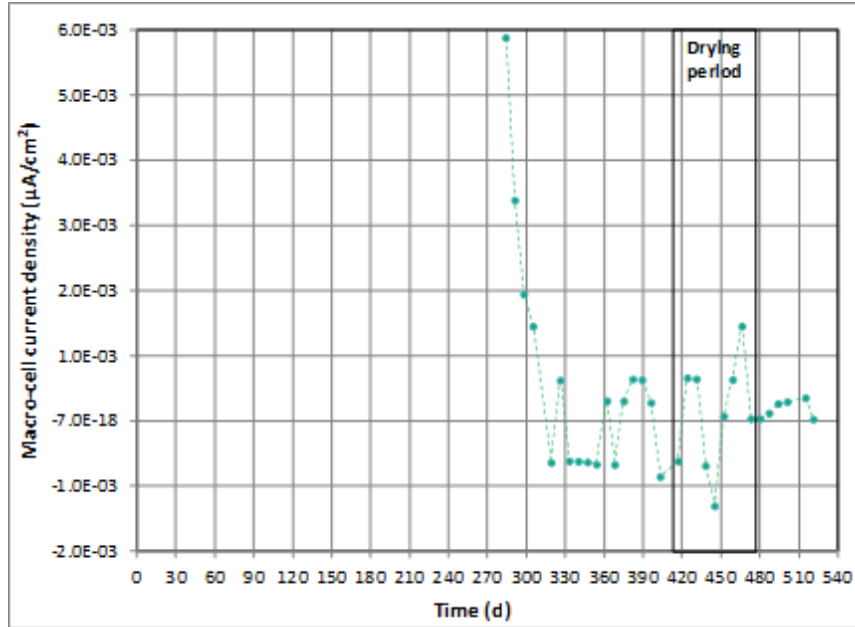
Source: FHWA.
 $1 \mu\text{A}/\text{cm}^2 = 6.45 \mu\text{A}/\text{inch}^2$.

Figure 54. Graph. $i_{macro-cell}$ versus time plot for 2-inch black bars in slab 1L.



Source: FHWA.

Figure 55. Graph. Potential versus time plot for 2-inch black bars in slab 8L.



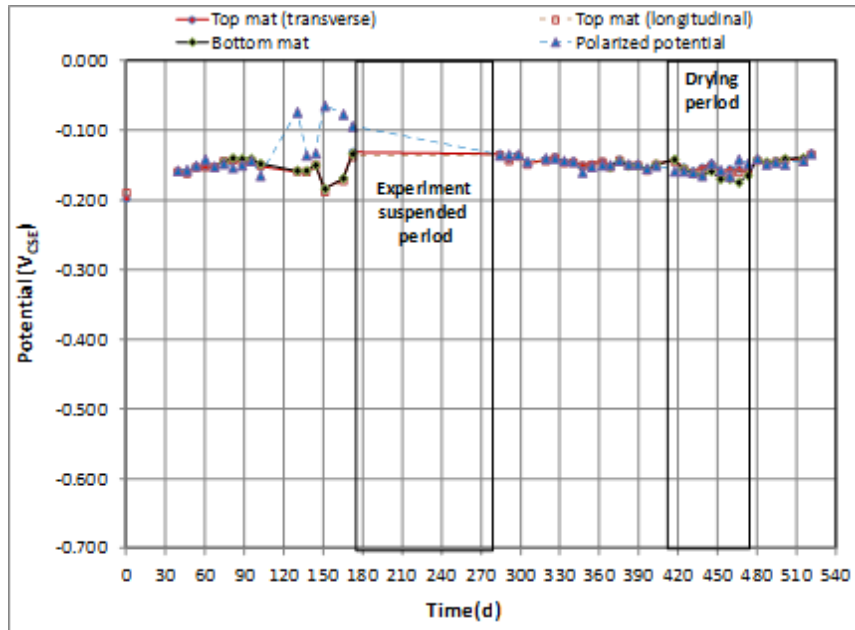
Source: FHWA.

$1 \mu\text{A}/\text{cm}^2 = 6.45 \mu\text{A}/\text{inch}^2$.

Figure 56. Graph. $i_{macro-cell}$ versus time plot for 2-inch black bars in slab 8L.

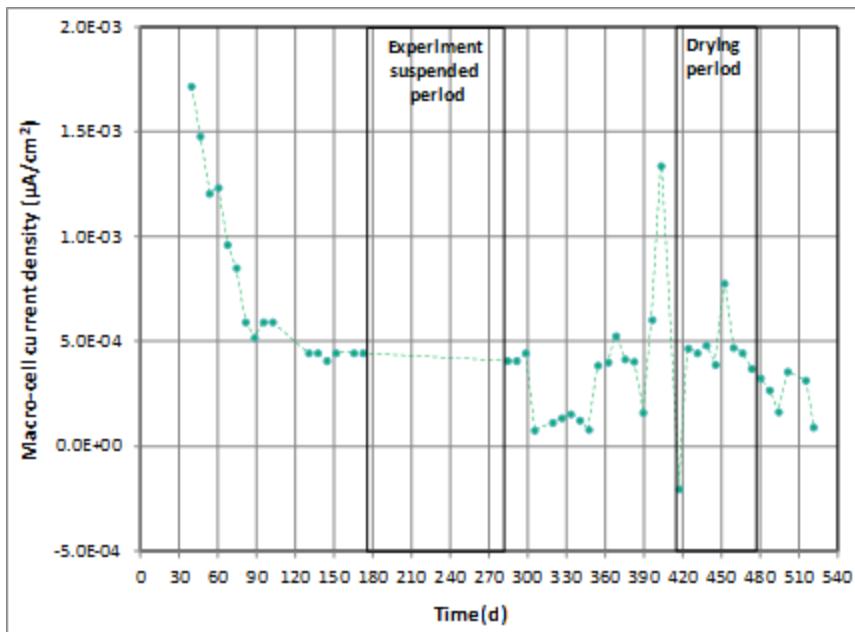
SCR1 (Slab 2L)

SCR1 demonstrated high corrosion resistance with consistently positive OCP and polarized potential (see figure 57) and negligible $i_{macro-cell}$ (see figure 58) throughout the testing. The corrosion-free bottom mat could be confirmed by consistently positive $i_{macro-cell}$ and positive bottom mat OCP data. The effect of extended drying was not observed in phase III.



Source: FHWA.

Figure 57. Graph. Potential versus time plot for SCR1 in slab 2L.



Source: FHWA.

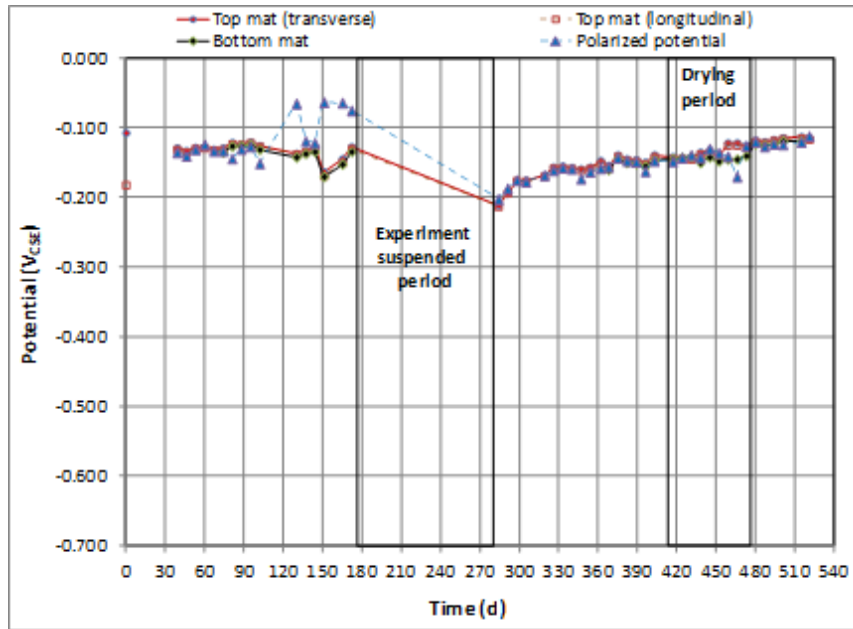
$1 \mu\text{A}/\text{cm}^2 = 6.45 \mu\text{A}/\text{inch}^2$.

Figure 58. Graph. $i_{macro-cell}$ versus time plot for SCR1 in slab 2L.

ECR Top Mat/Black Steel Bottom Mat (Slab 2R)

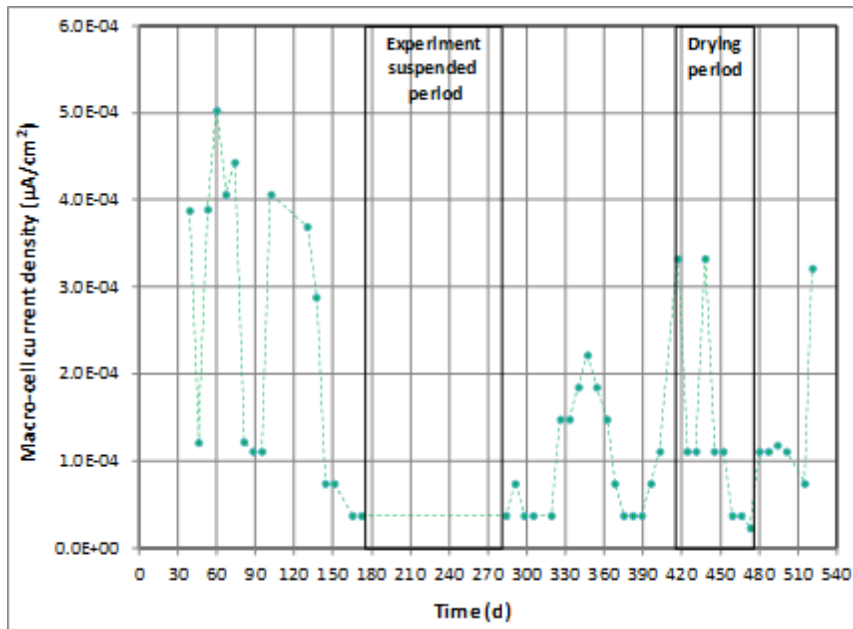
An assembly of ECR + black also demonstrated high corrosion resistance with consistently positive OCP and polarized potential (see figure 59) and negligible $i_{macro-cell}$ (see figure 60) throughout the testing. Like SCR1, corrosion-free bottom mat could be verified through

consistently positive $i_{macro-cell}$ and positive bottom mat OCP data. The effect of extended drying was not observed in phase III.



Source: FHWA.

Figure 59. Graph. Potential versus time plot for ECR + black in slab 2R.



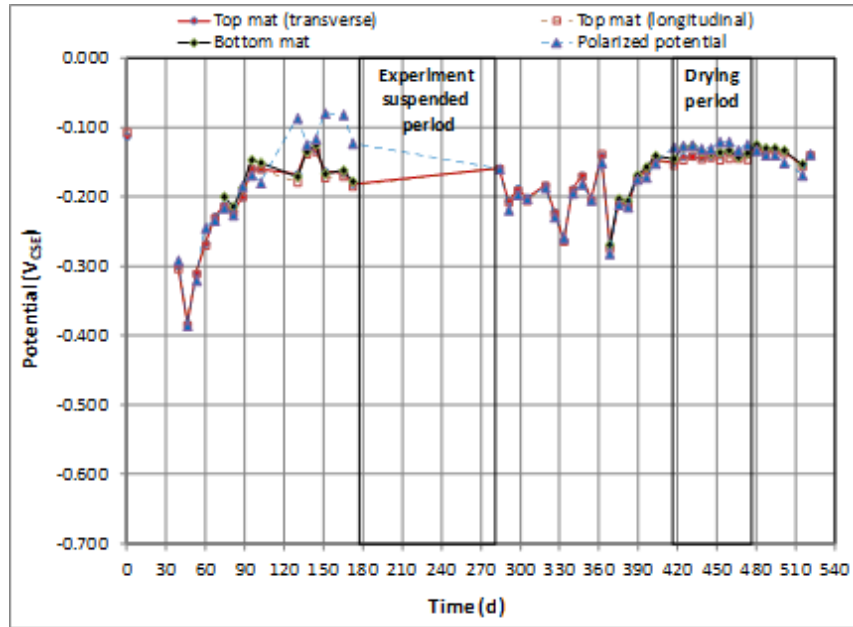
Source: FHWA.

$1 \mu A/cm^2 = 6.45 \mu A/inch^2$.

Figure 60. Graph. $i_{macro-cell}$ versus time plot for ECR + black in slab 2R.

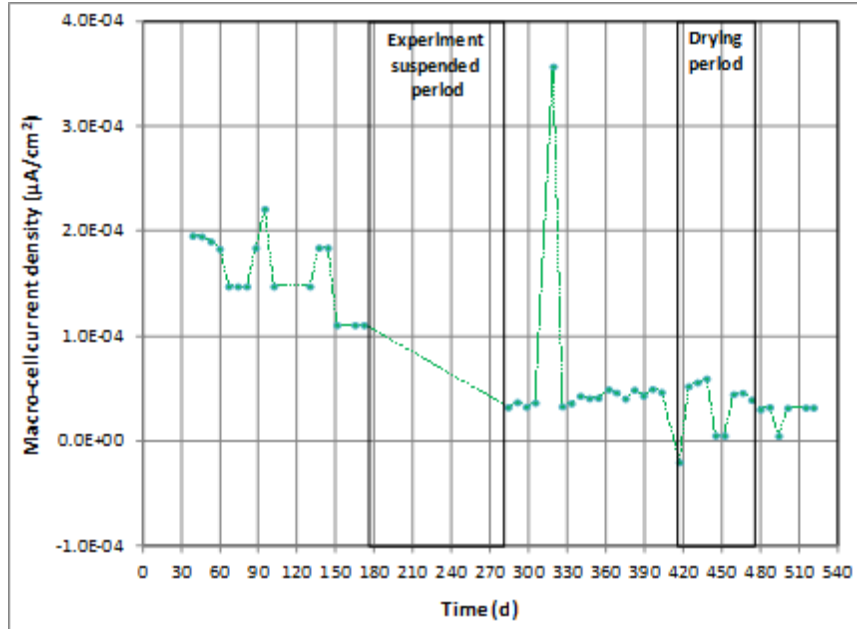
ECR in Both Mats (Slab 3L)

ECR in both mats started with somewhat negative OCPs and polarized potential and exhibited gradually more positive potentials with time (see figure 61). Negligible $i_{macro-cell}$ was maintained throughout the testing (see figure 62). No corrosion of the bottom mat could be confirmed by positive $i_{macro-cell}$ except for a single data point in phase III and a positive bottom mat OCP. The effect of extended drying was not observed in phase III.



Source: FHWA.

Figure 61. Graph. Potential versus time plot for ECR in slab 3L.



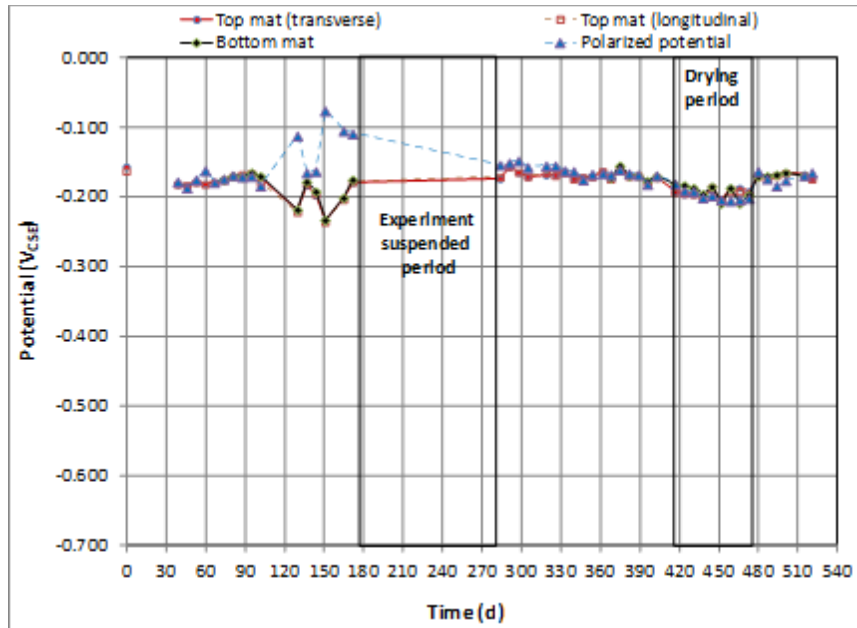
Source: FHWA.

$1 \mu\text{A}/\text{cm}^2 = 6.45 \mu\text{A}/\text{inch}^2$.

Figure 62. Graph. $i_{macro-cell}$ versus time plot for ECR in slab 3L.

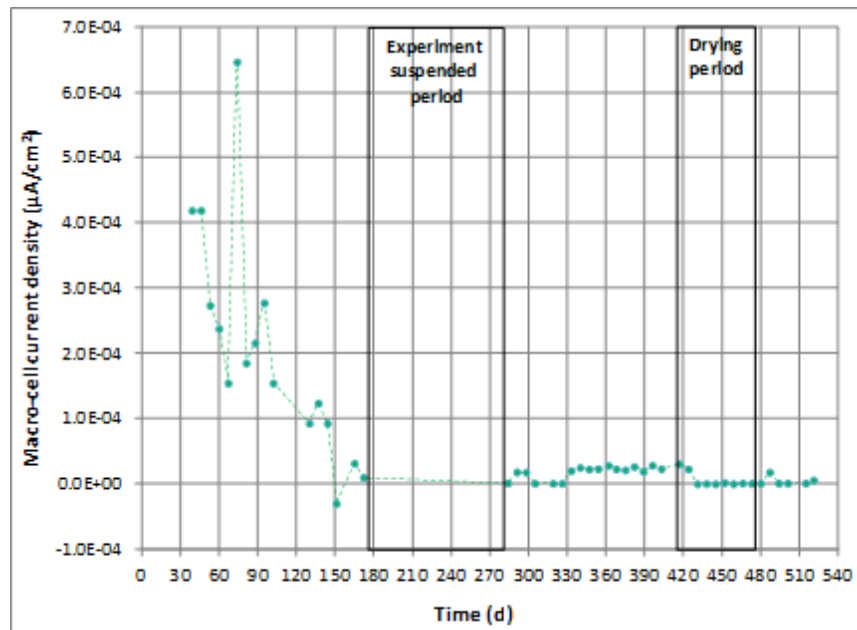
SCR2 (Slab 3R)

SCR2 behaved similarly to SCR1 and demonstrated high corrosion resistance with consistently positive OCPs and polarized potential (see figure 63) and negligible $i_{macro-cell}$ (see figure 64) throughout the testing. No bottom mat corrosion could be confirmed by positive $i_{macro-cell}$ except for a single data point in phase I and positive bottom mat OCP. Minor potential shifts in the negative direction were observed during the extended drying in phase III.



Source: FHWA.

Figure 63. Graph. Potential versus time plot for SCR2 in slab 3R.



Source: FHWA.

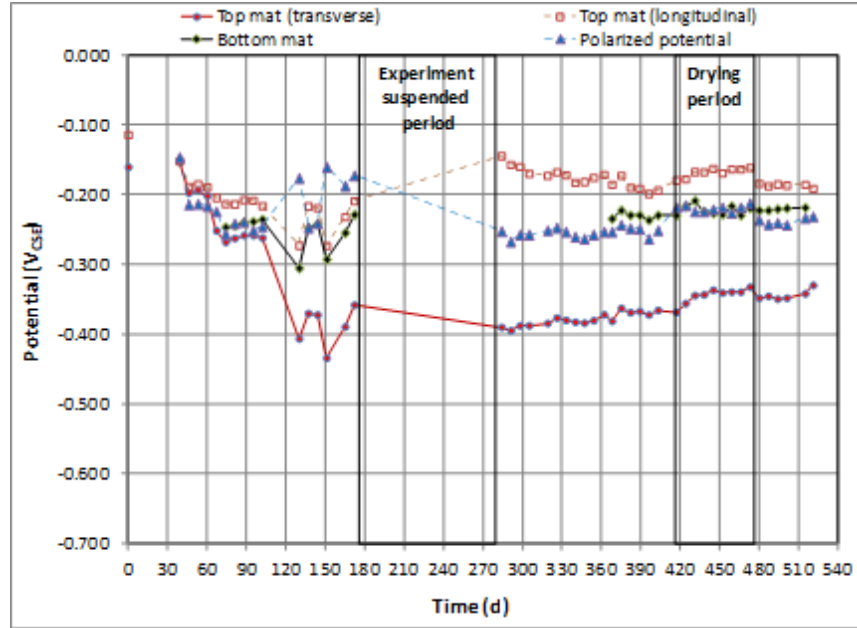
$$1 \mu\text{A}/\text{cm}^2 = 6.45 \mu\text{A}/\text{inch}^2.$$

Figure 64. Graph. $i_{macro-cell}$ versus time plot for SCR2 in slab 3R.

LSS2 (Slab 4L)

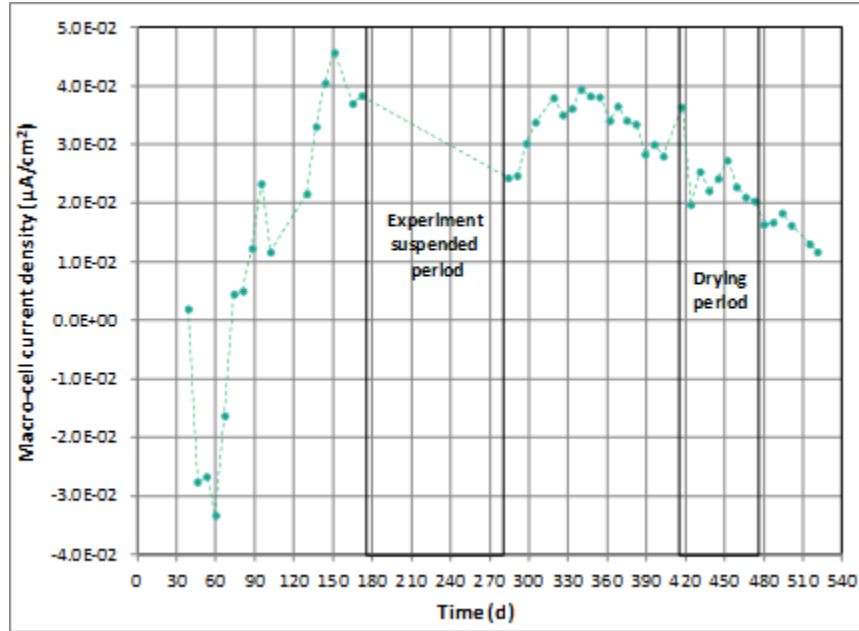
Top transverse bars became active near $-0.400 V_{CSE}$ after 120 d followed by a gradual shift in the positive direction in phases II through IV (see figure 65). However, top longitudinal bars and

bottom mat remained more positive than $-0.250 V_{CSE}$ for most of the time. The corresponding $i_{macro-cell}$ plot shows that negative $i_{macro-cell}$ occurred initially in phase I. After maximum $i_{macro-cell}$ was reached in phase II, it decreased continuously for the remaining period (see figure 66). Even though the exact reason is not known for the gradual OCP change of the top transverse bars in the positive direction, such an OCP behavior must have been responsible for the decreasing $i_{macro-cell}$. No drying effect on the potentials and $i_{macro-cell}$ was apparent.



Source: FHWA.

Figure 65. Graph. Potential versus time plot for LSS2 in slab 4L.



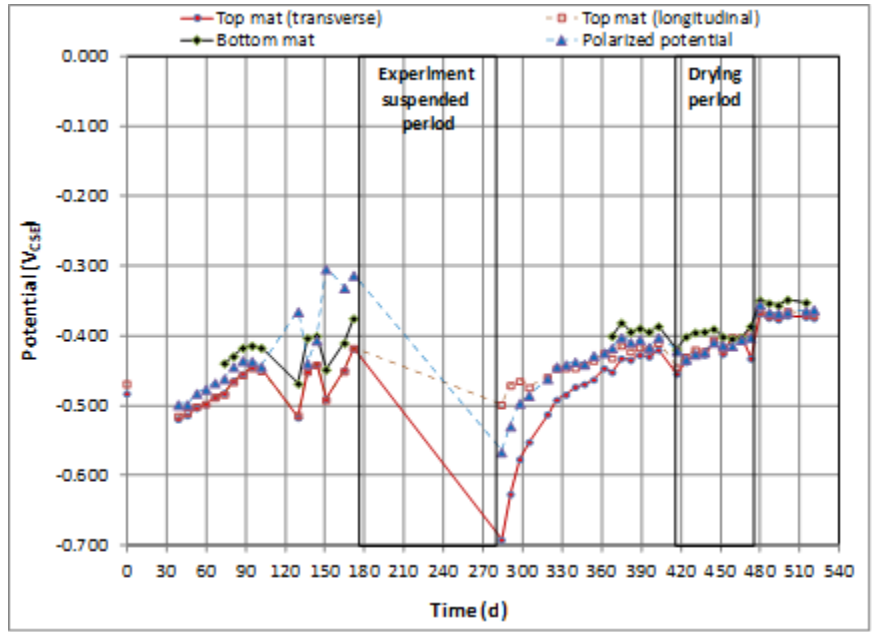
Source: FHWA.

$1 \mu\text{A}/\text{cm}^2 = 6.45 \mu\text{A}/\text{inch}^2$.

Figure 66. Graph. $i_{macro-cell}$ versus time plot for LSS2 in slab 4L.

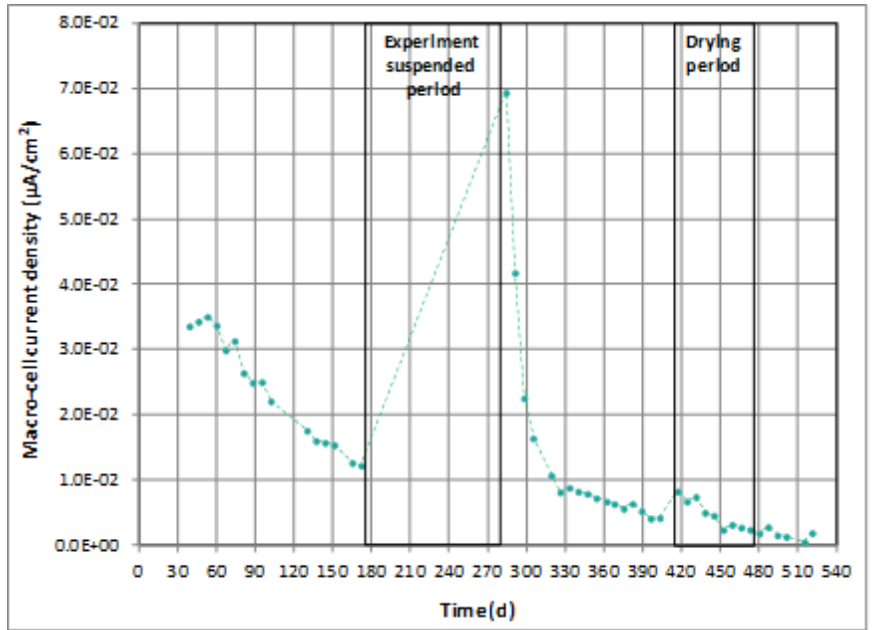
HDG (Slab 4R)

Because of the active zinc layer, HDG exhibited very active baseline OCPs near $-0.500 V_{CSE}$, and all potentials became more positive with time in phase I (see figure 67). When the top mat was exposed to salt water again in phase II, the OCP of the top transverse bars started at about 0.200 V less than its baseline. The top longitudinal bars exhibited the same initial baseline OCP. The top mat bars exhibited more positive OCPs and polarized potential with time in phases II through IV. As expected, the highest $i_{macro-cell}$ values were observed in phases I and II (see figure 68) when OCPs were the most negative. After the current surges, a decrease in $i_{macro-cell}$ was observed as OCPs became more positive with time in both phases. Interestingly, a potential shift of $-0.500 V$ and an increase in $i_{macro-cell}$ were noticed again in phase III soon after the concrete slab started drying. These potential and $i_{macro-cell}$ trends indicate that HDG was getting passivated with time under steady macro-cell current flow, but it could be reactivated in no current and/or drying conditions.



Source: FHWA.

Figure 67. Graph. Potential versus time plot for HDG in slab 4R.



Source: FHWA.

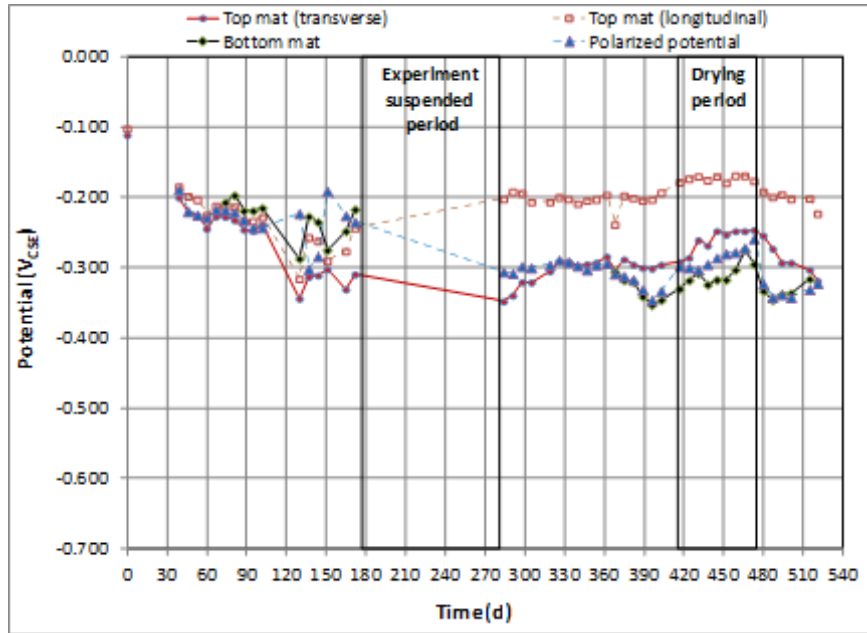
$$1 \mu\text{A}/\text{cm}^2 = 6.45 \mu\text{A}/\text{inch}^2.$$

Figure 68. Graph. $i_{macro-cell}$ versus time plot for HDG in slab 4R.

HSR (Slab 5L)

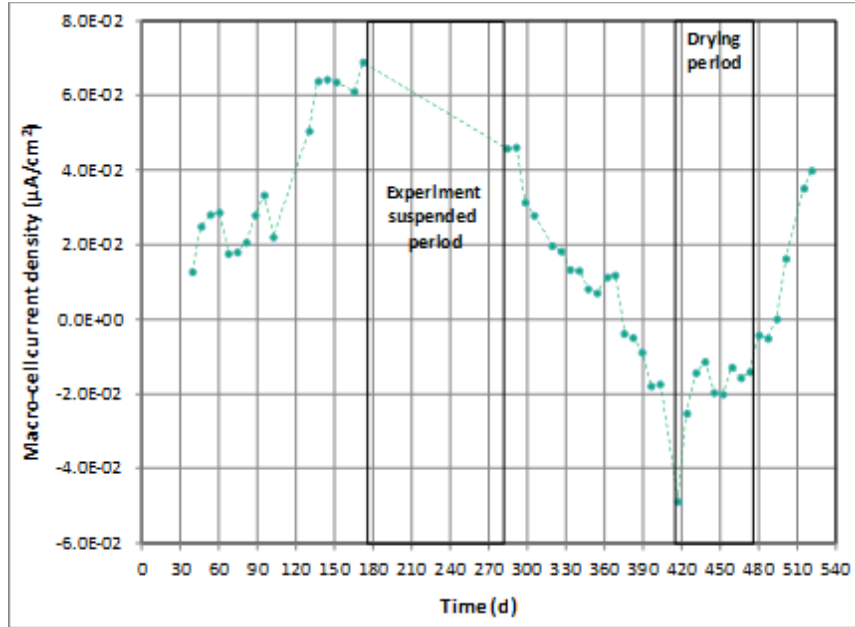
HSR exhibited very positive baseline OCPs followed by steadily decreasing potentials (see figure 69) and increasing $i_{macro-cell}$ (see figure 70) in phase I. While top longitudinal bars remained passive at around $-0.200 V_{CSE}$ in phases II through IV, top transverse bars stayed near

-0.300 V_{CSE} in phases II and IV. The bottom mat became more active than the top transverse bars near the end of phase II due to a corroding bottom mat as a result of leaked salt water. Subsequently, the polarized potential also became more negative than that of the top transverse bars. As a result, reversed macro-cell current flow took place during phase II. All potentials became more positive in phase III upon extended drying. Another current reversal occurred in phase IV as the OCP of the top transverse bars moved in the negative direction again, and the OCP of the bottom mat moved in the positive direction. Subsequently, a steady increase of *i*_{macro-cell} could be seen in phase IV.



Source: FHWA.

Figure 69. Graph. Potential versus time plot for HSR in slab 5L.

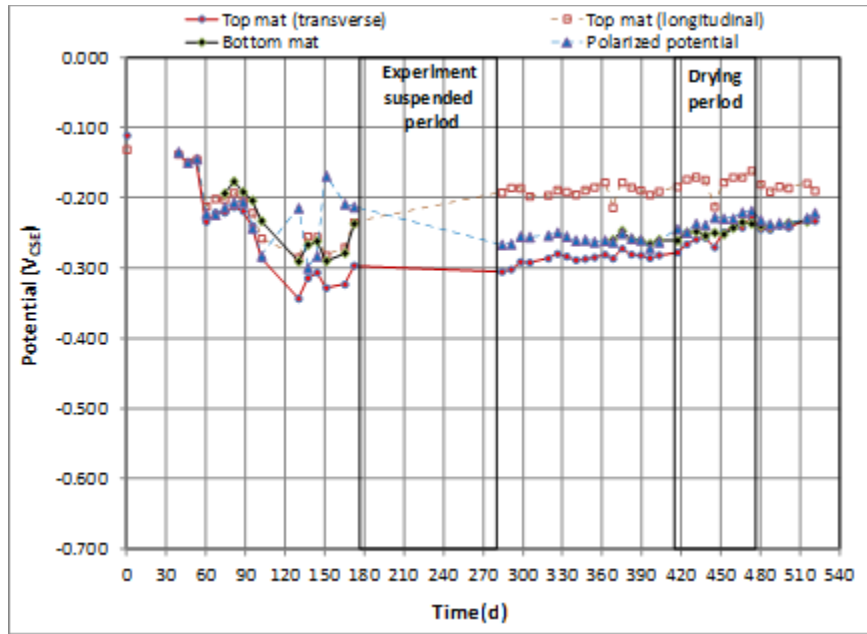


Source: FHWA.
 $1 \mu A/cm^2 = 6.45 \mu A/inch^2$.

Figure 70. Graph. $i_{macro-cell}$ versus time plot for HSR in slab 5L.

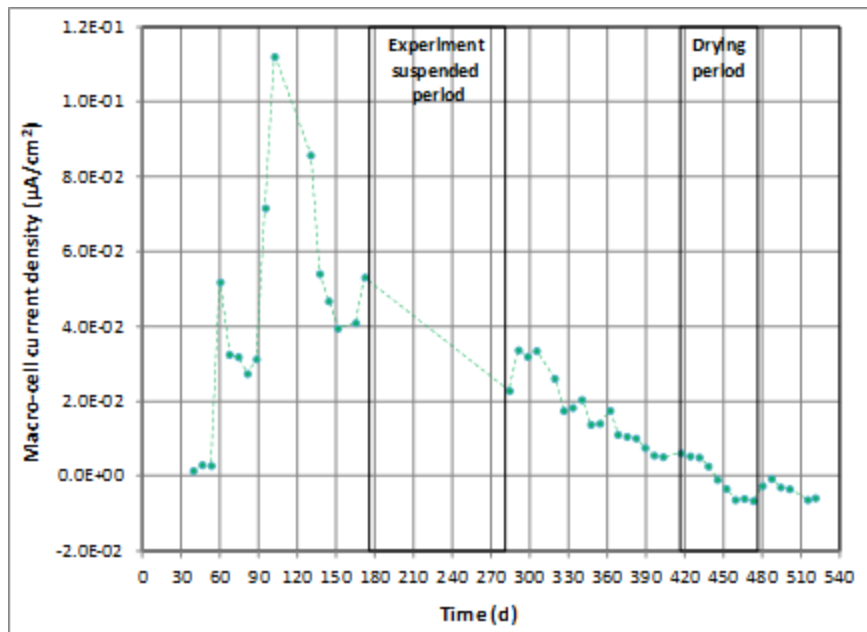
SSR1 (Slab 5R)

SSR1 also exhibited very positive baseline OCPs. In phase I, SSR1 showed steadily decreasing potentials (see figure 71) and increasing $i_{macro-cell}$ (see figure 72) before reversing their trends. While the top longitudinal bars remained passive near $-0.200 V_{CSE}$ throughout the remaining duration, the top transverse bars and bottom mat exhibited gradually positive OCPs and steadily decreasing $i_{macro-cell}$ for the same period. As a result, macro-cell current became negative for the last 80 d of testing. The magnitude of $i_{macro-cell}$ was considered larger than that of other bars, including ECR, DCR, and SSR2.



Source: FHWA.

Figure 71. Graph. Potential versus time plot for SSR1 in slab 5R.



Source: FHWA.

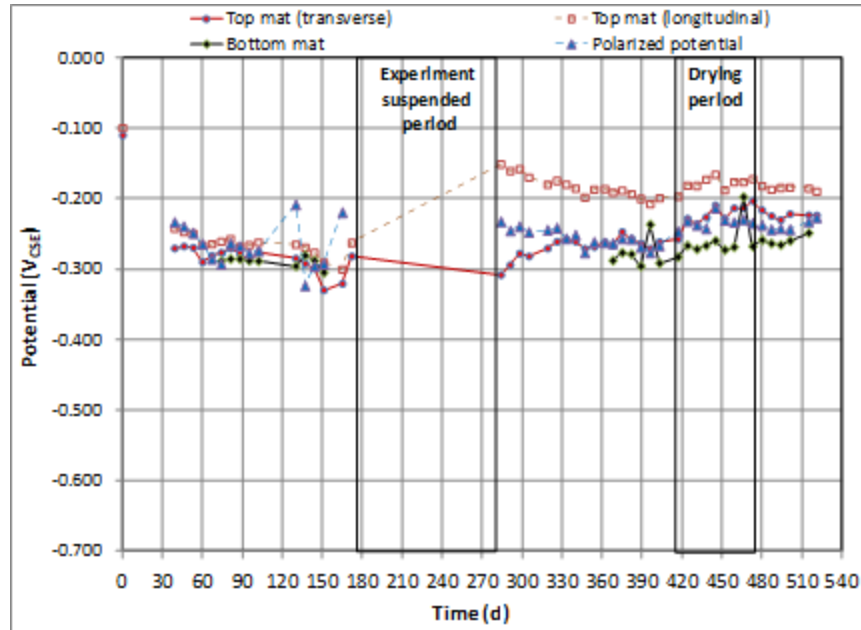
$$1 \mu\text{A}/\text{cm}^2 = 6.45 \mu\text{A}/\text{inch}^2.$$

Figure 72. Graph. $i_{macro-cell}$ versus time plot for SSR1 in slab 5R.

LSS1 (Slab 6L)

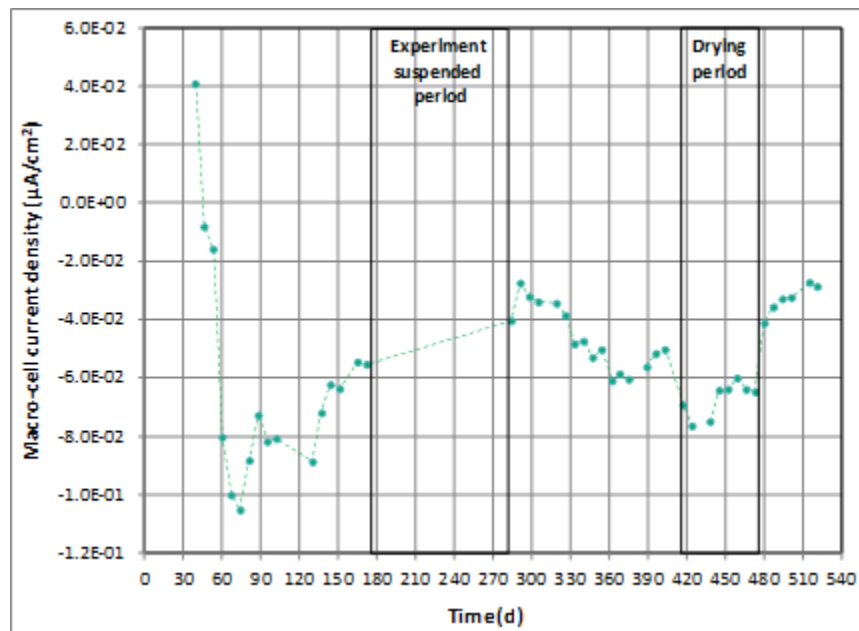
LSS1 also exhibited very positive baseline OCPs followed by gradual decreasing potentials (see figure 73) and $i_{macro-cell}$ (see figure 74) in phase I. A current reversal occurred during this period.

While the top longitudinal bars remained passive with above $-0.200 V_{CSE}$ throughout the remaining duration, the top transverse bars exhibited positive OCPs gradually from $-0.300 V_{CSE}$ with time for the same period. Due to corrosion of the bottom mat, the OCP of the bottom mat was more negative than that of the top transverse bars, leading to a negative $i_{macro-cell}$.



Source: FHWA.

Figure 73. Graph. Potential versus time plot for LSS1 in slab 6L.



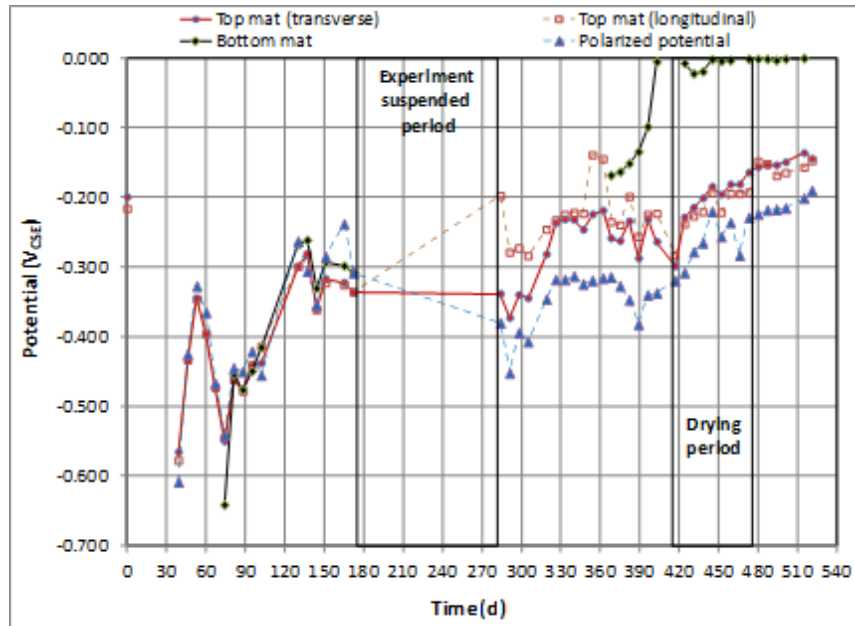
Source: FHWA.

$$1 \mu A/cm^2 = 6.45 \mu A/inch^2$$

Figure 74. Graph. $i_{macro-cell}$ versus time plot for LSS1 in slab 6L.

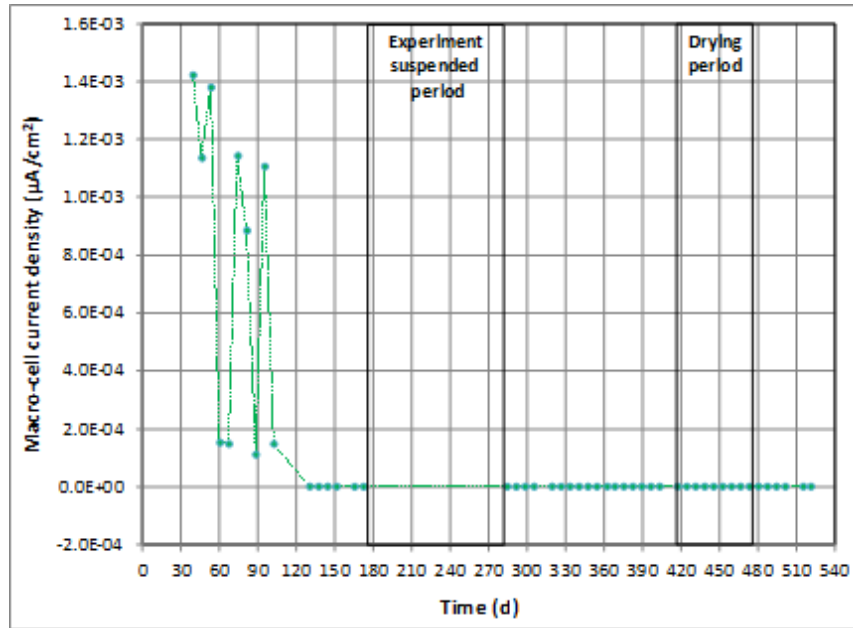
DCR (Slab 6R)

DCR exhibited very positive baseline OCPs. After an initial sudden potential drop in phase I, it exhibited a continuous upward movement of the potentials (see figure 75) and negligible $i_{macro-cell}$ (see figure 76) in phase II. All potentials became more positive with time, but $i_{macro-cell}$ remained virtually zero throughout the remaining duration. The passivity of zinc appeared to create similar potential and $i_{macro-cell}$ behaviors between DCR and HDG. In addition, no effect of extended drying was observed.



Source: FHWA.

Figure 75. Graph. Potential versus time plot for DCR in slab 6R.



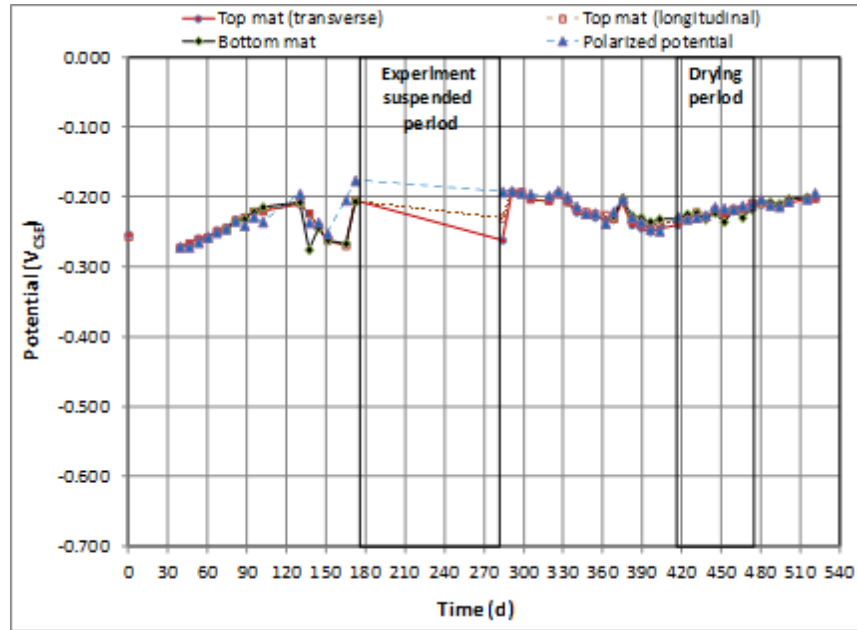
Source: FHWA.

$1 \mu\text{A}/\text{cm}^2 = 6.45 \mu\text{A}/\text{inch}^2$.

Figure 76. Graph. $i_{macro-cell}$ versus time plot for DCR in slab 6R.

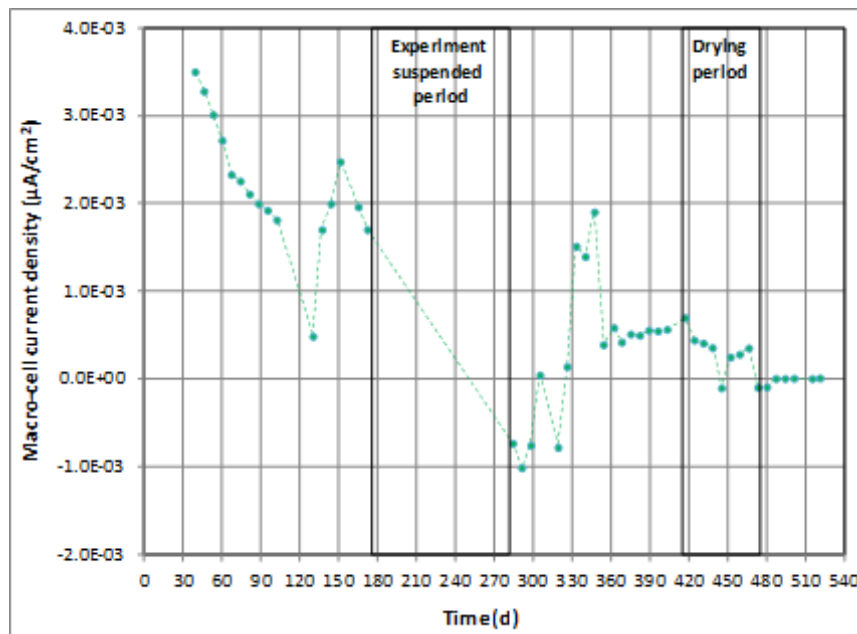
SSR2 (Slab 7L)

SSR2 exhibited $-0.250 V_{CSE}$ baseline OCPs. It maintained all potentials between -0.280 and $-0.200 V_{CSE}$ (see figure 77) and negligible $i_{macro-cell}$ (see figure 78) throughout the testing. There were several data points showing negative $i_{macro-cell}$ in the beginning of phase II, and it became almost $0 V_{CSE}$ in phase IV.



Source: FHWA.

Figure 77. Graph. Potential versus time plot for SSR2 in slab 7L.



Source: FHWA.

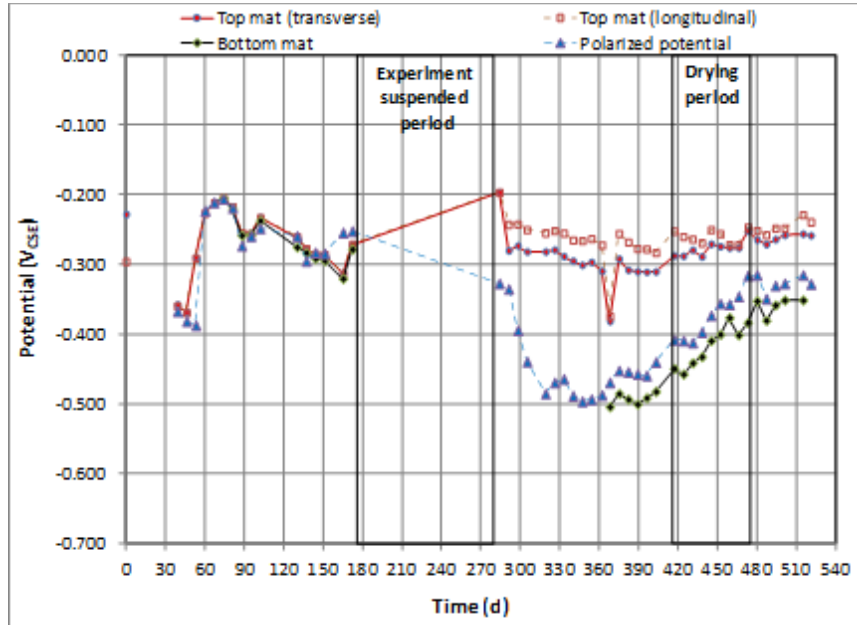
$$1 \mu\text{A}/\text{cm}^2 = 6.45 \mu\text{A}/\text{inch}^2.$$

Figure 78. Graph. $i_{macro-cell}$ versus time plot for SSR2 in slab 7L.

SSR3 (Slab 7R)

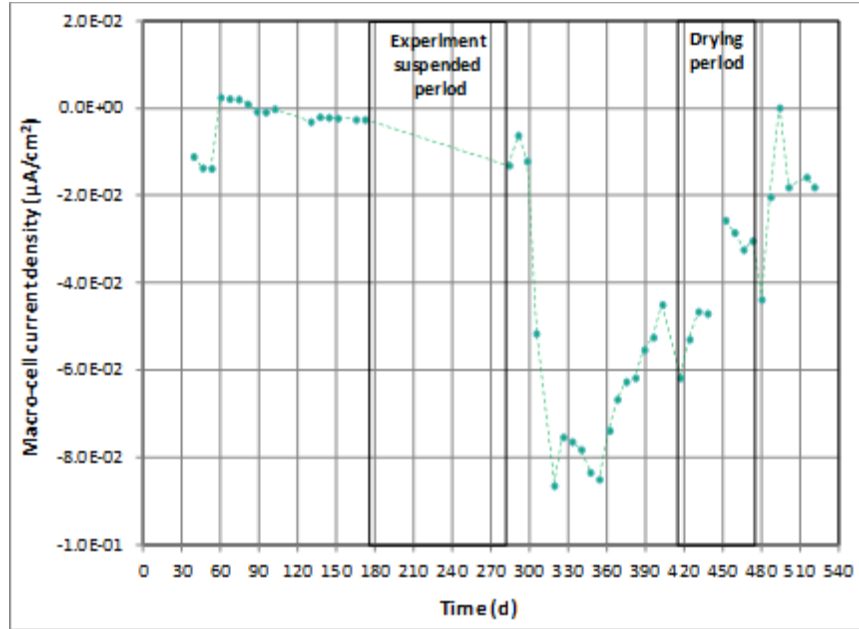
SSR3 exhibited relatively negative baseline OCPs followed by fluctuating potentials (see figure 79) and negligible $i_{macro-cell}$ (see figure 80) in phase I. From phase II, top transverse and longitudinal bars maintained more positive OCPs than $-0.300 V_{CSE}$, with some exceptional data

points throughout the testing. Conversely, the polarized potential and bottom mat OCP were quite negative before becoming more positive with time. These negative potentials were caused by the corroding bottom mat. As a result, negative $i_{macro-cell}$ was observed during the same period. The magnitude of $i_{macro-cell}$ was considered larger than that of other bars, including ECR, DCR, and SSR2.



Source: FHWA.

Figure 79. Graph. Potential versus time plot for SSR3 in slab 7R.

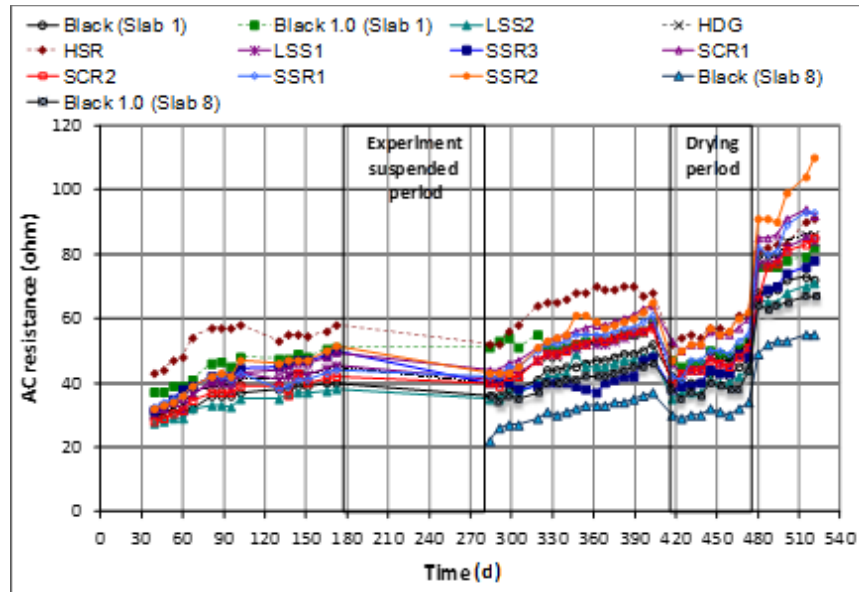


Source: FHWA.
 $1 \mu\text{A}/\text{cm}^2 = 6.45 \mu\text{A}/\text{inch}^2$.

Figure 80. Graph. $i_{macro-cell}$ versus time plot for SSR3 in slab 7R.

AC RESISTANCE

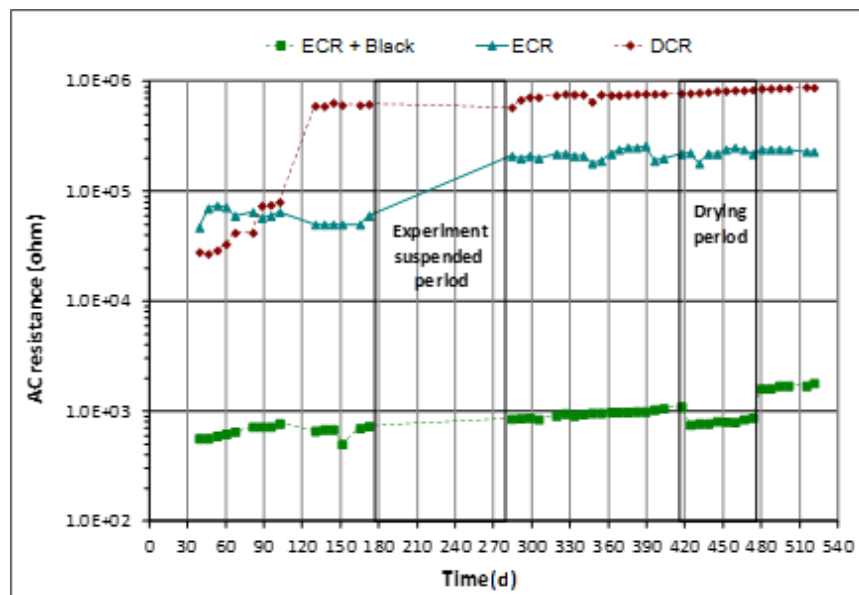
Figure 81 shows an AC resistance versus time plot for the bare bars. A gradual increase in AC resistance with time was observed for every bar material. Continuous hydration of cement paste was thought to be responsible for the increased resistance. This behavior might have also been responsible for the reduction in $i_{macro-cell}$ with time as discussed in the previous section. Except for the 2-inch cover black bars in slab 8L and HSR in slab 5L, the other bars were clustered around each other and varied within a 20-Ω range. All resistance dropped in phase III despite the extended drying exposure condition. This trend is not well understood, as drier concrete around the bars should have increased the AC resistance.



Source: FHWA.

Figure 81. Graph. AC resistance versus time plot for bare bars.

Figure 82 shows a similar plot for the coated bars (i.e., ECR, ECR with black bars in the bottom mat, and DCR). The presence of coating offered much higher AC resistance compared to the bare bars. The highest AC resistance was obtained by DCR, which had a dual coating system. The second-highest AC resistance was retained by ECR in both mats. ECR in the top mat and black bar in the bottom mat exhibited AC resistance at least two orders of magnitude lower than the other coated bars, but it still possessed resistance two orders of magnitude higher than the bare bars. The effect of extended drying on AC resistance of the coated bars was not significant.

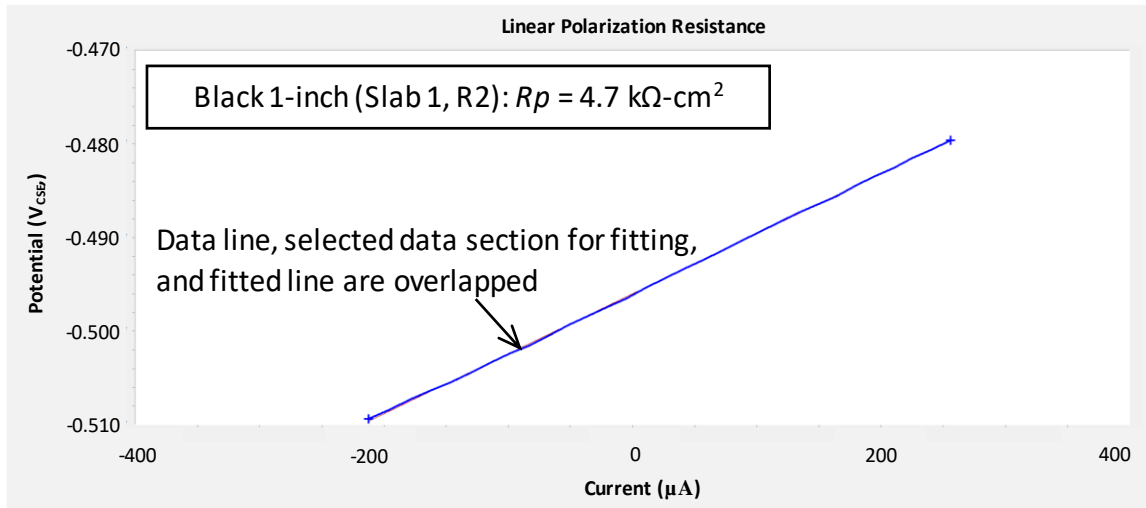


Source: FHWA.

Figure 82. Graph. AC resistance versus time plot for coated bars.

INSTANTANEOUS RATE OF CORROSION

Figure 83 presents typical low R_p (high corrosion rate) experimental data and linear regression analysis results indicated by a red fit line which is virtually identical to the data line. Similar examples for intermediate R_p (intermediate corrosion rate) and high R_p (low corrosion rate) are shown in figure 84 and figure 85, respectively. It can be seen that linearity of the experimental data tends to improve when R_p becomes lower.

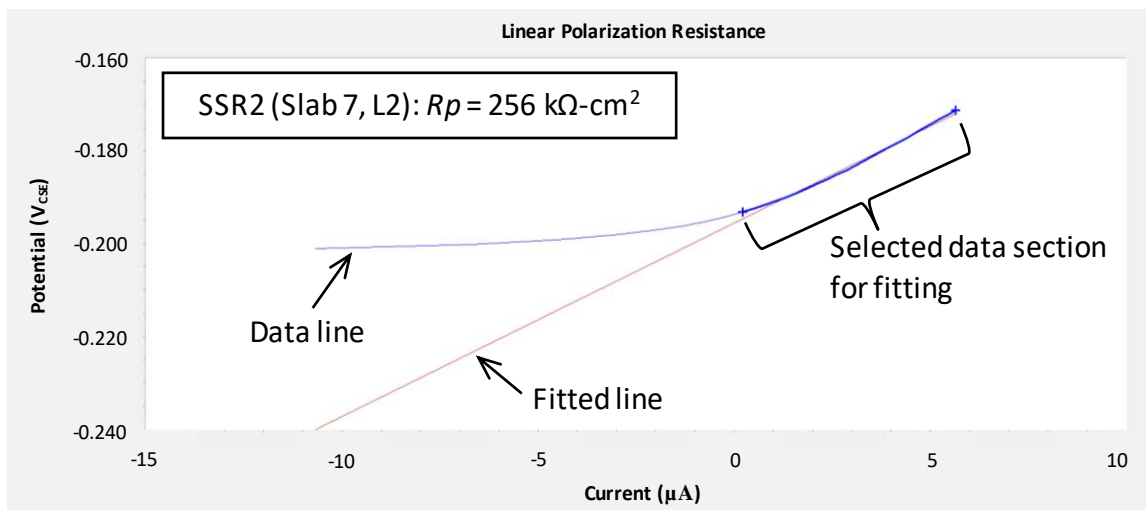


Source: FHWA.

$1 \text{ k}\Omega\text{-cm}^2 = 0.155 \text{ k}\Omega\text{-inch}^2$.

$1 \mu\text{A}/\text{cm}^2 = 6.45 \mu\text{A}/\text{inch}^2$.

Figure 83. Graph. Example of low R_p data.

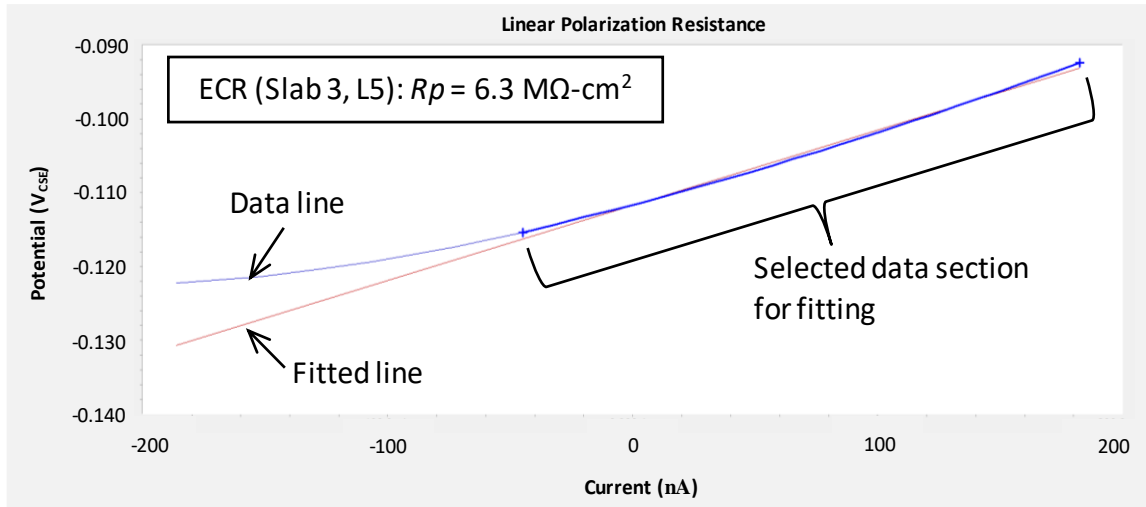


Source: FHWA.

$1 \text{ k}\Omega\text{-cm}^2 = 0.155 \text{ k}\Omega\text{-inch}^2$.

$1 \mu\text{A}/\text{cm}^2 = 6.45 \mu\text{A}/\text{inch}^2$.

Figure 84. Graph. Example of intermediate R_p data.



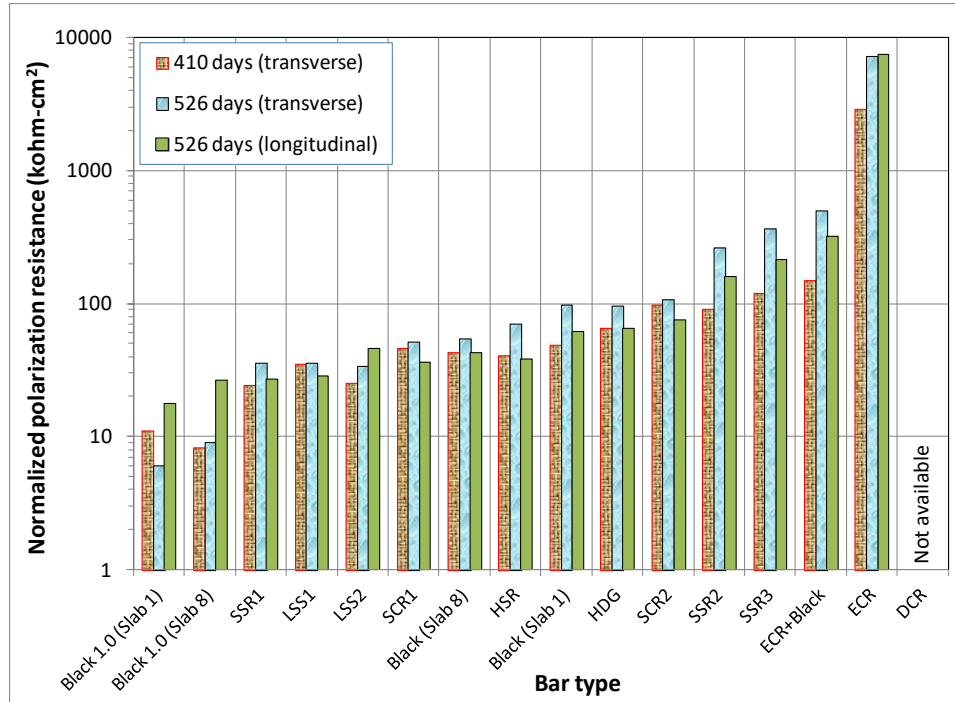
Source: FHWA

$1 \text{ M}\Omega\text{-cm}^2 = 155 \text{ M}\Omega\text{-inch}^2$.

$1 \mu\text{A/cm}^2 = 6.45 \mu\text{A/inch}^2$.

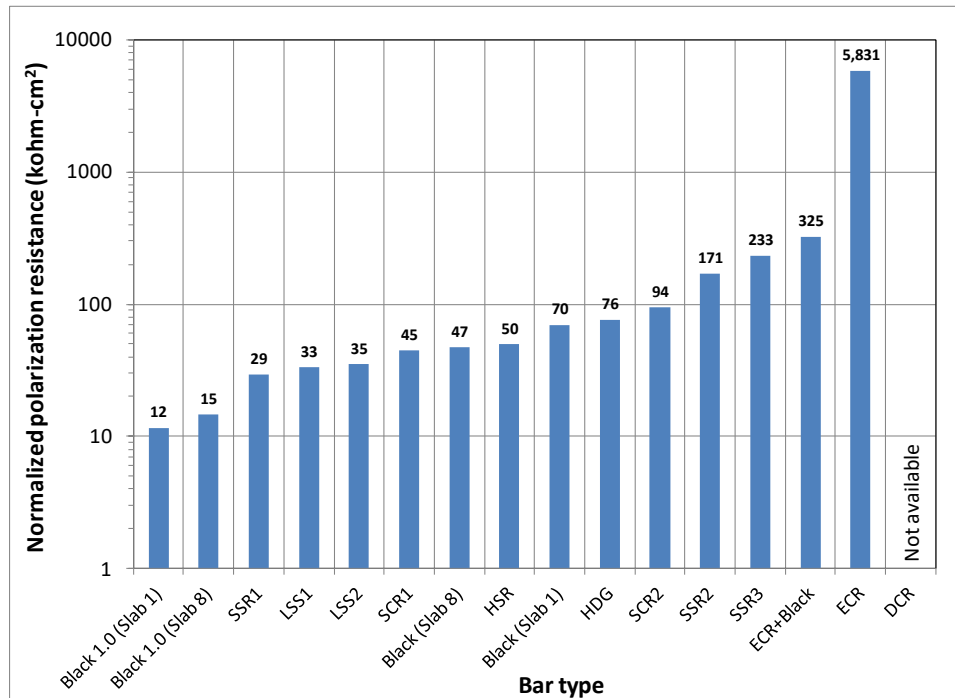
Figure 85. Graph. Example of high R_p data.

Figure 86 shows mean normalized R_p data of different bar materials determined at two different times: only top transverse bars at 410 d and both top transverse and longitudinal bars at 526 d. Figure 87 presents overall mean normalized R_p data of the same materials. Neither plot contains R_p data for DCR due to erratic behaviors during the LPR measurement. It is speculated that a zinc layer beneath epoxy coating might cause an instability problem for the instrument. Figure 87 clearly shows that black bars in 1-inch (labeled as "Black 1.0") cover and a group of highly corrosion-resistant reinforcing bars (i.e., SSR2, SSR3, ECR, and DCR) set the lower and the upper limits of R_p , respectively. The slabs containing ECR and DCR in both mats maintained the high R_p as long as the coating was not compromised. The others, including black bars in 2-inch cover, formed an intermediate R_p group.



Source: FHWA.
 $1 \text{ k}\Omega\text{-cm}^2 = 0.155 \text{ k}\Omega\text{-inch}^2$.

Figure 86. Graph. Mean normalized R_p measured at different times.



Source: FHWA.
 $1 \text{ k}\Omega\text{-cm}^2 = 0.155 \text{ k}\Omega\text{-inch}^2$.

Figure 87. Graph. Overall mean normalized R_p .

CHLORIDE ANALYSIS

Table 4 lists the first chloride dataset of eight concrete powder samples taken from six concrete slab sections after 102 d of testing. The sampling locations were chosen based on OCP readings more negative than $-0.300 V_{CSE}$ and two bottom mats that appeared to be in contact with leaked salt water. There was a significant variation in the chloride concentration data, and OCP data of neighboring bars did not correlate well with the corresponding chloride concentrations. For example, the highest chloride concentration of 3,015 ppm was found near a DCR transverse bar (R1) exhibiting an active OCP ($-0.487 V_{CSE}$), but a much lower chloride concentration of 559 ppm was found near a black transverse bar (R4) exhibiting a very active OCP ($-0.628 V_{CSE}$).

Table 4. Chloride concentrations of selective bars at 102 d exhibiting OCP more negative than $-0.300 V_{CSE}$ and two bottom mats exposed to salt water.

Bar Type	Sampling Location	OCP (V_{CSE})	Acid-Soluble Chloride Concentration (ppm)
Black	L1	-0.335	546
Black	Bottom mat	-0.293	1,257
Black 1-inch cover	R4	-0.628	559
LSS2	L1	-0.415	579
SSR1	R2	-0.341	1,176
LSS1	L1	-0.362	1,179
LSS1	Bottom mat	-0.289	507
DCR	R1	-0.487	3,015

Table 5 lists the second chloride concentration dataset of 28 concrete powder samples taken from 14 slab sections soon after corrosion testing was suspended to fix leaking ponding wells. The sampling locations in each slab section were chosen for the bars exhibiting the most positive OCP and the most negative OCP. As observed in table 4, a large variation in chloride data existed, and no apparent relationship was found between the chloride data and the matching OCP data. (The coefficient of determination (R^2) was 0.38.)

Table 5. Chloride concentrations at 193 d based on the most positive and negative OCPs per slab section.

Bar Type	Sampling Location	OCP (V_{CSE})	Acid-Soluble Chloride Concentration (ppm)
Black	L3	-0.195	77
Black	L5	-0.417	1,144
Black 1-inch cover	R6	-0.295	2,042
Black 1-inch cover	R5	-0.584	5,162
SCR1	L2	-0.084	312
SCR1	L1	-0.145	846
ECR + black	R4	-0.113	793
ECR + black	R2	-0.118	100
ECR	L5	-0.080	94
ECR	L1	-0.206	169
SCR2	R1	-0.165	63
SCR2	R5	-0.182	244
LSS2	L3	-0.252	373
LSS2	L5	-0.327	320
HDG	R2	-0.421	1,016
HDG	R5	-0.438	150
HSR	L3	-0.277	374
HSR	L2	-0.430	1,136
SSR1	R3	-0.243	799
SSR1	R4	-0.373	3,300
LSS1	L4	-0.253	325
LSS1	L1	-0.354	578
DCR	R4	-0.362	1,656
DCR	R2	-0.456	1,151
SSR2	R5	-0.350	1,292
SSR2	R1	-0.374	1,226
SSR3	L2	-0.226	1,500
SSR3	L5	-0.233	587

Final chloride concentration data and chloride diffusion coefficients are summarized in table 6 through table 21 as part of the autopsy results. The latter were caused by corrosion-induced damage in slabs 1R and 8R. Table 22 presents key statistical parameters of the final chloride data in terms of count, maximum, minimum, mean, median, standard deviation, and coefficient of variance (CV). Mean chloride concentrations were 5,516 ppm at 1 inch and 1,718 ppm at 2 inches. These concentrations were sufficient to initiate corrosion of black bars and those having low chloride threshold values. However, they were not enough to induce corrosion on some corrosion-resistant bar materials possessing high chloride threshold values, such as solid stainless

steel bars and stainless steel-clad bars. Based on small differences between mean and median values at each sampling depth, the final chloride data were thought to follow the normal distribution. However, large CV values confirmed that individual chloride data at each sampling depth still varied significantly, probably due to concrete heterogeneity.

Table 6. Black bar autopsy results (slab 1L).

Bar Type	Core ID	Core		Condition of Extracted Bar	Acid-Soluble Chloride Concentration (ppm)						Chloride Diffusion Coefficient (m ² /s)
		Length (Inch)	Condition		0.0625 Inch	0.125 Inch	0.5 Inch	1 Inch	2 Inches	4 Inches	
Black	L1-1	5.0	Intact	Small rust spots	—	—	—	—	1,976	—	—
Black	L1-2	3.5	Intact	Small rust spots at one end	—	—	—	—	1,449	—	—
Black	L1-3	5.0	Intact	Small rust spots	—	7,795	9,429	6,209	1,306	90	2.2 × 10 ⁻¹¹
Black	L2-1	5.0	Intact	Small rust spots	4,026	—	—	—	1,298	—	—
Black	L2-2	4.5	Intact	Small rust spots	—	7,766	9,449	6,209	1,625	65	2.8 × 10 ⁻¹¹
Black	L2-3	5.0	Intact	Small rust spots and end corrosion	—	—	—	—	—	—	—
Black	L5-1	3.5	Intact	Small rust spots	—	—	—	—	1,339	—	—
Black	L5-2	4.0	Intact	Small rust spots	—	—	—	—	2,366	—	—
Black	L5-3	4.0	Intact	Small rust spots and end corrosion	—	—	—	—	2,450	—	—
Black	L6-1	4.5	Intact	Small rust spots	—	9,312	9,857	4,814	1,388	84	1.7 × 10 ⁻¹¹
Black	L6-2	3.5	Intact	Small rust spots	4,880	—	—	—	2,362	—	—
Black	L6-3	5.0	Intact	Small rust spots and end corrosion	—	—	—	—	3,416	—	—
Black	L3-1	4.5	Intact	—	—	—	—	—	—	—	—
Black	L3-2	4.0	Intact	Small rust spots	—	—	—	—	—	—	—
Black	L3-3	3.5	Intact	—	—	—	—	—	—	—	—
Black	L4-1	4.0	Intact	—	—	—	—	—	—	—	—
Black	L4-2	4.0	Intact	—	—	—	—	—	—	—	—
Black	L4-3	4.0	Intact	—	—	—	—	—	—	—	—
Mean					N/A	8,291	9,578	5,744	1,907	80	2.2 × 10⁻¹¹

1 m²/s = 4.9 × 10¹⁰ inch²/yr; N/A = not applicable.

—Information was not available because no testing was performed as a result of limited budget or disintegrated cores.

Table 7. Black bar autopsy results (slab 8L).

Bar Type	Core ID	Core		Condition of Extracted Bar	Acid-Soluble Chloride Concentration (ppm)						Chloride Diffusion Coefficient (m ² /s)
		Length (Inches)	Condition		0.0625 Inch	0.125 Inch	0.5 Inch	1 Inch	2 Inches	4 Inches	
Black	L1-1	5.0	Intact	Rust spots	—	—	—	—	583	—	—
Black	L1-2	3.5	Intact	Rust spots	—	—	—	—	525	—	—
Black	L1-3	4.5	Intact	Rust spots	—	—	—	—	1,269	—	—
Black	L2-1	5.0	Intact	Rust spots	—	1,746	5,502	3,026	709	62	5.2 × 10 ⁻¹¹
Black	L2-2	3.5	Intact	Clean	—	—	—	—	1,306	—	—
Black	L2-3	3.5	Intact	Clean	—	—	—	—	775	—	—
Black	L5-1	3.5	Intact	Rust spots	—	—	—	—	—	—	—
Black	L5-2	3.5	Intact	Rust spots	1,456	—	—	—	1,360	—	—
Black	L5-3	5.5	Intact	Rust spots	—	—	—	—	2,499	—	—
Black	L6-1	4.0	Intact	Rust spots	2,351	—	—	—	943	—	—
Black	L6-2	4.5	Intact	Rust spots	—	5,820	8,171	5,002	1,458	81	2.8 × 10 ⁻¹¹
Black	L6-3	3.5	Intact	Rust spots	—	—	—	—	1,253	—	—
Black	L3-1	5.0	Intact	—	—	3,162	6,343	3,750	—	76	7.7 × 10 ⁻¹¹
Black	L3-2	2.5	Intact	—	—	—	—	—	—	—	—
Black	L3-3	5.0	Intact	—	—	—	—	—	—	—	—
Black	L4-1	5.0	Intact	—	—	—	—	—	—	—	—
Black	L4-2	4.0	Intact	—	—	—	—	—	—	—	—
Black	L4-3	3.5	Intact	—	—	—	—	—	—	—	—
Mean					N/A	3,576	6,672	3,926	1,153	73	5.2 × 10⁻¹¹

1 m²/s = 4.9 × 10¹⁰ inch²/yr; N/A = not applicable.

—Information was not available because no testing was performed as a result of limited budget or disintegrated cores.

Table 8. Black bar (1-inch cover) autopsy results (slab 1R).

Bar Type	Core ID	Core		Condition of Extracted Bar	Acid-Soluble Chloride Concentration (ppm)						Chloride Diffusion Coefficient (m ² /s)
		Length (Inches)	Condition		0.0625 Inch	0.125 Inch	0.5 Inch	1 Inch	2 Inches	4 Inches	
Black (1-inch cover)	R1-1	5.0	Cracked at bar	—	—	—	—	—	—	—	—
Black (1-inch cover)	R1-2	5.0	Cracked at bar	—	—	—	—	—	—	—	—
Black (1-inch cover)	R1-3	5.5	Cracked at bar	—	—	—	—	—	—	—	—
Black (1-inch cover)	R2-1	5.5	Cracked at bar	—	—	—	—	—	—	—	—
Black (1-inch cover)	R2-2	5.5	Cracked at bar	—	—	—	—	—	—	—	—
Black (1-inch cover)	R2-3	5.5	Cracked at bar	—	—	—	—	—	—	—	—
Black (1-inch cover)	R5-1	5.5	Cracked at bar	—	—	—	—	—	—	—	—
Black (1-inch cover)	R5-2	5.0	Cracked at bar	—	—	—	—	—	—	—	—
Black (1-inch cover)	R5-3	5.5	Cracked at bar	—	—	—	—	—	—	—	—
Black (1-inch cover)	R6-1	5.5	Cracked at bar	—	—	—	—	—	—	—	—
Black (1-inch cover)	R6-2	—	Fractured	—	—	—	—	—	—	—	—
Black (1-inch cover)	R6-3	4.0	Cracked at bar	—	—	—	—	—	—	—	—
Black (1-inch cover)	R3-1	5.0	Cracked at bar	—	—	—	—	—	—	—	—
Black (1-inch cover)	R3-2	—	Crumbled	—	—	—	—	—	—	—	—
Black (1-inch cover)	R3-3	5.5	Intact	—	—	—	—	—	—	—	—

Bar Type	Core ID	Core		Condition of Extracted Bar	Acid-Soluble Chloride Concentration (ppm)						Chloride Diffusion Coefficient (m ² /s)
		Length (Inches)	Condition		0.0625 Inch	0.125 Inch	0.5 Inch	1 Inch	2 Inches	4 Inches	
Black (1-inch cover)	R4-1	5.5	Cracked at bar	—	—	—	—	—	—	—	—
Black (1-inch cover)	R4-2	5.0	Cracked at bar	—	—	—	—	—	—	—	—
Black (1-inch cover)	R4-3	—	Crumbled	—	—	—	—	—	—	—	—

1 m²/s = 4.9 × 10¹⁰ inch²/yr.

—Information was not available because no testing was performed as a result of limited budget or disintegrated cores.

Table 9. Black bar (1-inch cover) autopsy results (slab 8R).

Bar Type	Core ID	Core		Condition of Extracted Bar	Acid-Soluble Chloride Concentration (ppm)						Chloride Diffusion Coefficient (m ² /s)
		Length (Inches)	Condition		0.0625 Inch	0.125 Inch	0.5 Inch	1 Inch	2 Inches	4 Inches	
Black (1-inch cover)	R1-1	—	Severely damaged	—	—	—	—	—	—	—	—
Black (1-inch cover)	R1-2	—	Severely damaged	—	—	—	—	—	—	—	—
Black (1-inch cover)	R1-3	—	Severely damaged	—	—	—	—	—	—	—	—
Black (1-inch cover)	R2-1	—	Severely damaged	—	—	—	—	—	—	—	—
Black (1-inch cover)	R2-2	—	Severely damaged	—	—	—	—	—	—	—	—
Black (1-inch cover)	R2-3	—	Severely damaged	—	—	—	—	—	—	—	—
Black (1-inch cover)	R5-1	4.0	Cracked at rebar	—	—	—	—	—	—	—	—
Black (1-inch cover)	R5-2	2.5	Cracked at rebar	—	—	—	—	—	—	—	—
Black (1-inch cover)	R5-3	4.5	Cracked at rebar	—	—	—	—	—	—	—	—
Black (1-inch cover)	R6-1	4.0	Cracked at rebar	—	—	—	—	—	—	—	—
Black (1-inch cover)	R6-2	5.0	Cracked at rebar	—	—	—	—	—	—	—	—
Black (1-inch cover)	R6-3	—	Severely damaged	—	—	—	—	—	—	—	—
Black (1-inch cover)	R3-1	3.0	Cracked	—	—	—	—	—	—	—	—
Black (1-inch cover)	R3-2	—	Severely damaged	—	—	—	—	—	—	—	—
Black (1-inch cover)	R3-3	—	Severely damaged	—	—	—	—	—	—	—	—

Bar Type	Core ID	Core		Condition of Extracted Bar	Acid-Soluble Chloride Concentration (ppm)						Chloride Diffusion Coefficient (m ² /s)
		Length (Inches)	Condition		0.0625 Inch	0.125 Inch	0.5 Inch	1 Inch	2 Inches	4 Inches	
Black (1-inch cover)	R4-1	—	Severely damaged	—	—	—	—	—	—	—	—
Black (1-inch cover)	R4-2	—	Severely damaged	—	—	—	—	—	—	—	—
Black (1-inch cover)	R4-3	—	Severely damaged	—	—	—	—	—	—	—	—

1 m²/s = 4.9 × 10¹⁰ inch²/yr.

—Information was not available because no testing was performed as a result of limited budget or disintegrated cores.

Table 10. SCR1 autopsy results (slab 2L).

Bar Type	Core ID	Core		Condition of Extracted Bar	Acid-Soluble Chloride Concentration (ppm)						Chloride Diffusion Coefficient (m ² /s)
		Length (Inches)	Condition		0.0625 Inch	0.125 Inch	0.5 Inch	1 Inch	2 Inches	4 Inches	
SCR 1	L1-1	5.0	Intact	Dark and rust spots	—	—	—	—	—	—	—
SCR 1	L1-2	5.0	Intact	Dark spots	—	8,128	9,294	5,124	1,600	78	2.0 × 10 ⁻¹¹
SCR 1	L1-3	5.0	Intact	Dark and rust spots	—	—	—	—	1,628	—	—
SCR 1	L2-1	5.0	Intact	Dark spots	—	—	—	—	2,412	—	—
SCR 1	L2-2	5.0	Intact	Dark spots	—	—	—	—	2,286	—	—
SCR 1	L2-3	4.5	Intact	Dark spots	—	—	—	—	4,265	—	—
SCR 1	L5-1	5.0	Intact	Clean	—	6,317	9,641	5,789	1,114	77	2.7 × 10 ⁻¹¹
SCR 1	L5-2	5.0	Intact	Dark and rust spots	—	—	—	—	1,695	—	—
SCR 1	L5-3	4.5	Intact	Dark and rust spots	—	—	—	—	1,508	—	—
SCR 1	L6-1	5.0	Intact	Dark and rust spots	—	—	—	—	1,578	—	—
SCR 1	L6-2	4.5	Intact	Dark and rust spots	2,971	—	—	—	1,769	—	—
SCR 1	L6-3	5.0	Intact	Dark and rust spots	—	—	—	—	1,545	—	—
SCR 1	L3-1	5.0	Intact	—	—	—	—	—	—	—	—
SCR 1	L3-2	5.0	Intact	—	—	7,646	9,662	6,422	—	131	5.0 × 10 ⁻¹¹
SCR 1	L3-3	3.0	Intact	—	—	—	—	—	—	—	—
SCR 1	L4-1	3.5	Intact	—	—	—	—	—	—	—	—
SCR 1	L4-2	3.5	Intact	—	—	—	—	—	—	—	—
SCR 1	L4-3	4.0	Intact	—	—	—	—	—	—	—	—
Mean					N/A	7,364	9,532	5,778	1,945	95	3.2 × 10⁻¹¹

1 m²/s = 4.9 × 10¹⁰ inch²/yr; N/A = not applicable.

—Information was not available because no testing was performed as a result of limited budget or disintegrated cores.

Table 11. ECR with black bar bottom mat autopsy results (slab 2R).

Bar Type	Core ID	Core		Condition of Extracted Bar	Acid-Soluble Chloride Concentration (ppm)						Chloride Diffusion Coefficient (m ² /s)	Number of Artificial Defects	Notes
		Length (Inches)	Condition		0.0625 Inch	0.125 Inch	0.5 Inch	1 Inch	2 Inches	4 Inches			
ECR + black	R1-1	5.0	Intact	Clean	2,761	—	—	—	353	—	—	4	Minimal disbonding at defects and knife adhesion test spots
ECR + black	R1-2	5.0	Intact	Clean	—	7,099	9,001	5,586	738	60	2.2×10^{-11}	5	Moderate disbonding at defects and knife adhesion test spots
ECR + black	R1-3	5.5	Intact	Clean	—	—	—	—	572	—	—	5	Moderate disbonding at defects and knife adhesion test spots
ECR + black	R2-1	5.0	Intact	Clean	—	—	—	—	884	—	—	2	Moderate disbonding at defects and knife adhesion test spots
ECR + black	R2-2	5.0	Intact	Clean	—	—	—	—	—	—	—	0	—
ECR + black	R2-3	5.0	Intact	Clean	—	—	—	—	1,332	—	—	3	Significant disbonding at defects and knife adhesion test spots

Bar Type	Core ID	Core		Condition of Extracted Bar	Acid-Soluble Chloride Concentration (ppm)						Chloride Diffusion Coefficient (m ² /s)	Number of Artificial Defects	Notes
		Length (Inches)	Condition		0.0625 Inch	0.125 Inch	0.5 Inch	1 Inch	2 Inches	4 Inches			
ECR + black	R5-1	5.0	Intact	Clean	—	—	—	—	1,745	—	—	0	Minimal disbonding at holidays and significant disbonding at knife adhesion test spots
ECR + black	R5-2	5.5	Intact	Clean	—	7,127	9,983	6,381	1,591	64	6.1×10^{-11}	0	Significant disbonding at knife adhesion test spots
ECR + black	R5-3	5.5	Intact	Clean	—	—	—	—	1,434	—	—	0	Significant disbonding at knife adhesion test spots
ECR + black	R6-1	5.5	Intact	Clean	—	—	—	—	945	—	—	0	Significant disbonding at knife adhesion test spots
ECR + black	R6-2	5.5	Intact	Clean	—	—	—	—	1,608	—	—	0	Significant disbonding at knife adhesion test spots
ECR + black	R6-3	3.5	Intact	Clean	—	—	—	—	1,637	—	—	0	Significant disbonding at knife adhesion test spots

Bar Type	Core ID	Core		Condition of Extracted Bar	Acid-Soluble Chloride Concentration (ppm)						Chloride Diffusion Coefficient (m ² /s)	Number of Artificial Defects	Notes
		Length (Inches)	Condition		0.0625 Inch	0.125 Inch	0.5 Inch	1 Inch	2 Inches	4 Inches			
ECR + black	R3-1	5.5	Intact	—	—	—	—	—	—	—	—	—	N/A
ECR + black	R3-2	5.5	Intact	—	—	5,411	9,087	5,479	—	62	2.9×10^{-11}	—	N/A
ECR + black	R3-3	5.0	Intact	—	—	—	—	—	—	—	—	—	N/A
ECR + black	R4-1	5.5	Intact	—	—	—	—	—	—	—	—	—	N/A
ECR + black	R4-2	5.5	Intact	—	—	—	—	—	—	—	—	—	N/A
ECR + black	R4-3	3.5	Intact	—	—	—	—	—	—	—	—	—	N/A
Mean					N/A	6,546	9,357	5,815	1,167	62	3.7×10^{-11}	N/A	N/A

1 m²/s = 4.9×10^{10} inch²/yr; N/A = not applicable.

—Information was not available because no testing was performed as a result of limited budget or disintegrated cores.

Table 12. ECR autopsy results (slab 3L).

Bar Type	Core ID	Core		Condition of Extracted Bar	Acid-Soluble Chloride Concentration (ppm)						Chloride Diffusion Coefficient (m ² /s)	Number of Artificial Defects	Notes
		Length (Inches)	Condition		0.0625 Inch	0.125 Inch	0.5 Inch	1 Inch	2 Inches	4 Inches			
ECR	L1-1	4.0	Intact	Clean	—	—	—	—	—	—	—	4	—
ECR	L1-2	3.5	Intact	Clean	3,784	—	—	—	2,666	—	—	2	Significant disbonding at defects and knife adhesion test spots
ECR	L1-3	5.0	Intact	Clean	—	6,720	6,694	5,141	2,356	74	3.4×10^{-11}	6	Significant disbonding at defects and knife adhesion test spots
ECR	L2-1	4.5	Intact	Clean	—	—	—	—	1,026	—	—	2	Moderate disbonding at defects and knife adhesion test spots
ECR	L2-2	3.5	Intact	Clean	—	—	—	—	2,565	—	—	3	Moderate disbonding at defects and minimal disbonding knife adhesion test spots
ECR	L2-3	5.0	Intact	Clean	—	—	—	—	1,486	—	—	3	Minimal disbonding at defects and knife adhesion test spots
ECR	L5-1	5.5	Intact	Clean	—	4,918	6,680	4,786	1,374	101	3.2×10^{-11}	1	Significant disbonding at defect and knife adhesion test spots
ECR	L5-2	5.0	Intact	Clean	—	—	—	—	2,153	—	—	1	Significant disbonding at defect and knife adhesion test spots
ECR	L5-3	4.5	Intact	Clean	—	—	—	—	1,298	—	—	0	Significant disbonding at

Bar Type	Core ID	Core		Condition of Extracted Bar	Acid-Soluble Chloride Concentration (ppm)						Chloride Diffusion Coefficient (m ² /s)	Number of Artificial Defects	Notes
		Length (Inches)	Condition		0.0625 Inch	0.125 Inch	0.5 Inch	1 Inch	2 Inches	4 Inches			
													knife adhesion test spots
ECR	L6-1	5.0	Intact	Clean	—	—	—	—	1,224	—	—	0	Significant disbonding at knife adhesion test spots
ECR	L6-2	5.0	Intact	Clean	—	—	—	—	1,268	—	—	0	Significant disbonding at knife adhesion test spots
ECR	L6-3	5.0	Intact	Clean	—	—	—	—	3,602	—	—	0	Significant disbonding at knife adhesion test spots
ECR	L3-1	5.0	Intact	—	—	—	—	—	—	—	—	—	—
ECR	L3-2	5.5	Intact	—	—	6,523	8,504	6,043	—	72	5.3×10^{-11}	—	—
ECR	L3-3	5.0	Intact	—	—	—	—	—	—	—	—	—	—
ECR	L4-1	5.5	Intact	—	—	—	—	—	—	—	—	—	—
ECR	L4-2	3.5	Intact	—	—	—	—	—	—	—	—	—	—
ECR	L4-3	3.5	Intact	—	—	—	—	—	—	—	—	—	—
Mean					N/A	6,054	7,293	5,323	1,911	82	4.0×10^{-11}	N/A	N/A

1 m²/s = 4.9×10^{10} inch²/yr; N/A = not applicable.

—Information was not available because no testing was performed as a result of limited budget or disintegrated cores.

Table 13. SCR2 autopsy results (slab 3R).

Bar Type	Core ID	Core		Condition of Extracted Bar	Acid-Soluble Chloride Concentration (ppm)						Chloride Diffusion Coefficient (m ² /s)
		Length (Inches)	Condition		0.0625 Inch	0.125 Inch	0.5 Inch	1 Inch	2 Inches	4 Inches	
SCR 2	R1-1	3.5	Intact	Dark and rust spots	—	—	—	—	1,341	—	—
SCR 2	R1-2	5.0	Intact	Dark spots	—	—	—	—	1,754	—	—
SCR 2	R1-3	5.0	Intact	Dark spots	—	6,282	7,754	5,293	1,896	77	3.5 × 10 ⁻¹¹
SCR 2	R2-1	5.5	Intact	Dark and rust spots	—	—	—	—	4,523	—	—
SCR 2	R2-2	3.5	Intact	Dark and rust spots	4,759	—	—	—	3,080	—	—
SCR 2	R2-3	5.5	Intact	Dark spots	—	—	—	—	2,309	—	—
SCR 2	R5-1	5.0	Intact	Dark spots	—	—	—	—	2,255	—	—
SCR 2	R5-2	5.0	Intact	Dark spots	—	7,318	8,291	6,333	4,299	91	5.8 × 10 ⁻¹¹
SCR 2	R5-3	5.0	Intact	Dark spots	—	—	—	—	3,343	—	—
SCR 2	R6-1	5.0	Intact	Clean	—	—	—	—	3,770	—	—
SCR 2	R6-2	4.5	Intact	Dark spots	—	—	—	—	2,779	—	—
SCR 2	R6-3	3.5	Intact	Dark spots	—	—	—	—	2,025	—	—
SCR 2	R3-1	5.5	Intact	—	—	—	—	—	—	—	—
SCR 2	R3-2	5.0	Intact	—	—	6,921	8,036	5,740	—	90	4.8 × 10 ⁻¹¹
SCR 2	R3-3	5.5	Intact	—	—	—	—	—	—	—	—
SCR 2	R4-1	3.5	Intact	—	—	—	—	—	—	—	—
SCR 2	R4-2	3.5	Intact	—	—	—	—	—	—	—	—
SCR 2	R4-3	3.5	Intact	—	—	—	—	—	—	—	—
Mean					N/A	6,840	8,027	5,789	2,781	86	4.7 × 10⁻¹¹

1 m²/s = 4.9 × 10¹⁰ inch²/yr; N/A = not applicable.

—Information was not available because no testing was performed as a result of limited budget or disintegrated cores.

Table 14. LSS2 autopsy results (slab 4L).

Bar Type	Core ID	Core		Condition of Extracted Bar	Acid-Soluble Chloride Concentration (ppm)						Chloride Diffusion Coefficient (m ² /s)
		Length (Inches)	Condition		0.0625 Inch	0.125 Inch	0.5 Inch	1 Inch	2 Inches	4 Inches	
LSS2	L1-1	5.0	Intact	Moderate corrosion	—	—	—	—	1,685	—	—
LSS2	L1-2	4.5	Intact	Moderate corrosion	2,878	—	—	—	1,223	—	—
LSS2	L1-3	4.5	Intact	Moderate corrosion and bar end corrosion	—	5,644	7,183	3,526	641	83	2.5 × 10 ⁻¹¹
LSS2	L2-1	4.5	Intact	Moderate corrosion	—	—	—	—	960	—	—
LSS2	L2-2	4.5	Intact	Moderate corrosion	—	—	—	—	1,613	—	—
LSS2	L2-3	4.0	Intact	Moderate corrosion	—	—	—	—	1,531	—	—
LSS2	L5-1	5.0	Intact	Moderate corrosion	—	—	—	—	1,257	—	—
LSS2	L5-2	3.0	Intact	Moderate corrosion	—	—	—	—	2,713	—	—
LSS2	L5-3	3.5	Intact	Moderate corrosion	—	—	—	—	1,324	—	—
LSS2	L6-1	4.5	Intact	Moderate corrosion	—	5,781	7,035	6,312	1,434	118	3.8 × 10 ⁻¹¹
LSS2	L6-2	4.5	Intact	Moderate corrosion	—	—	—	—	2,202	—	—
LSS2	L6-3	3.5	Intact	Moderate corrosion	—	—	—	—	1,537	—	—
LSS2	L3-1	4.5	Intact	—	—	—	—	—	—	—	—
LSS2	L3-2	4.5	Intact	—	—	5,567	8,499	4,332	—	98	6.8 × 10 ⁻¹¹
LSS2	L3-3	4.5	Intact	—	—	—	—	—	—	—	—
LSS2	L4-1	3.5	Intact	—	—	—	—	—	—	—	—
LSS2	L4-2	4.5	Intact	—	—	—	—	—	—	—	—
LSS2	L4-3	3.5	Intact	—	—	—	—	—	—	—	—
Mean					N/A	5,664	7,572	4,723	1,510	100	4.4 × 10⁻¹¹

1 m²/s = 4.9 × 10¹⁰ inch²/yr; N/A = not applicable.

—Information was not available because no testing was performed as a result of limited budget or disintegrated cores.

Table 15. HDG autopsy results (slab 4R).

Bar Type	Core ID	Core		Condition of Extracted Bar	Acid-Soluble Chloride Concentration (ppm)						Chloride Diffusion Coefficient (m ² /s)
		Length (Inches)	Condition		0.0625 Inch	0.125 Inch	0.5 Inch	1 Inch	2 Inches	4 Inches	
HDG	R1-1	4.5	Intact	Black color	—	—	—	—	785	—	—
HDG	R1-2	4.5	Intact	Black color	—	—	—	—	1,099	—	—
HDG	R1-3	3.5	Intact	Black color	—	—	—	—	1,593	—	—
HDG	R2-1	4.5	Intact	Gray color	—	5,957	9,120	5,499	854	278	1.9 × 10 ⁻¹¹
HDG	R2-2	4.5	Intact	Gray/black color	3,609	—	—	—	2,233	—	—
HDG	R2-3	4.5	Intact	Gray/black color	—	—	—	—	2,547	—	—
HDG	R5-1	5.0	Intact	Black color	—	—	—	—	1,537	—	—
HDG	R5-2	5.0	Intact	Gray/black color and rust spot	—	—	—	—	2,410	—	—
HDG	R5-3	5.0	Intact	Gray/black color	—	4,529	8,386	4,014	1,744	92	4.3 × 10 ⁻¹¹
HDG	R6-1	5.0	Intact	Black color	—	—	—	—	1,641	—	—
HDG	R6-2	5.0	Intact	Gray/black color	—	—	—	—	2,982	—	—
HDG	R6-3	5.0	Intact	Black color	—	—	—	—	2,271	—	—
HDG	R3-1	3.0	Split	Gray/black color	—	—	—	—	—	—	—
HDG	R3-2	3.5	Intact	—	—	—	—	—	—	—	—
HDG	R3-3	4.5	Intact	—	—	—	—	—	—	—	—
HDG	R4-1	4.5	Intact	—	—	5,198	9,159	5,932	—	53	4.2 × 10 ⁻¹¹
HDG	R4-2	5.0	Intact	—	—	—	—	—	—	—	—
HDG	R4-3	5.0	Intact	—	—	—	—	—	—	—	—
Mean					N/A	5,228	8,888	5,148	1,808	141	3.5 × 10⁻¹¹

1 m²/s = 4.9 × 10¹⁰ inch²/yr; N/A = not applicable.

—Information was not available because no testing was performed as a result of limited budget or disintegrated cores.

Table 16. HSR autopsy results (slab 5L).

Bar Type	Core ID	Core		Condition of Extracted Bar	Acid-Soluble Chloride Concentration (ppm)						Chloride Diffusion Coefficient (m ² /s)
		Length (Inches)	Condition		0.0625 Inch	0.125 Inch	0.5 Inch	1 Inch	2 Inches	4 Inches	
HSR	L1-1	5.5	Intact	Rust spots	—	—	—	—	1,244	—	—
HSR	L1-2	5.0	Intact	Rust spots	—	6,682	9,791	6,632	2,323	308	4.4 × 10 ⁻¹¹
HSR	L1-3	4.5	Intact	Rust spots	1,920	—	—	—	1,621	—	—
HSR	L2-1	4.5	Cracked	Rust spots and bar end corrosion	—	—	—	—	6,630	—	—
HSR	L2-2	5.0	Intact	Rust spots	—	5,329	9,137	5,871	2,840	62	6.3 × 10 ⁻¹¹
HSR	L2-3	4.0	Intact	Rust spots	—	—	—	—	—	—	—
HSR	L5-1	5.0	Intact	Rust spots	—	—	—	—	1,917	—	—
HSR	L5-2	5.0	Intact	Rust spots	—	5,909	7,978	6,775	2,398	106	4.5 × 10 ⁻¹¹
HSR	L5-3	3.5	Intact	Rust spots	—	—	—	—	961	—	—
HSR	L6-1	4.5	Intact	Rust spots	—	—	—	—	1,338	—	—
HSR	L6-2	4.5	Intact	Rust spots	—	—	—	—	1,675	—	—
HSR	L6-3	4.5	Intact	Rust spots	—	—	—	—	1,500	—	—
HSR	L3-1	5.0	Intact	—	—	—	—	—	—	—	—
HSR	L3-2	5.0	Intact	—	—	—	—	—	—	—	—
HSR	L3-3	4.5	Intact	—	—	—	—	—	—	—	—
HSR	L4-1	3.5	Intact	—	—	—	—	—	—	—	—
HSR	L4-2	4.5	Intact	—	—	5,380	8,720	7,058	—	74	7.6 × 10 ⁻¹¹
HSR	L4-3	5.0	Intact	—	—	—	—	—	—	—	—
Mean					N/A	5,825	8,907	6,584	2,222	138	5.7 × 10⁻¹¹

1 m²/s = 4.9 × 10¹⁰ inch²/yr; N/A = not applicable.

—Information was not available because no testing was performed as a result of limited budget or disintegrated cores.

Table 17. SSR1 autopsy results (slab 5R).

Bar Type	Core ID	Core		Condition of Extracted Bar	Acid-Soluble Chloride Concentration (ppm)						Chloride Diffusion Coefficient (m ² /s)
		Length (Inches)	Condition		0.0625 Inch	0.125 Inch	0.5 Inch	1 Inch	2 Inches	4 Inches	
SSR1	R1-1	5.0	Intact	Rust spots	—	—	—	—	774	—	—
SSR1	R1-2	4.0	Intact	Rust spots	—	—	—	—	1,841	—	—
SSR1	R1-3	5.0	Intact	Rust spots	—	—	—	—	1,753	—	—
SSR1	R2-1	5.0	Intact	Rust spots	—	4,754	7,900	5,156	1,668	92	4.8 × 10 ⁻¹¹
SSR1	R2-2	5.0	Split	Rust spots	—	—	—	—	1,811	—	—
SSR1	R2-3	5.0	Intact	Rust spots	—	—	—	—	4,153	—	—
SSR1	R5-1	5.0	Intact	Rust spots	—	4,227	7,348	5,190	1,232	203	4.9 × 10 ⁻¹¹
SSR1	R5-2	5.0	Intact	Rust spots	—	—	—	—	2,876	—	—
SSR1	R5-3	5.0	Intact	Rust spots	—	—	—	—	2,365	—	—
SSR1	R6-1	3.5	Intact	Rust spots	—	—	—	—	840	—	—
SSR1	R6-2	5.0	Intact	Rust spots	2,829	—	—	—	2,446	—	—
SSR1	R6-3	4.5	Intact	Rust spots	—	—	—	—	3,946	—	—
SSR1	R3-1	3.5	Intact	—	—	—	—	—	—	—	—
SSR1	R3-2	5.0	Intact	—	—	—	—	—	—	—	—
SSR1	R3-3	3.5	Intact	—	—	—	—	—	—	—	—
SSR1	R4-1	5.0	Intact	—	—	4,193	8,783	5,374	—	66	7.8 × 10 ⁻¹¹
SSR1	R4-2	5.0	Intact	—	—	—	—	—	—	—	—
SSR1	R4-3	5.0	Intact	—	—	—	—	—	—	—	—
Mean					N/A	4,391	8,010	5,240	2,142	120	5.8 × 10⁻¹¹

1 m²/s = 4.9 × 10¹⁰ inch²/yr; N/A = not applicable.

—Information was not available because no testing was performed as a result of limited budget or disintegrated cores.

Table 18. LSS1 autopsy results (slab 6L).

Bar Type	Core ID	Core		Condition of Extracted Bar	Acid-Soluble Chloride Concentration (ppm)						Chloride Diffusion Coefficient (m ² /s)
		Length (Inch)	Condition		0.0625 Inch	0.125 Inch	0.5 Inch	1 Inch	2 Inches	4 Inches	
LSS1	L1-1	4.5	Intact	Rust spots	—	6,298	6,996	5,882	1,087	121	1.7 × 10 ⁻¹¹
LSS1	L1-2	4.0	Split	Rust spots	—	7,718	9,083	6,151	1,699	64	2.3 × 10 ⁻¹¹
LSS1	L1-3	3.5	Intact	Rust spots and bar end corrosion	—	—	—	—	2,404	—	—
LSS1	L2-1	3.5	Intact	Clean	—	—	—	—	909	—	—
LSS1	L2-2	4.0	Intact	Rust spots	—	—	—	—	716	—	—
LSS1	L2-3	4.0	Intact	Rust spots and bar end corrosion	—	—	—	—	2,307	—	—
LSS1	L5-1	3.5	Intact	Clean	—	—	—	—	865	—	—
LSS1	L5-2	4.5	Intact	Clean	—	7,437	9,483	6,292	1,757	61	2.4 × 10 ⁻¹¹
LSS1	L5-3	3.5	Intact	Clean	—	—	—	—	2,276	—	—
LSS1	L6-1	3.5	Intact	Rust spots	—	—	—	—	621	—	—
LSS1	L6-2	3.5	Intact	Clean	—	—	—	—	1,389	—	—
LSS1	L6-3	2.5	Intact	Rust spots	—	—	—	—	2,936	—	—
LSS1	L3-1	3.5	Intact	—	—	—	—	—	—	—	—
LSS1	L3-2	3.5	Intact	—	—	—	—	—	—	—	—
LSS1	L3-3	3.5	Intact	—	—	—	—	—	—	—	—
LSS1	L4-1	3.5	Intact	—	—	—	—	—	—	—	—
LSS1	L4-2	5.5	Intact	—	—	—	—	—	—	—	—
LSS1	L4-3	4.0	Intact	—	—	—	—	—	—	—	—
Mean					N/A	7,151	8,521	6,108	1,581	82	2.1 × 10⁻¹¹

1 m²/s = 4.9 × 10¹⁰ inch²/yr; N/A = not applicable.

—Information was not available because no testing was performed as a result of limited budget or disintegrated cores.

Table 19. DCR autopsy results (slab 6R).

Bar Type	Core ID	Core		Condition of Extracted Bar	Acid-Soluble Chloride Concentration (ppm)						Chloride Diffusion Coefficient t (m^2/s)	Number of Artificial Defects	Notes
		Length (Inches)	Condition		0.0625 Inch	0.125 Inch	0.5 Inch	1 Inch	2 Inches	4 Inches			
DCR	R1-1	5.0	Intact	Clean	—	6,866	7,786	3,545	305	81	2.2×10^{-11}	8	Moderate disbonding at defects and knife adhesion test spots
DCR	R1-2	5.0	Intact	Clean	—	—	—	—	355	—	—	6	Minimal disbonding at defects and knife adhesion test spots
DCR	R1-3	5.0	Intact	Clean	—	—	—	—	2,138	—	—	6	Moderate disbonding at defects and minimal disbonding at knife adhesion test spots
DCR	R2-1	5.0	Intact	Clean	—	—	—	—	468	—	—	3	Minimal disbonding at defects and knife adhesion test spots
DCR	R2-2	3.5	Intact	Clean	3,306	—	—	—	501	—	—	3	Moderate disbonding at defects and knife adhesion test spots
DCR	R2-3	4.0	Intact	Clean	—	—	—	—	586	—	—	1	Minimal disbonding at defect and knife adhesion test spots
DCR	R5-1	5.0	Intact	Clean	—	—	—	—	729	—	—	0	Moderate disbonding at knife adhesion test spots
DCR	R5-2	5.0	Intact	Clean	—	7,863	9,694	6,142	1,536	84	2.8×10^{-11}	0	Minimal disbonding at

Bar Type	Core ID	Core		Condition of Extracted Bar	Acid-Soluble Chloride Concentration (ppm)						Chloride Diffusion Coefficient (m ² /s)	Number of Artificial Defects	Notes
		Length (Inches)	Condition		0.0625 Inch	0.125 Inch	0.5 Inch	1 Inch	2 Inches	4 Inches			
													knife adhesion test spots
DCR	R5-3	4.5	Intact	Clean	—	—	—	—	936	—	—	1	Minimal disbonding at defect and knife adhesion test spots
DCR	R6-1	3.0	Intact	Clean	—	—	—	—	611	—	—	0	Moderate disbonding at knife adhesion test spots
DCR	R6-2	4.5	Intact	Clean	—	—	—	—	855	—	—	0	Moderate disbonding at knife adhesion test spots
DCR	R6-3	4.5	Intact	Clean	—	—	—	—	1,191	—	—	0	Moderate disbonding at knife adhesion test spots
DCR	R3-1	3.5	Intact	—	—	—	—	—	—	—	—	—	—
DCR	R3-2	4.0	Intact	—	—	—	—	—	—	—	—	—	—
DCR	R3-3	2.5	Intact	Clean	—	—	—	—	—	—	—	—	—
DCR	R4-1	4.5	Intact	—	—	—	—	—	—	—	—	—	—
DCR	R4-2	5.0	Intact	—	—	7,888	8,346	5,529	—	73	4.2×10^{-11}	—	—
DCR	R4-3	4.5	Intact	—	—	—	—	—	—	—	—	—	—
Mean					N/A	7,539	8,609	5,072	851	79	3.0×10^{-11}	N/A	N/A

1 m²/s = 4.9×10^{10} inch²/yr; N/A = not applicable.

—Information was not available because no testing was performed as a result of limited budget or disintegrated cores.

Table 20. SSR2 autopsy results (slab 7L).

Bar Type	Core ID	Core		Condition of Extracted Bar	Acid-Soluble Chloride Concentration (ppm)						Chloride Diffusion Coefficient (m ² /s)
		Length (Inches)	Condition		0.0625 Inch	0.125 Inch	0.5 Inch	1 Inch	2 Inches	4 Inches	
SSR2	L1-1	3.5	Intact	Clean	—	—	—	—	514	—	—
SSR2	L1-2	3.5	Intact	Clean	—	—	—	—	784	—	—
SSR2	L1-3	2.5	Intact	Clean	—	—	—	—	330	—	—
SSR2	L2-1	3.0	Intact	Clean	—	—	—	—	770	—	—
SSR2	L2-2	4.0	Intact	Clean	2,834	—	—	—	2,452	—	—
SSR2	L2-3	2.5	Intact	Clean	—	—	—	—	636	—	—
SSR2	L5-1	4.0	Intact	Clean	—	—	—	—	669	—	—
SSR2	L5-2	3.5	Intact	Clean	—	—	—	—	1,514	—	—
SSR2	L5-3	4.5	Intact	Clean	—	—	—	—	2,342	—	—
SSR2	L6-1	4.5	Intact	Clean	—	5,501	8,518	5,819	548	117	3.0 × 10 ⁻¹¹
SSR2	L6-2	3.5	Intact	Clean	—	—	—	—	932	—	—
SSR2	L6-3	5.0	Intact	Clean	—	5,370	9,021	5,255	1,926	135	4.5 × 10 ⁻¹¹
SSR2	L3-1	4.5	Intact	—	—	5,567	9,070	6,804	—	109	6.4 × 10 ⁻¹¹
SSR2	L3-2	4.0	Intact	—	—	—	—	—	—	—	—
SSR2	L3-3	—	—	—	—	—	—	—	—	—	—
SSR2	L4-1	4.0	Intact	—	—	—	—	—	—	—	—
SSR2	L4-2	3.5	Intact	—	—	—	—	—	—	—	—
SSR2	L4-3	4.5	Intact	Clean	—	—	—	—	—	—	—
Mean					N/A	5,479	8,870	5,959	1,118	120	4.6 × 10⁻¹¹

1 m²/s = 4.9 × 10¹⁰ inch²/yr; N/A = not applicable.

—Information was not available because no testing was performed as a result of limited budget or disintegrated cores.

Table 21. SSR3 autopsy results (slab 7R).

Bar Type	Core ID	Core		Condition of Extracted Bar	Acid-Soluble Chloride Concentration (ppm)						Chloride Diffusion Coefficient (m ² /s)
		Length (Inches)	Condition		0.0625 Inch	0.125 Inch	0.5 Inch	1 Inch	2 Inches	4 Inches	
SSR3	R1-1	3.5	Intact	Rust stain	—	—	—	—	1,522	—	—
SSR3	R1-2	5.0	Intact	Rust stain	—	6,242	9,440	5,071	1,169	124	2.9 × 10 ⁻¹¹
SSR3	R1-3	5.0	Intact	Rust stain	—	—	—	—	4,288	—	—
SSR3	R2-1	5.5	Intact	Rust stain	—	—	—	—	807	—	—
SSR3	R2-2	5.0	Intact	Rust stain at bar end corrosion	—	—	—	—	769	—	—
SSR3	R2-3	5.5	Intact	Rust stain and bar end corrosion	—	—	—	—	4,012	—	—
SSR3	R5-1	5.5	Intact	Rust stain	—	—	—	—	765	—	—
SSR3	R5-2	3.5	Intact	Rust stain and bar end corrosion	—	—	—	—	1,594	—	—
SSR3	R5-3	3.0	Intact	Rust stain	—	—	—	—	2,651	—	—
SSR3	R6-1	5.5	Intact	Rust stain	—	4,635	8,170	5,565	1,202	54	4.3 × 10 ⁻¹¹
SSR3	R6-2	5.5	Intact	Rust stain	—	4,779	8,606	5,604	2,325	84	5.5 × 10 ⁻¹¹
SSR3	R6-3	3.5	Intact	Rust stain	—	—	—	—	2,314	—	—
SSR3	R3-1	3.0	Intact	—	—	—	—	—	—	—	—
SSR3	R3-2	4.5	Intact	—	—	—	—	—	—	—	—
SSR3	R3-3	—	—	—	—	—	—	—	—	—	—
SSR3	R4-1	5.0	Intact	—	—	—	—	—	—	—	—
SSR3	R4-2	5.5	Intact	—	—	5,930	8,868	6,228	—	146	6.4 × 10 ⁻¹¹
SSR3	R4-3	4.0	Intact	—	—	—	—	—	—	—	—
Mean					N/A	5,397	8,771	5,617	1,952	102	4.8 × 10⁻¹¹

1 m²/s = 4.9 × 10¹⁰ inch²/yr; N/A = not applicable.

—Information was not available because no testing was performed as a result of limited budget or disintegrated cores.

Table 22. Key statistical parameters of final chloride data.

Sampling Depth (Inches)	Number of Samples	Acid-Soluble Chloride Concentration (ppm)					CV (Percent)
		Maximum	Minimum	Mean	Median	Standard Deviation	
0.0625	14	4,880	1,456	3,169	2,925	979	30.9
0.125	44	9,312	1,746	6,074	5,944	1,428	23.5
0.5	44	9,983	5,502	8,489	8,663	1,045	12.3
1.0	44	7,058	3,026	5,516	5,595	922	16.7
2.0	162	6,630	305	1,718	1,537	981	57.1
4.0	44	308	53	98	84	52	52.7

Table 23 lists the mean chloride diffusion coefficients of each slab section based on three coefficients and also provides the overall mean coefficient, standard deviation, and CV. The concrete used in this study was fairly porous, with a chloride diffusion coefficient one order of magnitude higher (e.g., 1.0×10^{-11} m²/s (0.49 inch²/yr)) compared to ordinary normal concrete used in the field bridge decks (e.g., 1.0×10^{-12} m²/s (0.049 inch²/yr). As intended, such a porous concrete facilitated corrosion initiation of some bar materials with low chloride threshold values. Considering significant variations in chloride concentrations and chloride diffusion coefficient data, test slabs employed in this study seemed to have different concrete qualities that varied locally.

Table 23. Mean chloride diffusion coefficients of test slabs.

Slab ID	Bar Type	Mean Chloride Diffusion Coefficient (m²/s)
Slab 1L	Black	2.21×10^{-11}
Slab 2L	SCR1	3.23×10^{-11}
Slab 2R	ECR + black	3.70×10^{-11}
Slab 3L	ECR	3.96×10^{-11}
Slab 3R	SCR2	4.69×10^{-11}
Slab 4L	LSS2	4.37×10^{-11}
Slab 4R	HDG	3.46×10^{-11}
Slab 5L	HSR	5.73×10^{-11}
Slab 5R	SSR1	5.83×10^{-11}
Slab 6L	LSS1	2.13×10^{-11}
Slab 6R	DCR	3.04×10^{-11}
Slab 7L	SSR3	4.63×10^{-11}
Slab 7R	SSR2	4.77×10^{-11}
Slab 8L	Black	5.22×10^{-11}
Overall mean		4.12×10^{-11}
Standard deviation		1.73×10^{-11}
CV (percent)		41.9

1 m²/s = 4.9 × 10¹⁰ inch²/yr.

CONDITION EVALUATION OF EXTRACTED BAR SAMPLES

Figure 88 through figure 176 present photographs of extracted bar samples. At least two bar samples exposed to the highest and the lowest chloride concentrations per slab section are shown. Each core ID starts with a bar ID, as described in the earlier core extraction subsection, followed by the coring location: 1 (left), 2 (middle), or 3 (right). Each bar sample corresponds to a pair of figures: the first figure shows the overall condition of the sample, and the second figure shows a close-up view of unique features of the sample. Whenever additional features need to be presented for a particular sample or bar material, more photographs are provided. Some core photographs and bar imprints are also shown to describe certain conditions or phenomena.

Black Reinforcing Steel (Slabs 1 and 8)

The cores taken from 1-inch black bar slab sections (slab 1R) were either cracked or fractured during coring, and the extracted bars were severely corroded, as shown in figure 88 and figure 89. Those taken from slab 8R with a 1-inch cover were also severely damaged, even though the slab was added to the study at a later time. No chloride analysis could be done with the disintegrated cores, but excessive chloride accumulation at the shallow cover must have been responsible for these conditions.



Source: FHWA.

Figure 88. Photo. Corrosion-damaged slab 1R with a 5-2 core ID (black bar at 1-inch cover).



Source: FHWA.

Figure 89. Photo. Corrosion-damaged slab 1R with a 3-2 core ID (black bar at 1-inch cover).

Figure 90 shows a black bar sample in slab 1L exposed to the lowest $[Cl^-]_{\text{interface@2-inch}}$ of 1,298 ppm, and figure 91 shows a close-up view of corrosion on the same bar.



Source: FHWA.

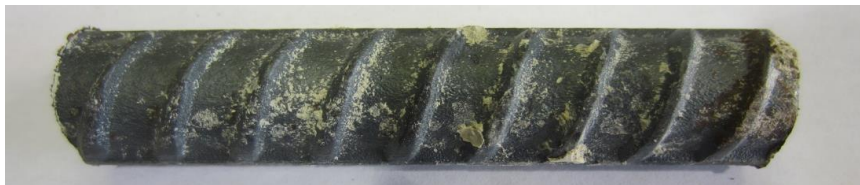
Figure 90. Photo. Extracted black bar from slab 1L with a 2-1 core ID ($[Cl^-]_{\text{interface@2-inch}} = 1,298$ ppm).



Source: FHWA.

Figure 91. Photo. Close-up view of the bar shown in figure 90.

Figure 92 and figure 93 show another bar exposed to the highest $[\text{Cl}^-]_{\text{interface@2-inch}}$ of 3,416 ppm in slab 1L.



Source: FHWA.

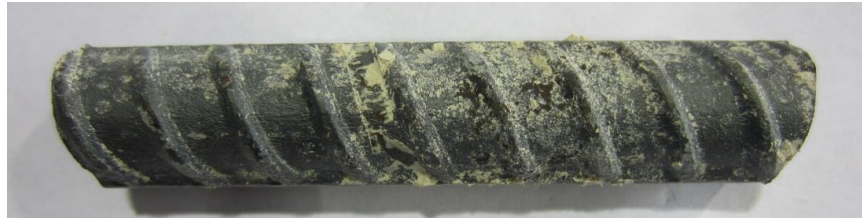
Figure 92. Photo. Extracted black bar from slab 1L with a 6-3 core ID ($[\text{Cl}^-]_{\text{interface@2-inch}} = 3,416$ ppm).



Source: FHWA.

Figure 93. Photo. Close-up view of the bar shown in figure 92.

Figure 94 shows a black bar sample exposed to the lowest $[Cl^-]_{\text{interface@2-inch}}$ of 525 ppm in slab 8L, and figure 95 shows a close-up view of corrosion on the same bar.



Source: FHWA.

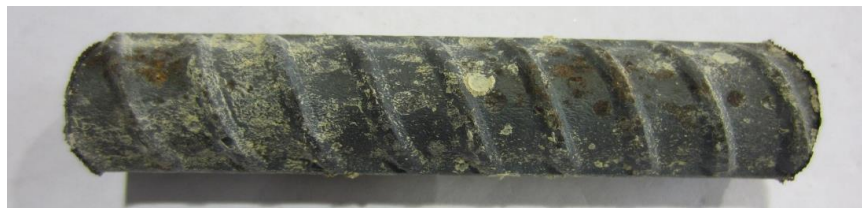
Figure 94. Photo. Extracted black bar from slab 8L with a 1-2 core ID ($[Cl^-]_{\text{interface@2-inch}} = 525$ ppm).



Source: FHWA.

Figure 95. Photo. Close-up view of the bar shown in figure 94.

Figure 96 and figure 97 show another bar exposed to the highest $[Cl^-]_{\text{interface@2-inch}}$ of 2,499 ppm. The level of corrosion observed on four black bar samples with a 2-inch cover was insignificant compared to that observed on samples with a 1-inch cover due to relatively low chloride concentrations.



Source: FHWA.

Figure 96. Photo. Extracted black bar from slab 8L with a 5-3 core ID ($[Cl^-]_{\text{interface@2-inch}} = 2,499$ ppm).



Source: FHWA.

Figure 97. Photo. Close-up view of the bar shown in figure 96.

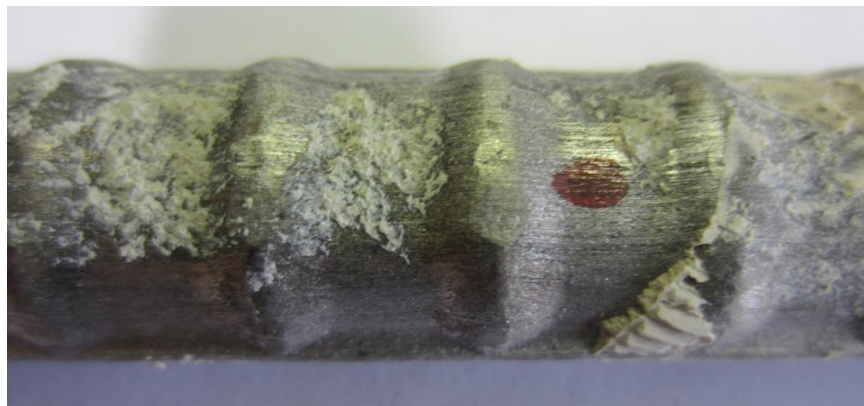
SCR1 (Slab 2L)

Figure 98 shows an SCR1 sample exposed to the lowest $[Cl^-]_{\text{interface@2-inch}}$ of 1,114 ppm in slab 2L, and figure 99 shows a close-up view of the same bar.



Source: FHWA.

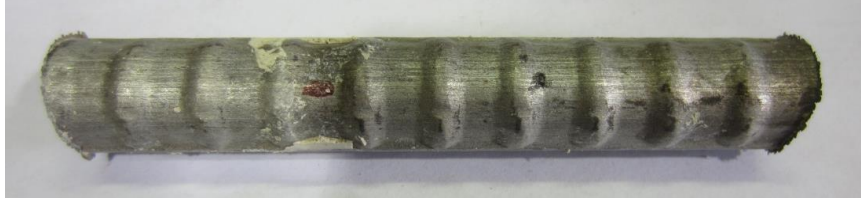
Figure 98. Photo. Extracted SCR1 from slab 2L with a 5-1 core ID ($[Cl^-]_{\text{interface@2-inch}} = 1,114$ ppm).



Source: FHWA.

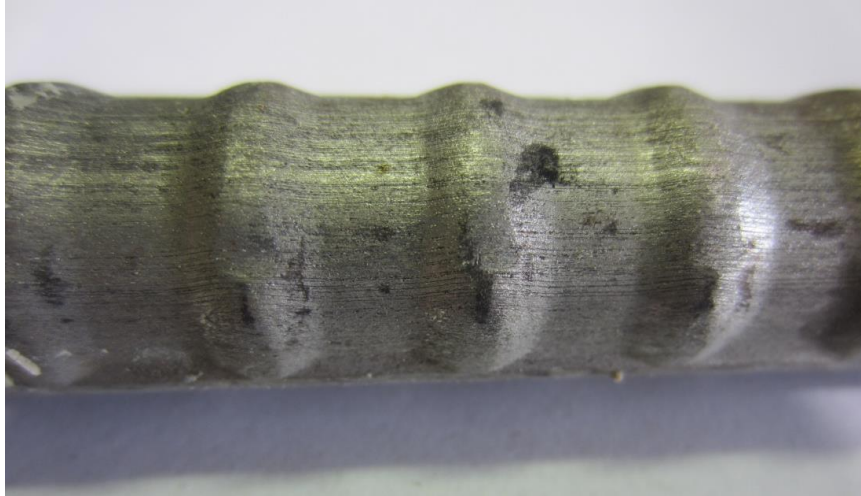
Figure 99. Photo. Close-up view of the bar shown in figure 98.

Figure 100 and figure 101 show another SCR1 bar exposed to the highest $[Cl^-]_{\text{interface@2-inch}}$ of 4,265 ppm in slab 2L.



Source: FHWA.

Figure 100. Photo. Extracted SCR1 from slab 2L with a 2-3 core ID ($[Cl^-]_{\text{interface@2-inch}} = 4,265 \text{ ppm}$).



Source: FHWA.

Figure 101. Photo. Close-up view of the bar shown in figure 100.

The extracted SCR1 samples showed a clean condition with some dark spots regardless of $[Cl^-]_{\text{interface@2-inch}}$. Magnified dark spots revealed rust stains and small pits, as shown in figure 102 and figure 103. The same figures show many tiny ridge lines parallel to the bar length, which served as pit initiation sites (see figure 103). Although these corrosion spots were insignificant compared to the entire bar surface, the long-term implications of this type of defect are currently unknown.



Source: FHWA.

Figure 102. Photo. Rust spot and two pits observed on an SCR1 sample from slab 2L with a 6-1 core ID ($[Cl]_{\text{interface@2-inch}} = 1,578$ ppm).



Source: FHWA.

Figure 103. Photo. Small pits on another SCR1 sample from slab 2L with a 1-3 core ID ($[Cl]_{\text{interface@2-inch}} = 1,628$ ppm).

ECR Top Mat/Black Bar Bottom Mat (Slab 2R)

Figure 104 shows an ECR sample exposed to the lowest $[Cl]_{\text{interface@2-inch}}$ of 353 ppm in slab 2R. Figure 105 and figure 106 show close-up views of the same bar after artificial coating defects were peeled off. Figure 105-A shows an artificial coating defect, and figure 106-A shows a knife adhesion spot next to another artificial coating defect. Figure 105-B and figure 106-B show conditions after the coating was removed. Coating adhesion appeared to be strong with minimal detachment.



Source: FHWA.

Figure 104. Photo. Extracted ECR from slab 2R with a 1-1 core ID ($[Cl^-]_{\text{interface@2-inch}} = 353 \text{ ppm}$).



Source: FHWA.

A. Before coating removal.



Source: FHWA.

B. After coating removal.

Figure 105. Photos. Close-up view of the bar shown in figure 104.



Source: FHWA.

A. Before coating removal.



Source: FHWA.

B. After coating removal.

Figure 106. Photos. Knife adhesion test results on the bar shown in figure 104.

Figure 107 shows another ECR exposed to the highest $[Cl^-]_{\text{interface@2-inch}}$ of 1,745 ppm in slab 2R. Figure 108-A and figure 109-A show close-up views of two as-received defects and a knife adhesion test spot, respectively, before coating was removed, while figure 108-B and figure 109-B show conditions after the coating was removed. Coating adhesion was weak with moderate detachment.



Source: FHWA.

Figure 107. Photo. Extracted ECR from slab 2R with a 5-1 core ID ($[Cl^-]_{\text{interface@2-inch}} = 1,745 \text{ ppm}$).



Source: FHWA.

A. Before coating removal.



Source: FHWA.

B. After coating removal.

Figure 108. Photos. Close-up views of the bar shown in figure 107.



Source: FHWA.

A. Before coating removal.



Source: FHWA.

B. After coating removal.

Figure 109. Photos. Knife adhesion test results on the bar shown in figure 107.

Figure 110 shows an ECR sample exhibiting corrosion at an artificial coating defect. Figure 111 shows a close-up of the defect before and after coating was removed (see figure 111-A and figure 111-B, respectively). $[Cl^-]_{\text{interface@2-inch}}$ was 1,332 ppm, which was not considered a high level. An autopsy of the coating defect revealed superficial corrosion, as shown in figure 111-B. Figure 112 shows the condition of the same bar after another coating defect was peeled off and a knife adhesion test was performed. Coating adhesion varied between strong and weak.



Source: FHWA.

Figure 110. Photo. Extracted ECR from slab 2R with a 2-3 core ID ($[Cl]_{\text{interface@2-inch}} = 1,332 \text{ ppm}$).



Source: FHWA.

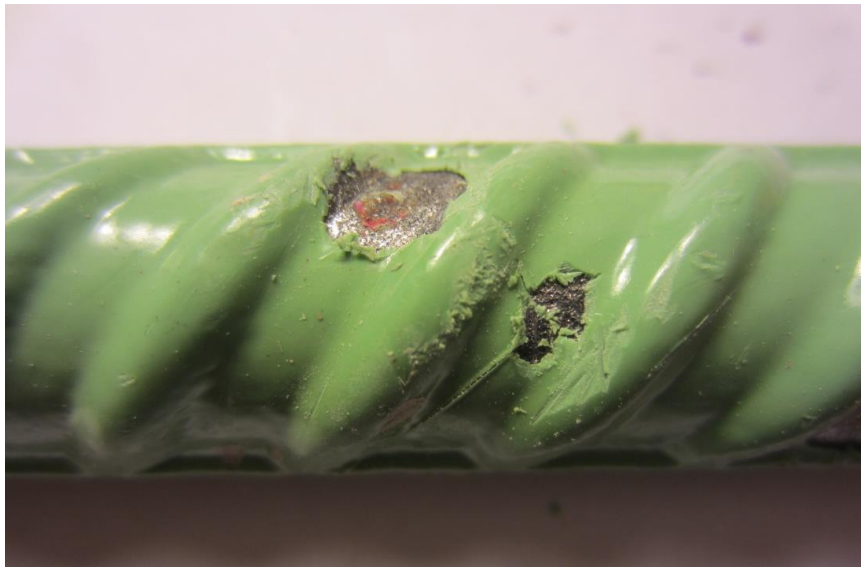
A. Before coating removal.



Source: FHWA.

B. After coating removal.

Figure 111. Photos. Close-up views of the bar shown in figure 110 before and after an artificial coating defect was peeled off.



Source: FHWA.

Figure 112. Photo. Second close-up view of the bar shown in figure 110.

Figure 113 shows the conditions before and after a knife adhesion test of an ECR sample. The sample exhibited the largest coating disbondment observed in this study. No correlation was found between the extent of coating disbondment and $[Cl^-]_{\text{interface@2-inch}}$.



Source: FHWA.

A. Before coating removal.



Source: FHWA.

B. After coating removal.

Figure 113. Photos. The most significant disbondment on an ECR from slab 2R with a 5-3 core ID ($[Cl^-]_{\text{interface@2-inch}} = 1,434$ ppm).

Figure 114 shows a representative condition of coating backside after coating was peeled off. The backside contamination appeared to be normal.



Source: FHWA.

A. After coating removal.



Source: FHWA.

B. Backside of the removed coating.

Figure 114. Photos. Coating backside contamination of an ECR from slab 2R with a 2-3 core ID ($[Cl^-]_{\text{interface@2-inch}} = 1,332$ ppm).

In summary, the extracted ECR samples showed corrosion-free physical appearance even in most of the artificial and as-received coating defects. Also, they exhibited minor to significant coating disbondment around coating defects and knife adhesion test spots.

ECR in Both Mats (Slab 3L)

Figure 115 shows an ECR sample exposed to the lowest $[Cl^-]_{\text{interface@2-inch}}$ of 1,026 ppm in slab 3L. Figure 116 shows a close-up view of the same bar before an artificial coating defect was removed (see figure 116-A) and a knife adhesion spot was autopsied (see figure 116-B). A moderate coating detachment can be seen after the coating was removed.



Source: FHWA.

Figure 115. Photo. Extracted ECR from slab 3L with a 2-1 core ID ($[Cl^-]_{\text{interface@2-inch}} = 1,026$ ppm).



Source: FHWA.

A. Before coating removal.



Source: FHWA.

B. After coating removal.

Figure 116. Photos. Close-up views of the bar shown in figure 115.

Figure 117 shows another ECR sample exposed to the highest $[Cl^-]_{\text{interface@2-inch}}$ of 3,602 ppm in slab 3L. Figure 118 shows of the conditions before and after a knife adhesion test was performed. It reveals a moderate coating disbondment.



Source: FHWA.

Figure 117. Photo. Extracted ECR from slab 3L with a 6-3 core ID ($[Cl^-]_{\text{interface@2-inch}} = 3,602$ ppm).



Source: FHWA.

A. Before coating removal.



Source: FHWA.

B. After coating removal.

Figure 118. Photos. Close-up views of the bar shown in figure 117.

Figure 119 shows the condition of an ECR sample after an artificial coating defect was removed. A powdery corrosion product can be seen beneath the disbonded coating. Figure 120 shows the backside contamination of the epoxy coating, which appeared to be normal.



Source: FHWA.

Figure 119. Photo. Condition beneath a defect from slab 3L with a 5-1 core ID ($[Cl]_{\text{interface@2-inch}} = 1,374$ ppm).



Source: FHWA.

Figure 120. Photo. Coating backside of an ECR from slab 3L with a 5-2 core ID ($[Cl^-]_{\text{interface@2-inch}} = 2,153$ ppm).

Similar to ECRs connected to black bar bottom mats, ECRs in both mats also exhibited excellent corrosion performance without showing rust stains or corrosion damage. Varying degrees of coating disbondment were also observed.

SCR2 (Slab 3R)

Figure 121 shows an SCR2 sample exposed to the lowest $[Cl^-]_{\text{interface@2-inch}}$ of 1,341 ppm in slab 3R, and figure 122 shows a close-up view of a distinctive corrosion spot on the same bar.



Source: FHWA.

Figure 121. Photo. Extracted SCR2 from slab 3R with a 1-1 core ID ($[Cl^-]_{\text{interface@2-inch}} = 1,341$ ppm).



Source: FHWA.

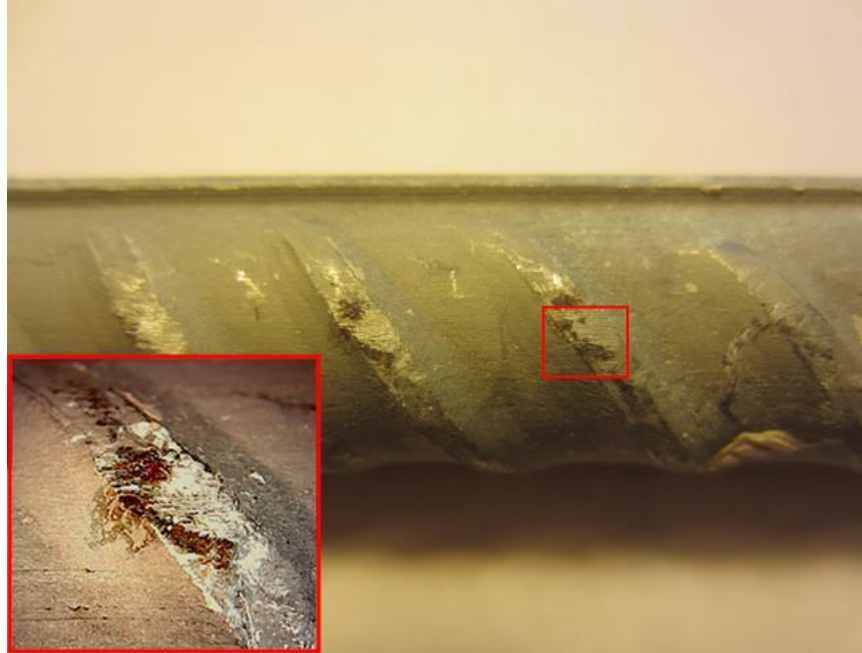
Figure 122. Photo. Close-up view of the bar shown in figure 121.

Figure 123 shows another SCR2 bar exposed to the highest $[Cl^-]_{\text{interface@2-inch}}$ of 4,523 ppm in the same slab section. Figure 124-A shows a close-up view of the same bar containing corrosion spots. A corrosion spot highlighted with a red square clearly shows corrosion product in a magnified image, as shown in Figure 124-B. This SCR2 exhibited dark spots, which were caused by light reflection at shiny scratch spots. Some of them exhibited very light corrosion.



Source: FHWA.

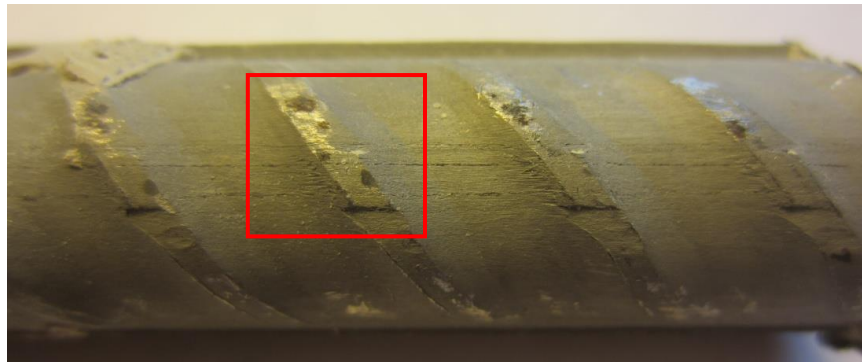
Figure 123. Photo. Extracted SCR2 from slab 3R with a 2-1 core ID ($[Cl^-]_{\text{interface@2-inch}} = 4,523$ ppm).



Source: FHWA.

Figure 124. Photo. Close-up view of the bar shown in figure 123.

Figure 125 also shows dark spots (one such area is indicated by a red square) on the deformation lugs, and figure 126 shows a magnified dark spot, which turned out to be rust. Figure 126 also shows crack-like fine parallel lines on the bar surface, which seemed to be manufacturing defects.



Source: FHWA.

Figure 125. Photo. Extracted SCR2 from slab 3R with a 2-2 core ID ($[Cl]_{\text{interface@2-inch}} = 3,080 \text{ ppm}$).

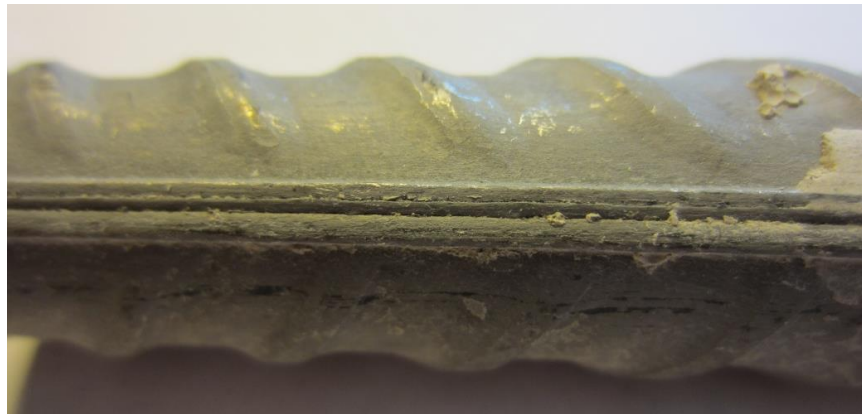


Source: FHWA.

Note: This figure is not directly correlated with the defects and rust spots highlighted in the red box in figure 125.

Figure 126. Photo. Close-up view of manufacturing defects and rust spots shown in figure 125.

Figure 127 shows another type of manufacturing defect: distinctive joining gaps along the rib of an SCR2 sample. No crevice corrosion was found in the gaps in the presence of a high $[\text{Cl}^-]_{\text{interface@2-inch}}$ of 4,299 ppm.



Source: FHWA.

Figure 127. Photo. Visible gap along the rib of an SCR2 from slab 3R with a 5-2 core ID ($[\text{Cl}^-]_{\text{interface@2-inch}} = 4,299$ ppm).

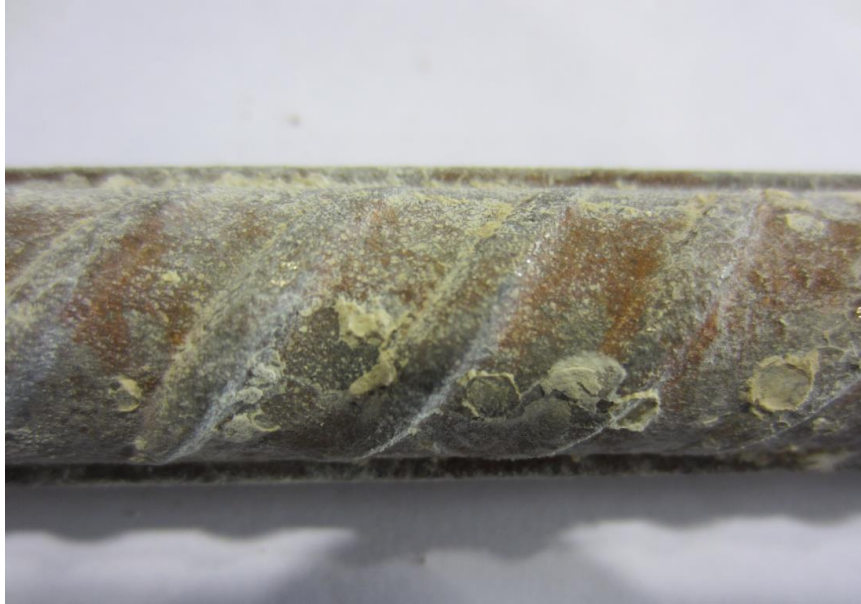
LSS2 (Slab 4L)

Figure 128 shows an LSS2 sample exposed to the lowest $[\text{Cl}^-]_{\text{interface@2-inch}}$ of 641 ppm in slab 4L, and figure 129 shows a close-up view of the same bar exhibiting superficial light corrosion.



Source: FHWA.

Figure 128. Photo. Extracted LSS2 from slab 4L with a 1-3 core ID ($[Cl^-]_{\text{interface@2-inch}} = 641 \text{ ppm}$).



Source: FHWA.

Figure 129. Photo. Close-up view of the bar shown in figure 128.

Figure 130 shows another LSS2 bar exposed to the highest $[Cl^-]_{\text{interface@2-inch}}$ of 2,713 ppm in the same slab section, and figure 131 shows a close-up view of the same bar exhibiting corrosion. Even though $[Cl^-]_{\text{interface@2-inch}}$ was much higher than in the bar shown in figure 129, both bars showed the same corrosion morphology.



Source: FHWA.

Figure 130. Photo. Extracted LSS2 from slab 4L with a 5-2 core ID ($[Cl^-]_{\text{interface@2-inch}} = 2,713 \text{ ppm}$).

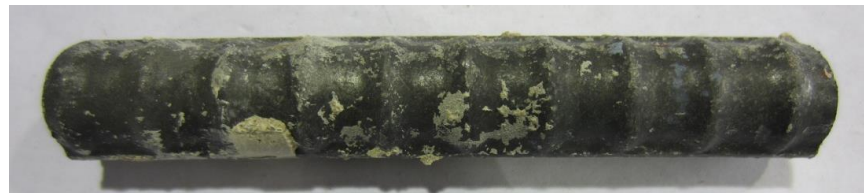


Source: FHWA.

Figure 131. Photo. Close-up view of the bar shown in figure 130.

HDG (Slab 4R)

Figure 132 shows an HDG sample exposed to the lowest $[Cl^-]_{\text{interface@2-inch}}$ of 785 ppm in slab 4R, and figure 133 shows a close-up view of the same bar. It is apparent that the original shiny zinc coating became dark or blackish in color, indicating that zinc was passivated.



Source: FHWA.

Figure 132. Photo. Extracted HDG from slab 4R with a 1-1 core ID ($[Cl^-]_{\text{interface@2-inch}} = 785$ ppm).



Source: FHWA.

Figure 133. Photo. Close-up view of the bar shown in figure 132.

Figure 134 shows another bar exposed to the highest $[Cl^-]_{\text{interface@2-inch}}$ of 2,982 ppm in slab 4R, and figure 135 shows a close-up view of the same bar exhibiting a gray corrosion product.



Source: FHWA.

Figure 134. Photo. Extracted HDG from slab 4R with a 6-2 core ID ($[Cl^-]_{\text{interface@2-inch}} = 2,982$ ppm).



Source: FHWA.

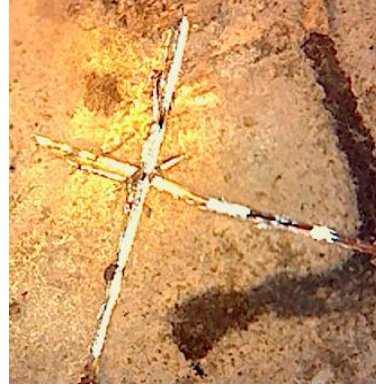
Figure 135. Photo. Close-up view of the bar shown in figure 134.

Figure 136-A shows the remaining zinc layer on the underside of the bar shown in figure 132. Upon scratching the dull gray-colored zinc surface, bright zinc was exposed (see Figure 136-B). When the zinc coating was consumed, a red corrosion product was observed. An example of active corrosion highlighted in a red square is shown in Figure 137-A, and a magnified corrosion product is shown in figure 137-B.



Source: FHWA.

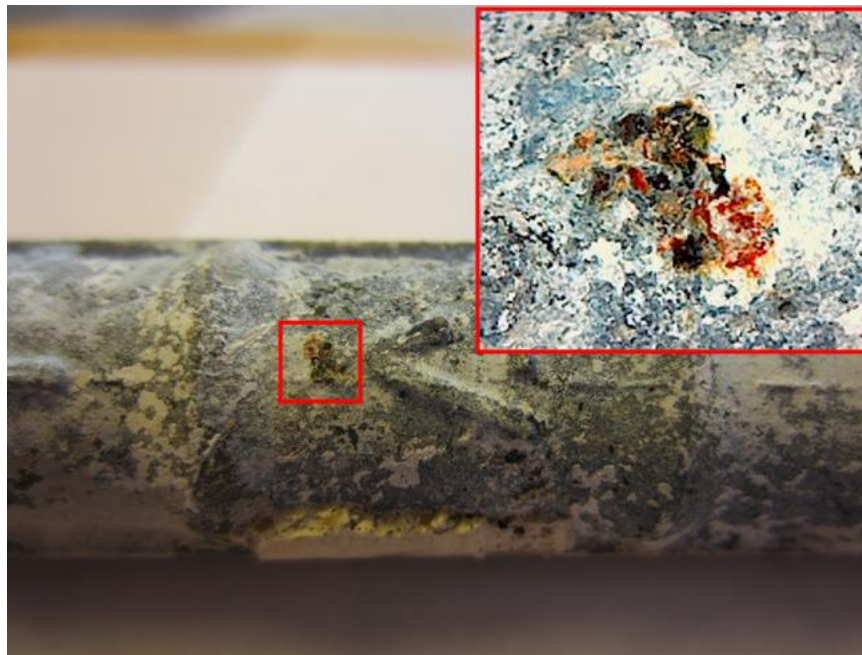
A. Close-up view.



Source: FHWA.

B. Magnified "X" mark.

Figure 136. Photos. Remaining zinc coating on the bar shown in figure 132.



Source: FHWA.

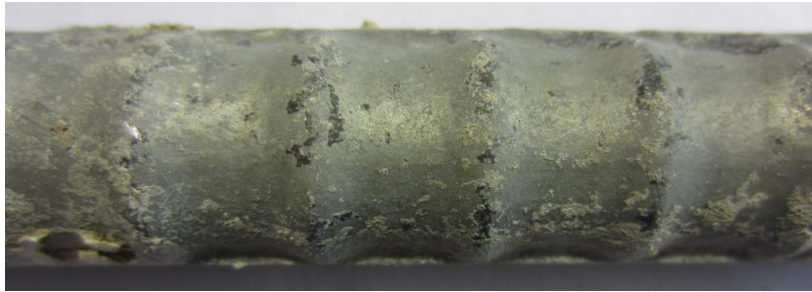
Figure 137. Photo. Close-up view of an extracted HDG from slab 4R with a 5-2 core ID ($[Cl^-]_{\text{interface@2-inch}} = 2,410$ ppm).

One unique feature of HDG is bar imprints covered with zinc that must be transferred from HDG. Figure 138 and figure 139 show an example of a gray-colored bar imprint and the matching HDG sample, respectively. $[Cl^-]_{\text{interface@2-inch}}$ was low at 854 ppm.



Source: FHWA.

Figure 138. Photo. Bar imprint in slab 4R with a 2-1 core ID ($[Cl^-]_{\text{interface@2-inch}} = 854 \text{ ppm}$).



Source: FHWA.

Figure 139. Photo. Matching HDG for the imprint shown in figure 138.

Figure 140 and figure 141 show another pair consisting of a bar imprint and the matching HDG sample found with a high $[Cl^-]_{\text{interface@2-inch}}$ of 2,233 ppm. Figure 141 also shows a distinct color difference between intact zinc (gray) and passivated zinc (black).



Source: FHWA.

Figure 140. Photo. Rebar imprint in slab 4R with a 2-2 core ID ($[Cl^-]_{\text{interface@2-inch}} = 2,233 \text{ ppm}$).



Source: FHWA.

Figure 141. Photo. Matching HDG for the imprint shown in figure 140.

HSR (Slab 5L)

Figure 142 shows an HSR sample exposed to the lowest $[Cl^-]_{\text{interface@2-inch}}$ of 961 ppm in slab 5L, and figure 143 shows a close-up view of the same bar. The figure shows superficial light corrosion formed in some areas.



Source: FHWA.

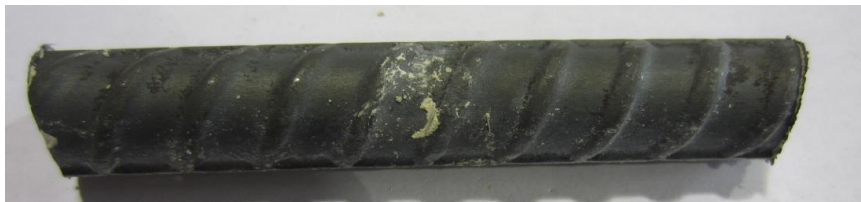
Figure 142. Photo. Extracted HSR from slab 5L with a 5-3 core ID ($[Cl^-]_{\text{interface@2-inch}} = 961$ ppm).



Source: FHWA.

Figure 143. Photo. Close-up view of the bar shown in figure 142.

Figure 144 shows another HSR bar exposed to the highest $[Cl^-]_{\text{interface@2-inch}}$ of 2,398 ppm in the same slab section, and figure 145 shows a close-up view of the same bar exhibiting similar corrosion conditions to those observed on the bar shown in figure 143.



Source: FHWA.

Figure 144. Photo. Extracted HSR from slab 5L with a 5-2 core ID ($[Cl^-]_{\text{interface@2-inch}} = 2,398$ ppm).



Source: FHWA.

Figure 145. Photo. Close-up view of the bar shown in figure 144.

Figure 146 shows the only non-black-bar core that contained a vertical crack extending to the top surface. Because salt water was able to penetrate the crack and reach the bar during the accelerated corrosion testing, $[\text{Cl}^-]_{\text{interface@2-inch}}$ was 6,630 ppm, which was the highest concentration found in this study. Figure 147 shows a severely corroded HSR bar extracted from the cracked core.



Source: FHWA.

Figure 146. Photo. Cracked slab 5L with a 2-1 core ID ($[\text{Cl}^-]_{\text{interface@2-inch}} = 6,630$ ppm).



Source: FHWA.

Figure 147. Photo. Corroded HSR extracted from the core shown in figure 146.

SSR1 (Slab 5R)

Figure 148 shows an SSR1 sample exposed to the lowest $[Cl^-]_{\text{interface@2-inch}}$ of 774 ppm in slab 5R, and figure 149 shows a close-up view of the same bar. It shows negligible corrosion product formed in some surface areas.



Source: FHWA.

Figure 148. Photo. Extracted SSR1 from slab 5R with a 1-1 core ID ($[Cl^-]_{\text{interface@2-inch}} = 774$ ppm).



Source: FHWA.

Figure 149. Photo. Close-up view of the bar shown in figure 148.

Figure 150 shows another SSR1 bar exposed to the highest $[Cl^-]_{interface@2-inch}$ of 4,153 ppm in slab 5R, and figure 151 shows a close-up view of the same bar exhibiting the same kind of corrosion product observed on the bar shown in figure 149. Figure 152 through figure 154 also show similar surface condition, regardless of $[Cl^-]_{interface@2-inch}$.



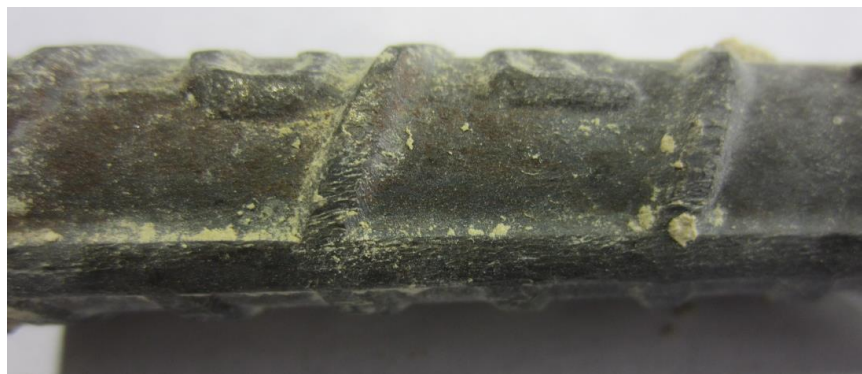
Source: FHWA.

Figure 150. Photo. Extracted SSR1 from slab 5R with a 2-3 core ID ($[Cl^-]_{interface@2-inch} = 4,153$ ppm).



Source: FHWA.

Figure 151. Photo. Close-up view of the bar shown in figure 150.



Source: FHWA.

Figure 152. Photo. Second close-up view of the bar shown in figure 150.



Source: FHWA.

Figure 153. Photo. Corrosion of an SSR1 from slab 5R with a 1-2 core ID ($[Cl^-]_{\text{interface@2-inch}} = 1,841$ ppm).



Source: FHWA.

Figure 154. Photo. Corrosion of a second SSR1 from slab 5R with a 6-2 core ID ($[Cl^-]_{\text{interface@2-inch}} = 2,446$ ppm).

LSS1 (Slab 6L)

Figure 155 shows an LSS1 sample exposed to the lowest $[Cl^-]_{\text{interface@2-inch}}$ of 621 ppm in slab 6L, and figure 156 shows a close-up view of the same bar. It shows a light superficial corrosion product formed in some surface areas.



Source: FHWA.

Figure 155. Photo. Extracted LSS1 from slab 6L with a 6-1 core ID ($[Cl^-]_{\text{interface@2-inch}} = 621$ ppm).



Source: FHWA.

Figure 156. Photo. Close-up view of the bar shown in figure 155.

Figure 157 shows another LSS1 bar exposed to the highest $[Cl^-]_{\text{interface@2-inch}}$ of 2,936 ppm in slab 6L, and figure 158 shows a close-up view of the same bar exhibiting the same kind of corrosion product observed on the bar shown in figure 156. This bar material also exhibited negligible corrosion regardless of $[Cl^-]_{\text{interface@2-inch}}$.



Source: FHWA.

Figure 157. Photo. Extracted LSS1 from slab 6L with a 6-3 core ID ($[Cl^-]_{\text{interface@2-inch}} = 2,936$ ppm).



Source: FHWA.

Figure 158. Photo. Close-up view of the bar shown in figure 157.

DCR (Slab 6R)

Figure 159 shows a DCR sample exposed to the lowest $[Cl^-]_{\text{interface@2-inch}}$ of 305 ppm in slab 6R. Figure 160-A shows a close-up view of the same bar before coat removal, and figure 160-B shows the condition of an artificial defect and a knife adhesion test spot after the coating was peeled off. A moderate disbondment without corrosion can be seen. Figure 161 shows two other areas with the coating removed on the same bar. Similar to figure 160, a moderate coating disbondment was observed. A black ring around the artificial coating defect suggests that the coating disbondment took place in the radial direction, followed by corrosion of the zinc coating in the presence of water and chloride beneath the delaminated coating. Figure 162-A shows the condition of peeled coating, and Figure 162-B shows coating backside that revealed zinc residue adhered to the peeled epoxy coating.



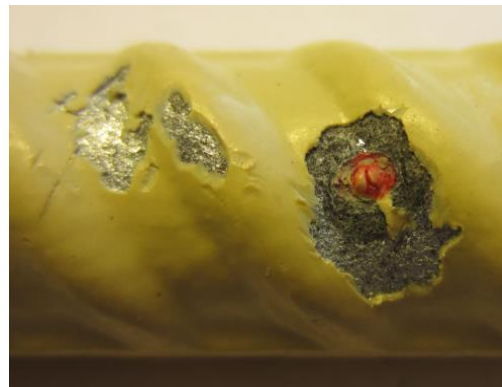
Source: FHWA.

Figure 159. Photo. Extracted DCR from slab 6R with a 1-1 core ID ($[Cl^-]_{\text{interface@2-inch}} = 305$ ppm).



Source: FHWA.

A. Before coating removal.



Source: FHWA.

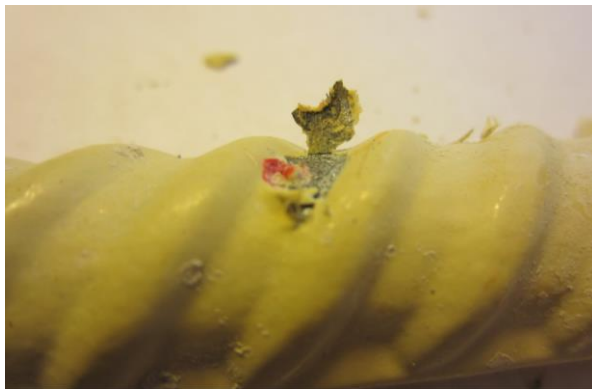
B. After coating removal.

Figure 160. Photos. Close-up views of the bar shown in figure 159.



Source: FHWA.

Figure 161. Photo. A second autopsied area of the bar shown in figure 159.



Source: FHWA.

A. After coating removal.



Source: FHWA.

B. Backside of the removed coating.

Figure 162. Photos. Removed coating from the bar shown in figure 159.

Figure 163 shows another DCR bar exposed to the highest $[Cl^-]_{\text{interface@2-inch}}$ of 2,138 ppm in slab 6R, and figure 164 shows a close-up view of the same bar containing an artificial coating defect filled with corrosion product. Small coating cracks were also formed around the defect. Figure 165-A shows a severely corroded area beneath the coating defect shown in figure 164. Figure 165-B shows the bar condition after the delaminated coating was completely removed. The exposed area exhibited the typical corrosion morphology of steel surrounded by gray-colored zinc corrosion product. The fine coating cracks were caused by active corrosion under the delaminated coating. The coating fragments removed from a corroding area shown in figure 166 showed a mixture of intact zinc layer and reddish corrosion product on their backside.



Source: FHWA.

Figure 163. Photo. Extracted DCR from slab 6R with a 1-3 core ID ($[Cl^-]_{interface@2-inch} = 2,138 \text{ ppm}$).



Source: FHWA.

Figure 164. Photo. Close-up view of the bar shown in figure 163.



Source: FHWA.

A. After partial coating removal.



Source: FHWA.

B. Completely exposed substrate.

Figure 165. Photos. Autopsy of the area shown in figure 164.

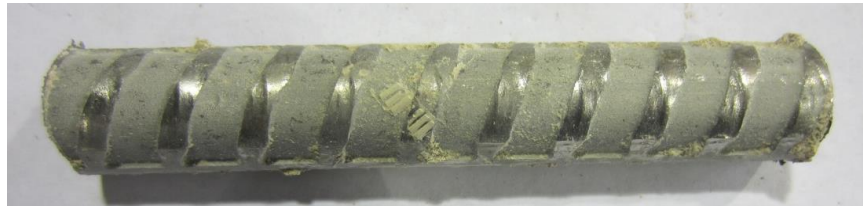


Source: FHWA.

Figure 166. Photo. Coating fragments removed from the area shown in figure 165.

SSR2 (Slab 7L)

Figure 167 shows an SSR2 sample exposed to the lowest $[Cl^-]_{\text{interface@2-inch}}$ of 330 ppm in slab 7L, and figure 168 shows another SSR2 bar exposed to the highest $[Cl^-]_{\text{interface@2-inch}}$ of 2,452 ppm in the same slab section.



Source: FHWA.

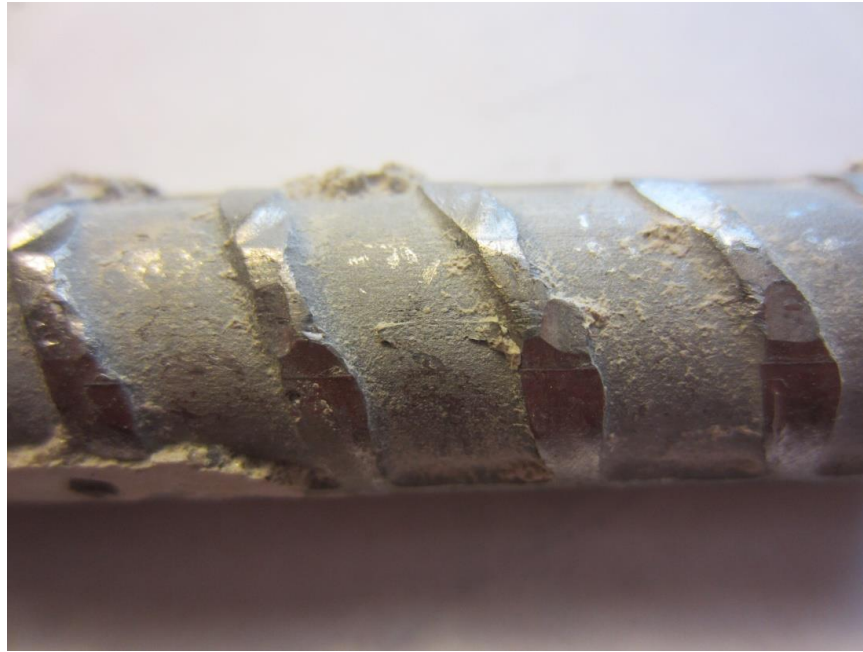
Figure 167. Photo. Extracted SSR2 from slab 7L with a 1-3 core ID ($[Cl^-]_{\text{interface@2-inch}} = 330$ ppm).



Source: FHWA.

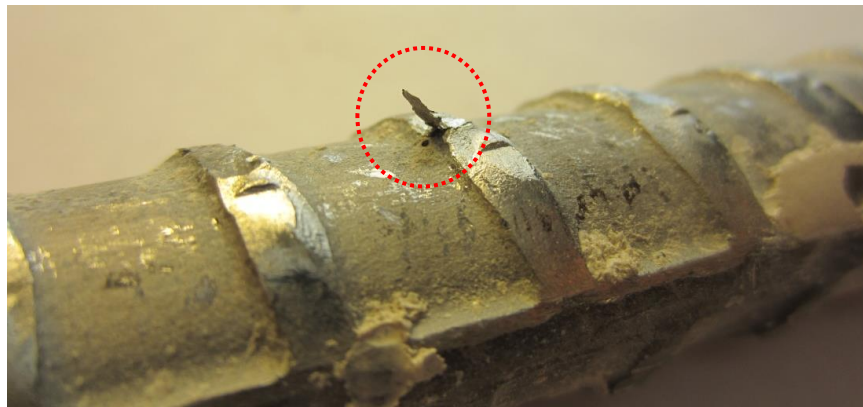
Figure 168. Photo. Extracted SSR2 from slab 7L with a 2-2 core ID ($[Cl^-]_{\text{interface@2-inch}} = 2,452$ ppm).

Figure 169 shows a close-up view of a bar with smashed lugs, which may be related to the production process. A sliver is also found on another SSR2, as shown in figure 170. This bar material exhibited a clean bar surface condition regardless of corrosion concentration.



Source: FHWA.

Figure 169. Photo. Close-up view of an SSR2 from slab 7L with a 6-2 core ID ($[Cl]_{\text{interface@2-inch}} = 932$ ppm).

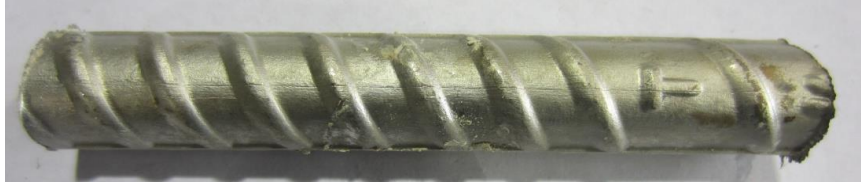


Source: FHWA.

Figure 170. Photo. Sliver on the bar shown in figure 169.

SSR3 (Slab 7R)

Figure 171 shows an SSR3 sample exposed to the lowest $[Cl]_{\text{interface@2-inch}}$ of 765 ppm in slab 7R, and figure 172 shows a close-up view of the same bar showing slight discoloration.



Source: FHWA.

Figure 171. Photo. Extracted SSR3 from slab 7R with a 5-1 core ID ($[Cl^-]_{\text{interface@2-inch}} = 765 \text{ ppm}$).



Source: FHWA.

Figure 172. Photo. Close-up view of the bar shown in figure 171.

Figure 173 shows another SSR3 bar exposed to the highest $[Cl^-]_{\text{interface@2-inch}}$ of 4,288 ppm in the same slab section, and figure 174 shows a close-up view of the same bar exhibiting a small corrosion spot.



Source: FHWA.

Figure 173. Photo. Extracted SSR3 from slab 7R with a 1-3 core ID ($[Cl^-]_{\text{interface@2-inch}} = 4,288 \text{ ppm}$).



Source: FHWA.

Figure 174. Photo. Close-up view of the bar shown in figure 173.

Figure 175 and figure 176 show distinctive signs of surface corrosion, which is rarely seen on solid stainless steel bars.



Source: FHWA.

Figure 175. Photo. Rust on the bar shown in figure 173.



Source: FHWA.

Figure 176. Photo. Powderous corrosion product on an SSR3 bar sample from slab 7R with a 2-3 core ID ($[Cl^-]_{\text{interface@2-inch}} = 4,012 \text{ ppm}$).

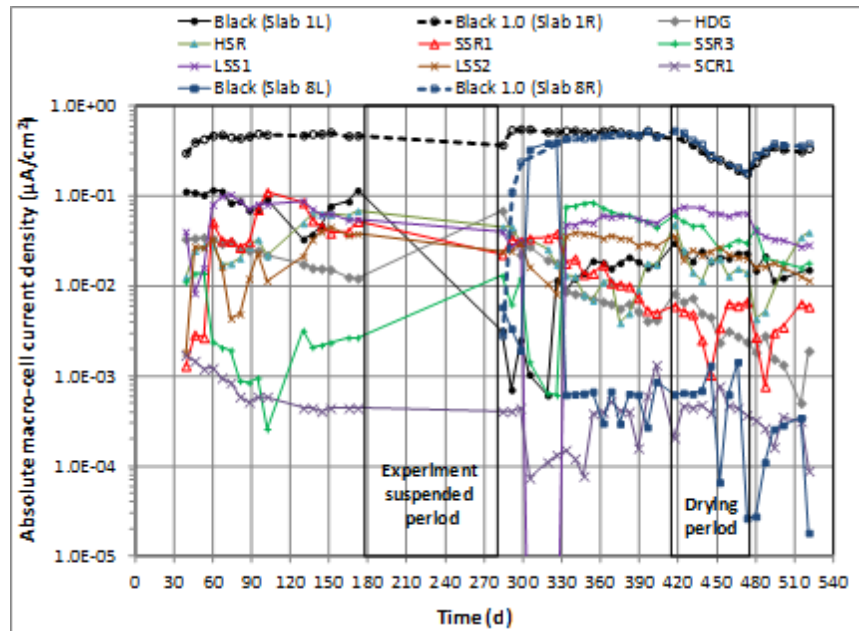
DISCUSSION

The collected OCP data indicate that the existing ASTM C876 criteria were not applicable to some bar materials containing zinc coating, such as HDG and DCR.⁽¹⁷⁾ Separate or modified corrosion criteria are needed to assess the possibility of corrosion for these out-of-specification bar materials.

This study yielded mixed test results regarding the corrosion performance of various metallic reinforcing bars for two reasons. The first and most critical issue was unexpected chloride contamination of the bottom mats by ponded 15 weight percent NaCl solution that leaked down from some of the ponding wells. This unintended corrosion of the bottom mats disturbed the research protocol established for the macro-cell corrosion test setup. Normally, when sufficient amounts of chloride from the deck surface reach the bars in the top mat, they start corroding as the macro-anode. The bars in the bottom mat, without being exposed to chloride, keep consuming electrons as the macro-cathode in the presence of oxygen and water. With this problem of chloride contamination on the bottom mat, the time-to-corrosion initiation for individual bar materials in the top mat could not be determined. Additionally, reversed $I_{\text{macro-cell}}$ flow occurred in the slab sections that initiated corrosion in the bottom mats first. Later, some of these sections went through another current reversal (turning to positive current flow) when their top mat bars also started corroding (as soon as sufficient Cl^- accumulated there). Because individual slab sections had experienced different levels of salt contamination in both the top and bottom mats, the quality of the collected data varied, and thus accurate data analysis could not be done consistently.

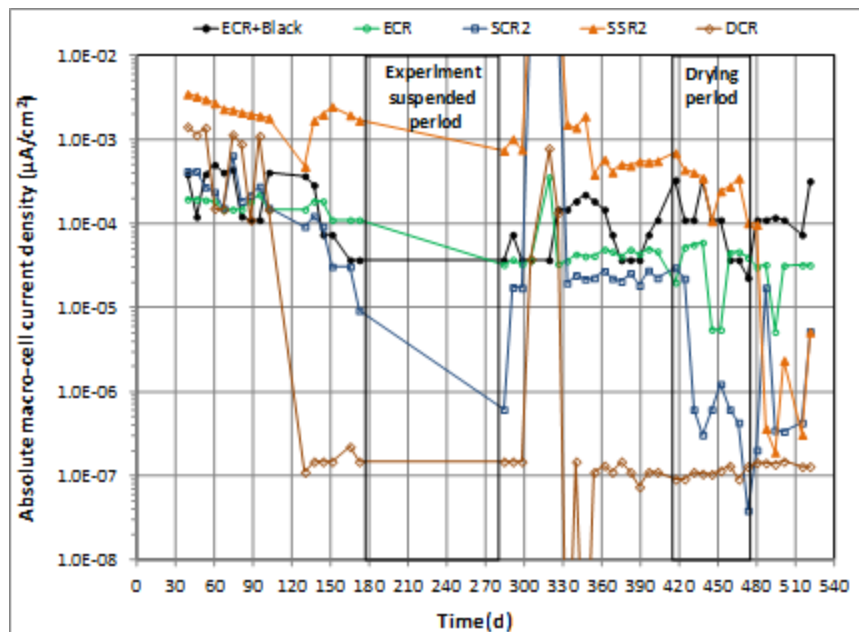
To reduce the impact of the reversed macro-cell current problem, the absolute values of $i_{\text{macro-cell}}$ data were used to construct two plots. Figure 177 shows an absolute $i_{\text{macro-cell}}$ versus time plot for the mediocre and poor performance groups showing relatively high $i_{\text{macro-cell}}$. Figure 178 shows a similar plot for the best performance group showing relatively low $i_{\text{macro-cell}}$. Because of large variations in the data, both plots used different upper and lower limits in the logarithmic scale.

The same data were used to calculate the mean $i_{macro-cell}$ for the entire testing duration, and a bar chart constructed with mean $i_{macro-cell}$ is presented in figure 179. A large variation of the mean $i_{macro-cell}$ data can be seen.



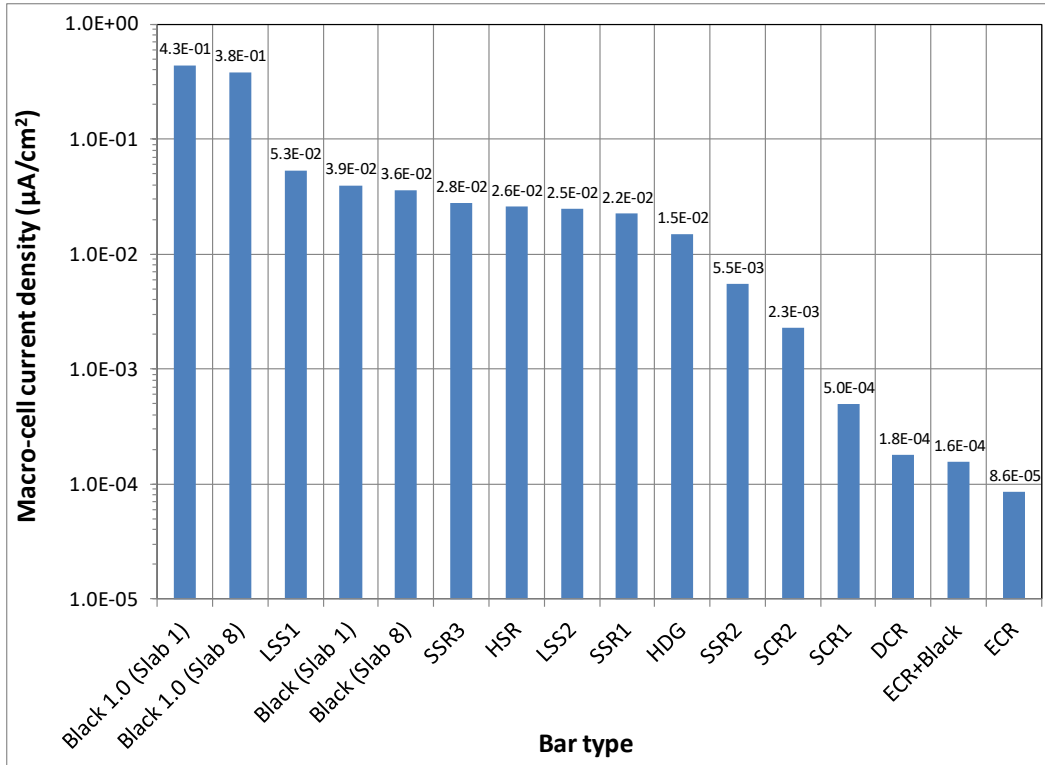
Source: FHWA.
 $1 \mu A/cm^2 = 6.45 \mu A/inch^2$.

Figure 177. Graph. $i_{macro-cell}$ versus time plot for high absolute current group.



Source: FHWA.
 $1 \mu A/cm^2 = 6.45 \mu A/inch^2$.

Figure 178. Graph. $i_{macro-cell}$ versus time plot for low absolute current group.



Source: FHWA.

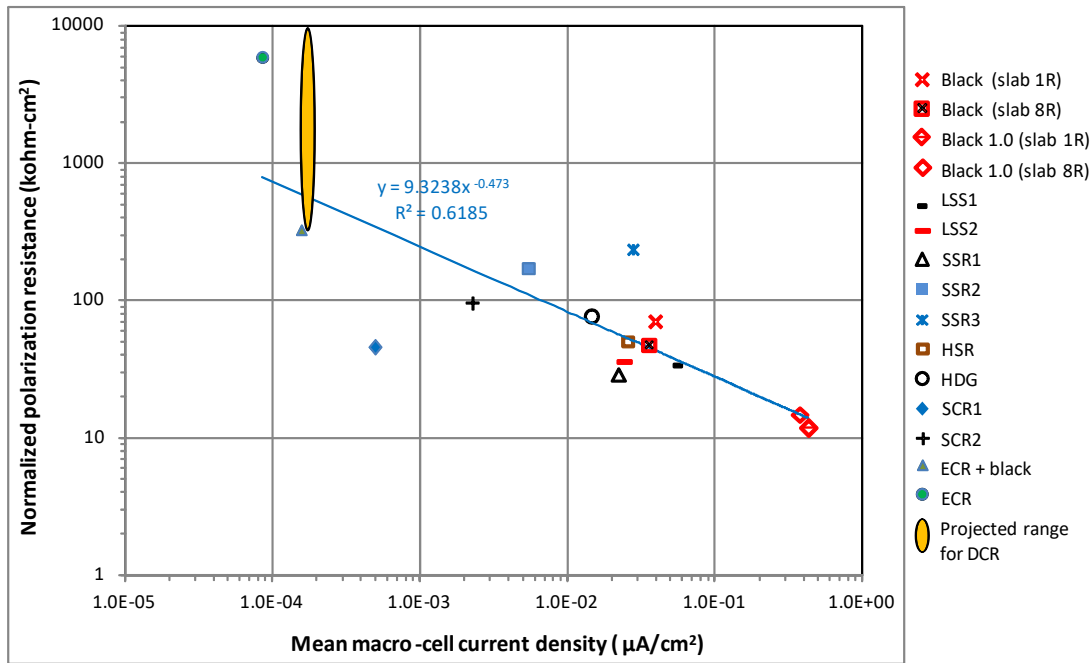
$1 \mu A/cm^2 = 6.45 \mu A/inch^2$.

Figure 179. Graph. Mean $i_{macro-cell}$.

While the best and the poorest performing materials could be easily identifiable with distinctive differences in the data, uncertainties associated with performance ranking existed among mediocre performers, which include SSR1, SSR3, SCR1, HDG, HSR, and LSS2. According to normalized mean R_p data, the following performance ranking for these materials could be attempted from the best to the worst: SSR3 > HDG > HSR \cong SCR1 > LSS2 > SSR1. The black bar in the 2-inch cover exhibited R_p values similar to those of HSR and SCR1. If the mean $i_{macro-cell}$ data were used for the performance ranking, the following order could be established from the best to the worst: SCR1 > HDG > SSR1 \cong LSS2 \cong HSR \cong SSR3. Again, the black bar in 2-inch cover performed similarly to HSR and SSR3. As is discussed in chapter 4, a follow-up laboratory study confirmed that the poor performance of SSR1 was caused by an improper or lack of pickling treatment. The SCR and some low-grade stainless steel bars showed measurable corrosion activity, but the type of corrosion may be less detrimental in an embedded concrete application due to low corrosion intensity in terms of R_p and $i_{macro-cell}$.

Figure 180 shows a scatter plot between the mean $i_{macro-cell}$ data as presented in figure 179 and the corresponding mean normalized R_p data as presented in figure 87 of the tested bar materials. Since R_p data could not be obtained with DCR, a range of possible R_p values was estimated in relation to ECR data on the premise that the former should perform as well as or better than the latter. A linear regression analysis yielded an R^2 of 0.62. If inherent differences between the two electrochemical techniques are taken into account, it can be stated that a reasonable correlation exists between the two sets of data. In other words, the former R_p is determined at the

micro level of corrosion potential and i_{corr} of a metal (thus no external current involved), and the latter ($i_{macro-cell}$) is determined at the macro level of polarized potential involving two dissimilar metals. It is postulated that if the $i_{macro-cell}$ data had been collected with corroding top mat bars and non-corroding bottom mats, a better correlation could have been obtained between the electrochemical tests. The scatter plot shows relative positions among three performance groups. It is interesting to note that the two top performance bar materials within the mediocre group, SSR3 and SCR1, are situated on either side of the fitted regression line.



Source: FHWA.

1 kΩ-cm² = 0.155 kΩ-inch².

1 µA/cm² = 6.45 µA/inch².

Figure 180. Graph. Normalized mean R_p versus mean $i_{macro-cell}$.

The second issue of the present study was related to its duration. The accelerated corrosion testing for 521 d was not long enough to distinguish subtle differences among bar materials possessing similar corrosion characteristics. This has been a common problem for other preceding research studies investigating highly corrosion-resistant reinforcing bars. Moreover, there was almost a 3-yr gap between the core extraction and autopsy. It is possible that the extended storage in the laboratory affected the outcomes of the autopsy due to excessively dried cores. For example, ECR samples extracted from fresh cores can exhibit additional coating delamination due to wet adhesion loss, and some metallic bars may not show powderous corrosion products on their surfaces.

It should be noted that while ECR was one of the best performing materials for this test, considerable variability of performance has been reported in other tests and real-world applications. Since this current study was a short-term corrosion evaluation in a very specific environment, performance of ECR as well as all the rebar types tested may vary depending on the specific factors of installation and environment. Therefore, further durability tests or field

evaluations of existing structures containing various types of metallic reinforcing steel materials are recommended to predict their long-term performance.

CHAPTER 4. A FOLLOW-UP LABORATORY STUDY

A 10-mo follow-up study was carried out to investigate time-to-corrosion initiation for the bar materials employed in the original study. The following describes the experimental details and the findings of the follow-up study.

PREPARATION OF EXPERIMENT

The second laboratory experiment required two sets of new rebar specimens and a test setup as described in the following subsections.

Reinforcing Bars

The same reinforcing bars evaluated in the original study were employed using #5 leftover samples. One exception was the newly acquired #5 black bars, which were clean without any surface rust. Also, three pickled SSR1 bars were included to investigate the effect of acid pickling on the corrosion resistance of SSR1. One of the as-received SSR1 bars was cut into three 6-inch pieces that were subsequently sent to a stainless steel producer for the pickling treatment. Most of the ECR, DCR, and HDG bars contained natural and/or artificial defects to simulate realistic conditions.

Cylindrical Specimens

A total of 39 cylindrical concrete specimens were cast using 4- by 8-inch plastic molds. They were fabricated to measure OCPs and rates of corrosion by the LPR method. Figure 181 through figure 193 show conditions of the individual bar types prior to casting. Three bars of each type were prepared. Each bar was 6 inches long and was suspended from a wood strip that was spanned over the mouth of the mold, as shown in figure 194.



Source: FHWA.

Figure 181. Photo. Black bars.



Source: FHWA.

Figure 182. Photo. ECR bars.



Source: FHWA.

Figure 183. Photo. DCR bars.



Source: FHWA.

Figure 184. Photo. HDG bars.



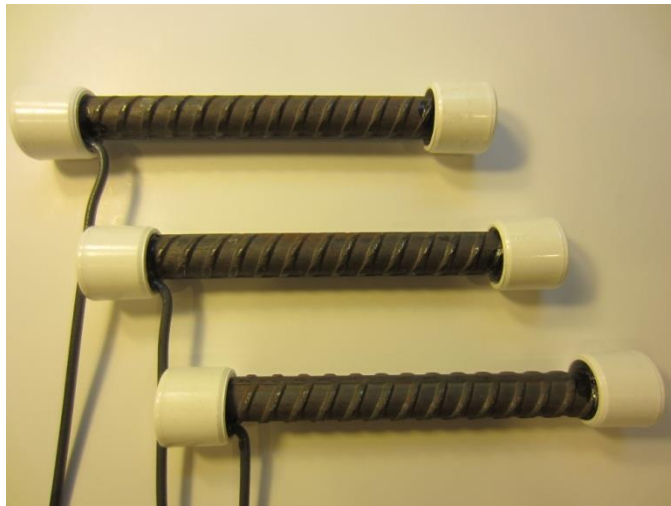
Source: FHWA.

Figure 185. Photo. SCR1 bars.



Source: FHWA.

Figure 186. Photo. SCR2 bars.



Source: FHWA.

Figure 187. Photo. SSR1 bars.



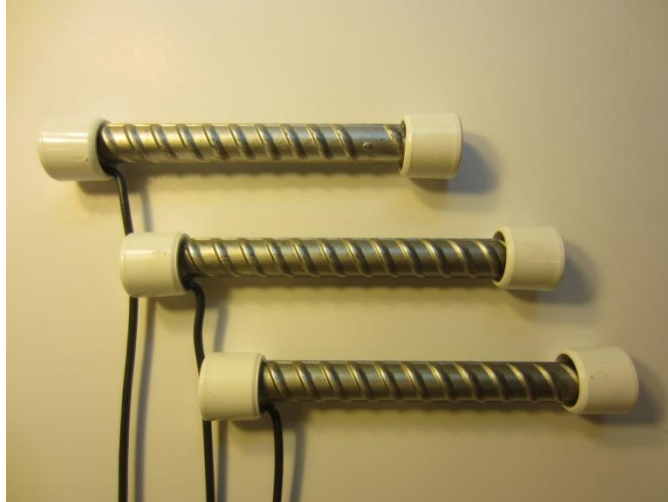
Source: FHWA.

Figure 188. Photo. Pickled SSR1 bars.



Source: FHWA.

Figure 189. Photo. SSR2 bars.



Source: FHWA.

Figure 190. Photo. SSR3 bars.



Source: FHWA.

Figure 191. Photo. HSR bars.



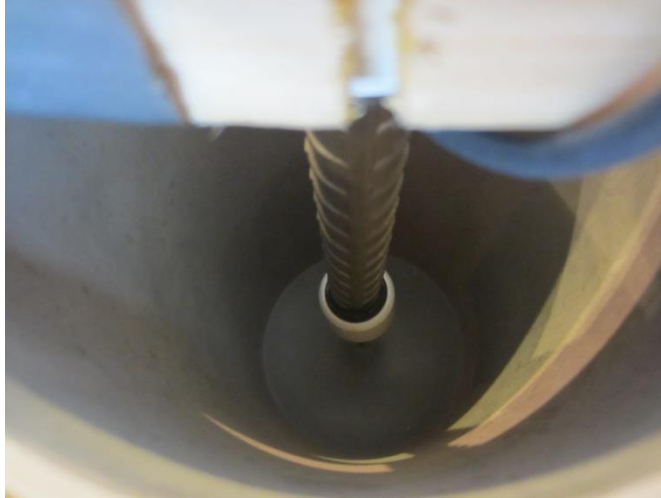
Source: FHWA.

Figure 192. Photo. LSS1 bars.



Source: FHWA.

Figure 193. Photo. LSS2 bars.



Source: FHWA.

Figure 194. Photo. View from above of a suspended bar in an empty mold.

Slab Specimens

In addition to the cylindrical specimens, two 20- by 15- by 4-inch concrete slabs were fabricated to measure OCP and $I_{macro-cell}$. Each bar had a 1.5-inch clear cover. Each slab contained a type 316 stainless steel mesh as the macro-cathode at the bottom of the mold. The macro-cathode was introduced to accelerate corrosion of the macro-anodes, which were the bars in the top section of the slab. A plastic ponding well was installed on the top surface of each slab and filled with 15 weight percent NaCl solution.

Slab #1 accommodated six bar types: ECR, DCR, SCR1, SCR2, SSR2, and SSR3 (see figure 195). Slab #2 contained the remaining bar types: black, HDG, HSR, LSS1, SSR1, and LSS2 (see figure 196). A #4 black and a short LSS2 were used because no more samples were available.



Source: FHWA.

Figure 195. Photo. Slab #1 bars.



Source: FHWA.

Figure 196. Photo. Slab #2 bars.

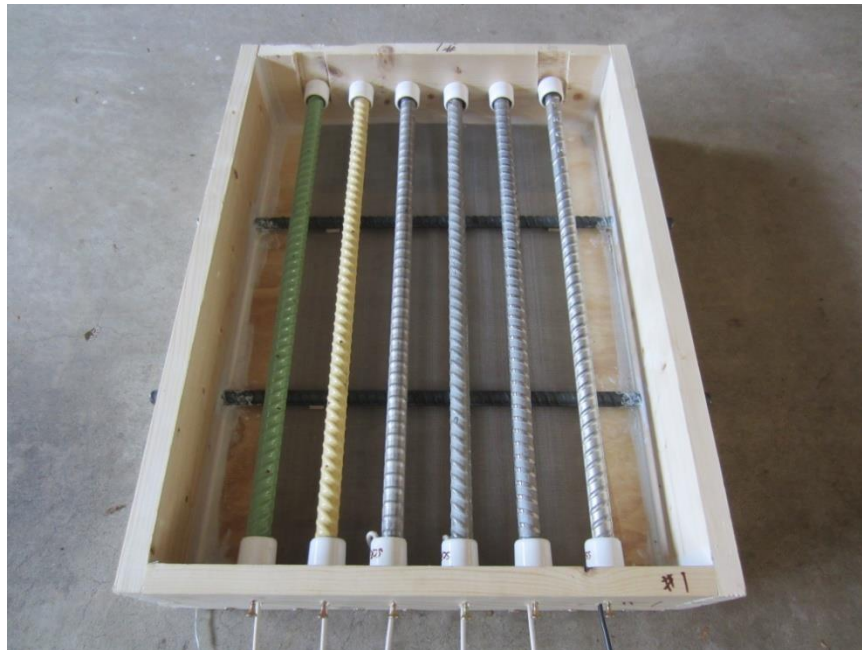
Concrete Casting and Curing

Commercial ready-mix concrete bags (60 lb each) were used to fabricate all of the concrete specimens. The recommended amount of mixing water was used to ensure good-quality concrete representing typical old-generation bridge deck concrete. Figure 197 shows 39 cylindrical molds before pouring concrete. Figure 198 and figure 199 show slab molds that contained the preassigned bars and a stainless steel mesh at the bottom of the mold.



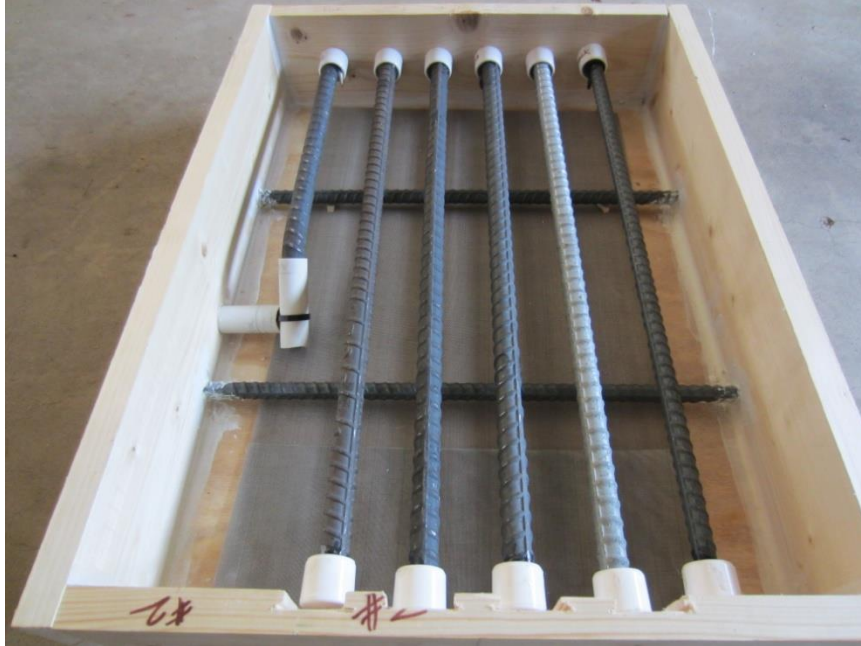
Source: FHWA.

Figure 197. Photo. 4- by 8-inch cylindrical molds ready for casting.



Source: FHWA.

Figure 198. Photo. Slab #1 mold.



Source: FHWA.

Figure 199. Photo. Slab #2 mold.

After concrete casting, the specimens covered with plastic sheeting went through 28-d air curing in the laboratory. Figure 200 shows the concrete specimens being cured, and Figure 201 shows the specimens after they were demolded.



Source: FHWA.

Figure 200. Photo. Specimen curing.

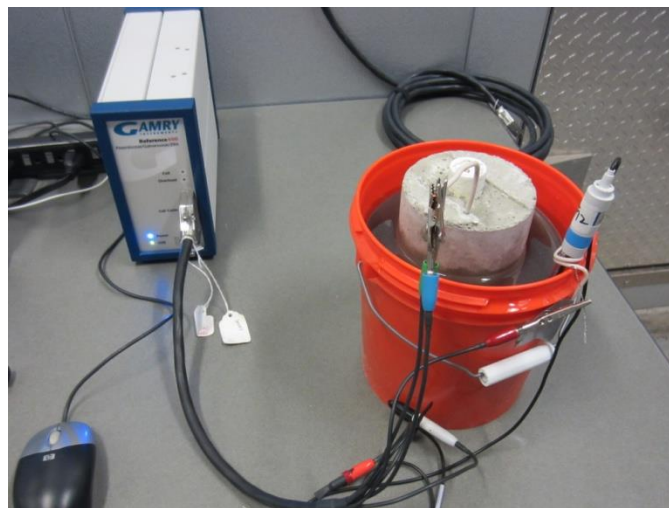


Source: FHWA.

Figure 201. Photo. Demolded concrete specimens.

Exposure Testing and Data Collection

This follow-up study employed three electrochemical testing methods: OCP for all specimens, rate of corrosion by LPR method for the cylindrical specimens, and $I_{macro-cell}$ for the slab specimens. At the beginning of the experiment, baseline data were collected. Figure 202 shows the OCP and LPR measurements in progress. The two-electrode system and a potentiostat were used for the LPR measurements. To avoid chloride contamination in the reference electrode (RE) being submerged in the salt solution, a glass body silver–silver chloride (Ag/AgCl) RE was used for the potential readings instead of conventional CSE. Figure 203 shows the OCP and $I_{macro-cell}$ measurement of the slab #2 specimen.



Source: FHWA.

Figure 202. Photo. OCP and LPR measurements of a cylindrical specimen.



Source: FHWA.

Figure 203. Photo. OCP and $I_{macro-cell}$ measurements of slab #2 specimen.

After the baseline data were collected, the cylindrical specimens were divided into three groups and placed in three plastic containers that were filled with 15 weight percent NaCl solution, as shown in figure 204. A temporary heat tent was fabricated with insulation boards for the specimens, as shown in figure 205. With three flood lamps and two digital thermostats, temperature inside the heat tent was maintained at 85–90 °F. Even though the temperature was set at 104 °F as the original study, it could not reach the target temperature due to poor insulation quality of the heat tent.



Source: FHWA.

Figure 204. Photo. Cylindrical specimens in a plastic container.



Source: FHWA.

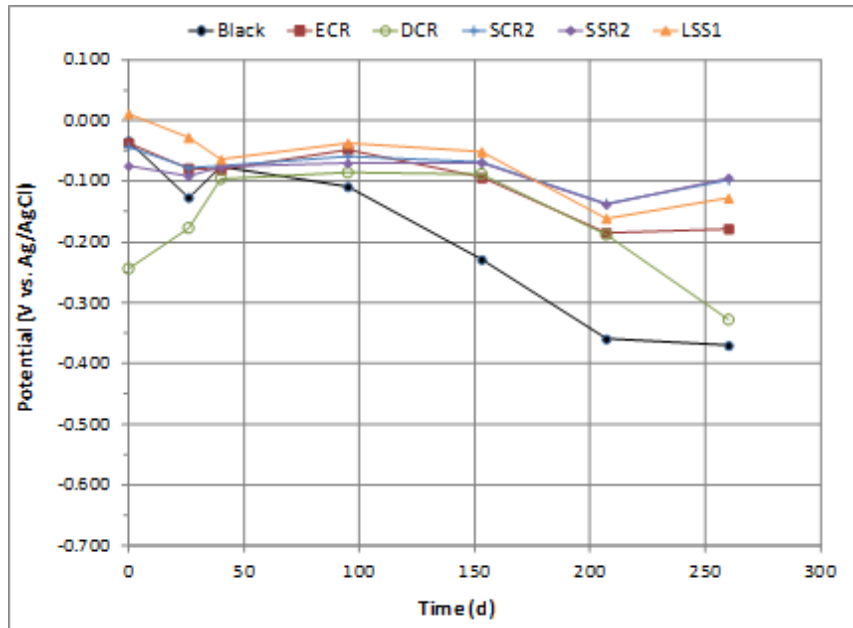
Figure 205. Photo. Arrangement of specimens in a temporary heat tent with lid removed.

TEST RESULTS AND DISCUSSION

A total of seven rounds of data collection occurred over the 260-d study period. The following subsections discuss the collected data.

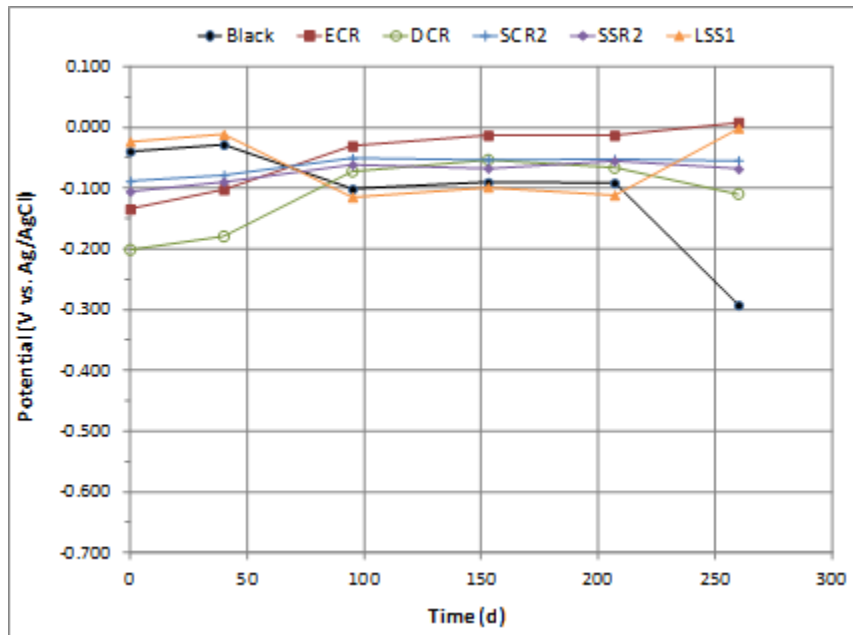
OCP Data

Figure 206 and figure 207 present the OCP versus time plot for the best and poorest performance bars embedded in the cylindrical specimens and the slab specimens, respectively. Since the Ag/AgCl RE gives about -0.100 V more positive readings than the CSE, the 90 percent probability of corrosion occurrence should be related to an RE more negative than -0.250 V versus Ag/AgCl (or roughly $-0.350\text{ V}_{\text{CSE}}$).⁽¹⁷⁾ According to this criterion, only black bar in the slab and black and DCR in the cylindrical specimens were judged to initiate corrosion.



Source: FHWA.

Figure 206. Graph. Mean OCP versus time plot for the best and poorest performance bars in the cylindrical specimens.

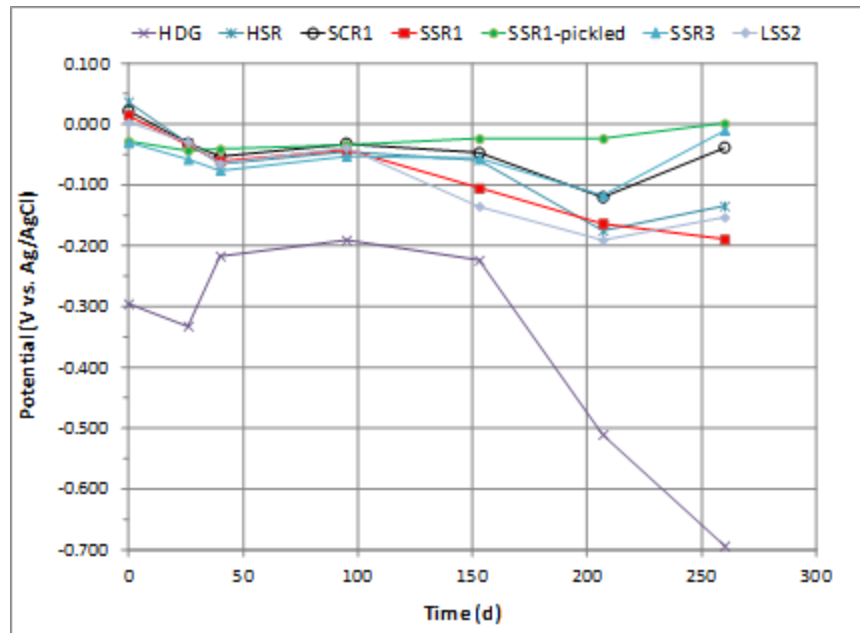


Source: FHWA.

Figure 207. Graph. OCP versus time plot for the best and poorest performance bars in the slab specimens.

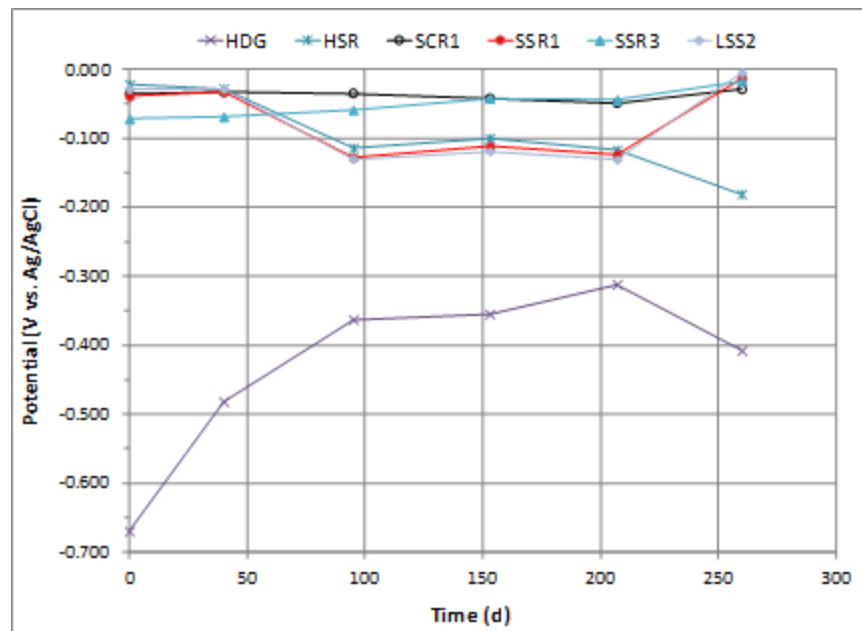
Figure 208 and figure 209 present the OCP versus time plot for the intermediate performance bars embedded in the cylindrical specimens and the slab specimens, respectively. As seen in the previous bar groups, the bars in this group, except for HDG, did not start corroding by the time

the experiment was terminated. As seen in the original study, the most negative OCP was exhibited by HDG due to active zinc coating. The bars in the slab tended to give more positive OCPs than those in the cylindrical specimens.



Source: FHWA.

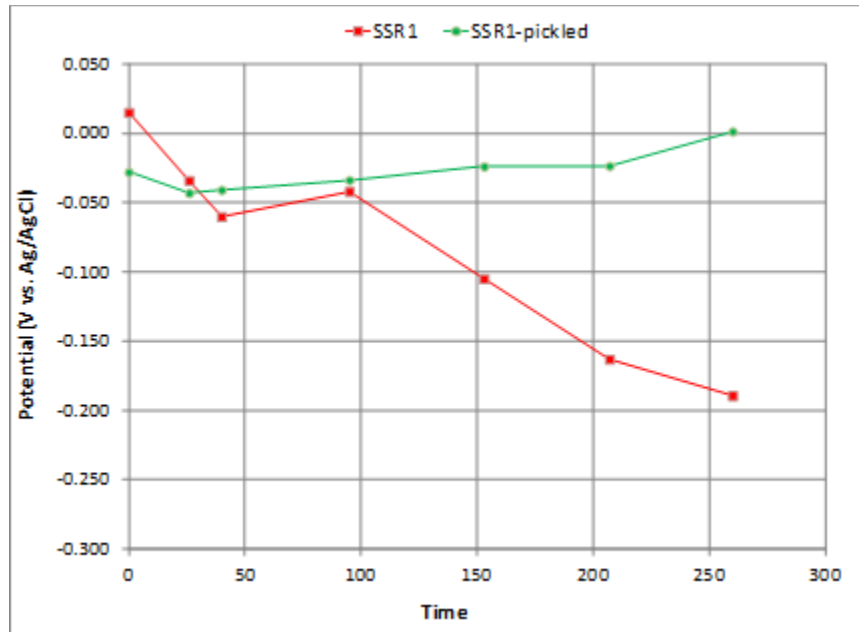
Figure 208. Graph. Mean OCP versus time plot for intermediate performance bars in the cylindrical specimens.



Source: FHWA.

Figure 209. Graph. OCP versus time plot for intermediate performance bars in the slab specimens.

A mean OCP versus time plot for as-received SSR1 and pickled SSR1 embedded in the cylindrical specimens is shown in figure 210. The potential data trend indicates that the pickled SSR1 showed more corrosion resistance by maintaining positive OCP, while the as-received SSR1 showed gradually decreasing OCP toward the active zone exhibiting more negative potential.

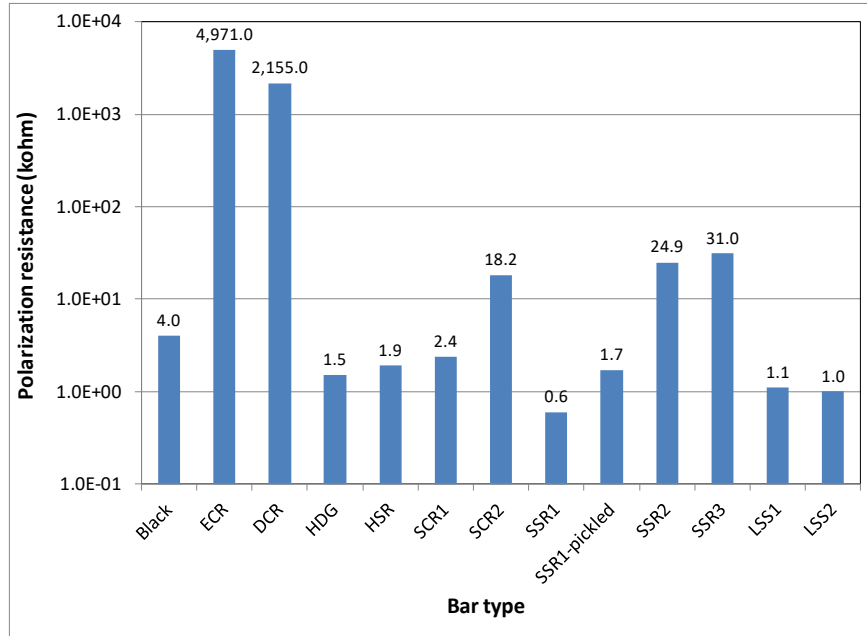


Source: FHWA.

Figure 210. Graph. Mean OCP versus time plot for as-received SSR1 and pickled SSR1 in the cylindrical specimens.

***R_p* Data**

Figure 211 presents the baseline R_p data of individual bar materials. As seen in the original study, ECR possessed the highest R_p . Although the R_p of DCR could not be determined in the concrete slab during the original study, DCR exhibited the second-highest R_p among the bars in the follow-up study. This may be attributed to an isolated, small DCR, making the R_p measurement possible. The other bars did not show any new results.



Source: FHWA.

Figure 211. Graph. Baseline R_p data.

***I_{macro-cell}* Data**

All of the bars embedded in the slabs exhibited negative $I_{macro-cell}$ throughout the duration of the study. The reversed $I_{macro-cell}$ flow was caused by the fact that the stainless steel meshes exhibited more negative OCP than the bar materials during the duration of the follow-up study. Their potentials could have been eventually more positive with time had strong passivity formed on the surface. As a result, the $I_{macro-cell}$ data were not informative to report.

CHAPTER 5. CONCLUSIONS

The following conclusions can be reached based on the research findings:

- The best corrosion performance group of reinforcing bars includes ECR, SCR2, DCR, and duplex SSR2. Differences among the bars within this group need to be determined further.
- The poor corrosion performance group includes black steel and LSS1.
- The intermediate corrosion performance group includes SSR1, SSR3, SCR1, LSS2, HSR, and HDG. More refined corrosion characteristics need to be investigated for this group of bar materials.
- A short-term follow-up study confirmed that the pickled SSR1 shows a more corrosion-resistant tendency by maintaining quite positive OCP compared to the as-received SSR1. This finding should emphasize the importance of a proper pickling process to maximize the inherent corrosion resistance of stainless steel bars.
- Since this current study was a short-term corrosion evaluation in a very specific environment, performance of all the rebar types tested may vary depending on the specific factors of installation and environment. In particular, ECR has shown considerable variability of performance in other tests and real-world applications due to its susceptibility to coating flaws/damage. Therefore, further durability tests or field evaluations of existing structures containing various types of metallic reinforcing steel materials are recommended to predict their long-term performance.

REFERENCES

1. Mehta, P.K. (1986). *Concrete—Structure, Properties, and Materials*, First Edition, Prentice-Hall, Inc., Upper Saddle River, NJ.
2. ASTM A615/A615M. (2014). “Standard Specification for Deformed and Plain Carbon-Steel Bars for Concrete Reinforcement,” *Book of Standards Volume 01.04*, ASTM International, West Conshohocken, PA.
3. ASTM A775/A775M. (2014). “Standard Specification for Epoxy-Coated Steel Reinforcing Bars,” *Book of Standards, 01.04 Volume* ASTM International, West Conshohocken, PA.
4. ASTM A1055/A1055M. (2010). “Standard Specification for Zinc and Epoxy Dual-Coated Steel Reinforcing Bars,” *Book of Standards Volume 01.04*, ASTM International, West Conshohocken, PA.
5. ASTM A767/A767M. (2009). “Standard Specification for Zinc-Coated (Galvanized) Steel Bars for Concrete Reinforcement,” *Book of Standards Volume 01.04*, ASTM International, West Conshohocken, PA.
6. AASHTO M 329M/M 329-11. (2011). *Standard Specification for Stainless Clad Deformed and Plain Round Steel Bars for Concrete Reinforcement*, American Association of State and Highway Transportation Officials, Washington, DC.
7. ASTM A240/A240M. (2015). “Standard Specification for Chromium and Chromium-Nickel Stainless Steel Plate, Sheet, and Strip for Pressure Vessels and for General Applications,” *Book of Standards Volume 01.03*, ASTM International, West Conshohocken, PA.
8. ASTM A955/A955M. (2014). “Standard Specification for Deformed and Plain Stainless-Steel Bars for Concrete Reinforcement,” *Book of Standards Volume 01.04*, ASTM International, West Conshohocken, PA.
9. ASTM A1035/A1035M. (2014). “Standard Specification for Deformed and Plain, Low-Carbon, Chromium, Steel Bars for Concrete Reinforcement,” *Book of Standards Volume 01.04*, ASTM International, West Conshohocken, PA.
10. ASTM A1010/A1010M. (2013). “Standard Specification for Higher-Strength Martensitic Stainless Steel Plate, Sheet, and Strip,” *Book of Standards Volume 01.03*, ASTM International, West Conshohocken, PA.
11. AASHTO MP 18M/MP 18-09. (2013). *Standard Specification for Uncoated, Corrosion-Resistant, Deformed and Plain Alloy, Billet-Steel Bars for Concrete Reinforcement and Dowels*, American Association of State and Highway Transportation Officials, Washington, DC.

12. NX Infrastructure, Ltd. (2008). *NX-SCR Specification Sheet*, West Glamorgan, United Kingdom. Available online: http://www.nxinfrastructure.com/sites/default/files/usa.spec_.pdf, last accessed October 11, 2016.
13. Hartt, W.H., Powers, R.G., Marino, F.P., Paredes, M., Simmons, R., Yu, H., Himiob, R., and Virmani, Y.P. (2009). *Corrosion Resistant Alloys for Reinforced Concrete*, Report No. FHWA-HRT-09-020, Federal Highway Administration, Washington, DC.
14. Carpenter Technology Corporation. (2010). *Technical Datasheet: EnduraMet® 32 Stainless*, Wyomissing, PA. Available online: <http://cartech.ides.com/datasheet.aspx?i=101&E=332>, last accessed October 11, 2016.
15. ArcelorMittal USA. (2010). *Duracorr®: Life-Cycle Cost-Effective 12% Chromium Stainless Steel*, ArcelorMittal USA, Burns Harbor, IN. Available online: <http://www.iowadot.gov/bridge/A1010/Presentations/ARCELORMITTAL%20DURACORR.pdf>, last accessed October 11, 2016.
16. Atlas Steel. (2015). *3CR12: The Superior Choice for Your Utility Stainless Steel Applications*, Atlas Steel, Twinsburg, OH. Available online: <http://www.atlassteel.com/products/3cr12.aspx>, last accessed October 11, 2016.
17. ASTM C876. (2009). "Standard Test Method for Corrosion Potentials of Uncoated Reinforcing Steel in Concrete," *Book of Standards Volume 03.02*, ASTM International, West Conshohocken, PA.
18. ASTM C1152/C1152M-04. (2012). "Standard Test Method for Acid-Soluble Chloride in Mortar and Concrete," *Book of Standards Volume 04.02*, ASTM International, West Conshohocken, PA.

